Response of a Multicomponent Interstellar Medium to External Gravitational Influences

V. A. Antonov and A. S. Baranov

Pulkovo Astronomical Observatory, Russian Academy of Sciences,
Pulkovskoe sh. 65, St. Petersburg, 196140 Russia
Received April 30, 2001; in final form October 19, 2001

Abstract—The contribution of cosmic rays as a collection of charged particles to the generation of currents in the interstellar medium and to the total viscosity of this medium is analyzed. Our estimates show that this contribution is negligible under the conditions commonly found in our Galaxy but can become important when an excess dust concentration above the mean level is combined with a local increase in the cosmic-ray density. © *2002 MAIK "Nauka/Interperiodica".*

1. INTRODUCTION

The response of the interstellar medium (ISM) to external gravitational influences, or, more precisely, the elasticity and rigidity of the medium, is not as straightforward a problem as is often believed [1, 2]. Studies usually fail to adequately allow for the multicomponent nature of the ISM. To perform a more detailed analysis, we consider here a model with an infinite uniform medium of fairly complex composition, neglecting self-gravity or including it in the external gravitational field. We use a four-component model for the interstellar medium. Appropriate subscripts—e, i, d, or c—are used to distinguish between parameters referring to these different components.

We restrict our analysis to the case of a constant gravitational perturbation in the form of a one-dimensional running wave with the field strength given in the (complex) form

$$F = \varepsilon e^{-i\omega t + i\kappa z}, \qquad (1)$$

where ε is a small parameter used for subsequent linearization, t is time, and ω and κ are the frequency and wavenumber of the perturbation. The wave propagates along the z axis; the two remaining coordinates do not enter into our computations.

We take the phase velocity $v_0 = \omega/\kappa$ to be in the interval $V \ll v_0 \ll c$, where V is the characteristic thermal velocity of particles of ordinary matter (not cosmic rays) and c is the speed of light. Accordingly, the hydrodynamical equations below neglect the pressure, whereas the cosmic-ray component, on the contrary, is relativistic and therefore essentially unresponsive to the gravitational field. The only role played by cosmic rays is as a static source of electromagnetic, or, more specifically, positive charge, due to the predominance of nuclei over electrons. A more detailed analysis of the joint response of various components to external influences brings to light certain features that are not evident in previous studies, which, as a rule, were restricted to the formal introduction of a single sound speed [3].

2. PRINCIPAL EQUATIONS

Our adopted assumptions imply that electrons, ions, and cosmic dust should individually satisfy the one-dimensional hydrodynamical equation for a cold medium and the continuity equation

$$\frac{\partial w}{\partial t} + w\frac{\partial w}{\partial z} = F + \frac{e}{m}E + \frac{A}{mn}, \qquad (2)$$

$$\frac{\partial n}{\partial t} + \frac{\partial}{\partial z}(nw) = 0.$$

In (2), w is the z velocity of the component considered, e and m the charge and mass of the particle type considered, n the particle volume density, E the intensity of the electric field along the z axis, and A the specific force per unit volume due to friction. To simplify our analysis, we take e and m to represent mean parameters, although their values can differ for different ions or dust particles. Linearization of (2) yields

$$\frac{\partial w}{\partial t} = F + \frac{e}{m}E + \frac{A}{mn}, \qquad (3)$$

$$\frac{\partial \delta n}{\partial t} + n\frac{\partial w}{\partial z} = 0,$$

where we have introduced the perturbation δn of the particle-number density to denote its departure from the initial density n. We must also take into account

the Poisson equation for the electric field, which in the one-dimensional case reduces to

$$\frac{\partial E}{\partial z} = 4\pi\rho, \tag{4}$$

where ρ is the total space density of emerging charges; i.e.,

$$A = \sum_\alpha e_\alpha \, \delta n_\alpha. \tag{5}$$

In (5) and the following equations, α can represent any of the subscripts e, i, d, or c mentioned above. We then isolate the arguments t and z in the usual way and go over, as in (1), to the complex form $\partial/\partial t = -i\omega$, $\partial/\partial z = i\kappa$. In view of (4), Eqs. (3) acquire the form

$$-i\omega w_\alpha = \varepsilon - \frac{4\pi i e_\alpha}{m_\alpha \kappa}\rho + \frac{A_\alpha}{m_\alpha n_\alpha}, \tag{6}$$

$$\delta n_\alpha = \frac{\kappa n_\alpha}{\omega} w_\alpha.$$

We now specify the frictional force, which is also electromagnetic but is manifest irregularly via collisions. Friction in plasma has been the subject of numerous studies [4, 5]. Its analog in stellar dynamics is so-called dynamical friction [6–8].

Friction is the result of the relative motions of particles, and must therefore be included at this stage. We assume that the systematic velocities w_α (or rather, their differences) are small even compared to the thermal velocities, so the frictional forces can also be linearized, yielding formulas of the form

$$A_\alpha = \sum_\beta q_{\alpha\beta}(w_\beta - w_\alpha), \quad q_{\alpha\beta} \geq 0, \tag{7}$$

where, by virtue of the equality of action and reaction, the coefficients $q_{\alpha\beta}$ should obey the symmetry rule $q_{\alpha\beta} = q_{\beta\alpha}$. The parameter $\beta = \alpha$ can be excluded from the summation, since a given component does not act on itself.

Simple manipulations with (5)–(7) enable us to derive the following algebraic relations for the induced velocities:

$$\omega w_\alpha - \frac{4\pi e_\alpha}{\omega w_\alpha}\sum_\alpha e_\alpha n_\alpha w_\alpha \tag{8}$$

$$-\frac{i}{m_\alpha n_\alpha}\sum_\beta q_{\alpha\beta}(w_\beta - w_\alpha) = i\varepsilon.$$

Recall that we assumed that $w_\alpha = 0$ for cosmic rays. We neglect the scattering of cosmic rays on ions and electrons, and vice versa, due to the smallness of these effects.

3. COSMIC PLASMA WITHOUT DUST

In the absence of dust, the system of equations (8) reduces to two equations:

$$\omega w_e - \frac{4\pi e_e}{\omega m_e}(e_e n_e w_e + e_i n_i w_i) \tag{9}$$

$$-\frac{i}{m_e n_e}q_{ei}(w_i - w_e) = i\varepsilon,$$

$$\omega w_i - \frac{4\pi e_i}{\omega m_i}(e_e n_e w_e + e_i n_i w_i)$$

$$-\frac{i}{m_i n_i}q_{ei}(w_e - w_i) = i\varepsilon.$$

It is convenient to introduce the macroscopic parameters $X = m_e n_e w_e + m_i n_i w_i$, $Z = e_e n_e w_e + e_i n_i w_i$, which are related to the mass-flow rate and electric field in obvious ways. The velocities of the components can be expressed in terms of these quantities as follows:

$$w_e = \frac{e_i X - m_i Z}{n_e(m_e e_i - m_i e_e)}, \tag{10}$$

$$w_i = \frac{m_e Z - e_e X}{n_i(m_e e_i - m_i e_e)}.$$

We now multiply the first and second equations of (9) by $m_e n_e$ and $m_i n_i$ or by $e_e n_e$ and $e_i n_i$, respectively. After summation, we obtain in either case

$$\omega X + \frac{4\pi}{\omega}n_c e_c Z = i\varepsilon(m_e n_e + m_i n_i), \tag{11}$$

$$\omega Z - \frac{4\pi}{\omega}\left(\frac{e_e^2 n_e}{m_e} + \frac{e_i^2 n_i}{m_i}\right)Z$$

$$+\frac{iq_{ei}}{m_e m_e n_i n_e}[(m_e n_e + m_i n_i)Z + e_c n_c X] = -i\varepsilon e_c n_c.$$

When deriving (11), we took into account the initial electrical-neutrality condition

$$e_e n_e + e_i n_i = -e_c n_c. \tag{12}$$

This transformation gives rise to the small parameter $n_c/n_e \approx n_c/n_i$. Solution of system (11) yields

$$Z = \varepsilon e_c n_c\left[\frac{q_{ei}(m_e n_e + m_i n_i)}{\omega m_e m_i n_e n_i} - i\right] \tag{13}$$

$$\times\left\{\omega - \frac{4\pi}{\omega}\left(\frac{e_e^2 n_e}{m_e} + \frac{e_i^2 n_i}{m_i}\right)\right.$$

$$\left.+\frac{iq_{ei}}{m_e m_i n_e n_i}\left[m_e n_e + m_i n_i - \frac{4\pi(e_c n_c)^2}{\omega^2}\right]\right\}^{-1}.$$

The parameter X can then be derived from the first equation of (11).

A more specific analysis requires some numerical estimates. As noted above, we neglect the presence of heavy elements in cosmic rays and among ions, and

can therefore use the parameters for protons: $m_i = 1.67 \times 10^{-24}$, $e_i = e_c = -e_e = 4.8 \times 10^{-10}$ (here and below, we use CGS units). We adopt the volume densities $n_e \approx n_i \approx 0.08$ and $n_c \approx 0.8 \times 10^{-10}$ [9].

When finding q_{ei}, we take into account the fact that, after each free flight, an individual electron imparts an average momentum of $m_e(w_e - w_i)$ to the ion component, and the additional coefficient n_e must be introduced to allow for the total number of electrons per unit volume. This transfer of momentum occurs during the free-flight time [4]

$$\tau \approx \frac{m_e^2 V^3}{16\pi e_e^4 n_e L},\qquad(14)$$

where $L \approx 15$ is the well-known Coulomb logarithm and the velocity V refers to the electrons. Furthermore, $m_e = 9.1 \times 10^{-28}$.

It is known [9, 10] that the electron temperature in the interstellar gas can vary substantially, and we adopt an average value of $V \approx 5.5 \times 10^6$. Comparing (14) and the accompanying arguments to the definition of q_{ei} in (7), we now find that

$$q_{ei} = \frac{16\pi e_e^4 n_e^2 L}{m_e V^3}.\qquad(15)$$

Computation yields $q_{ei} \approx 1.7 \times 10^{-30}$.

It is convenient to introduce the total density of the medium $\sigma = m_i n_i + m_e n_e \approx m_i n_i$ and a number of characteristic frequencies. We first use as an example the frequency of the external perturbation $\omega = 0.2 \times 10^{-14}$, which corresponds to the period of the two-armed wave in the Galaxy. We then determine the plasma frequency [4]

$$\Omega = \sqrt{4\pi\left(\frac{e_e^2 n_e}{m_e} + \frac{e_i^2 n_i}{m_i}\right)} \approx \sqrt{4\pi\frac{e_e^2 n_e}{m_e}},$$

the dissipative decrement

$$\omega' = \frac{q_{ei}(m_e n_e + m_i n_i)}{m_e m_i n_e n_i} \approx \frac{q_{ei}}{m_e n_e},$$

and the combined frequency

$$\tilde{\omega} = \sqrt{4\pi\frac{e_c^2 n_c^2}{m_e n_e + m_i n_i}} \approx e_c n_c \sqrt{\frac{4\pi}{m_i n_i}}.$$

Equation (13) can then be rewritten in the form

$$Z = \varepsilon e_c n_c\left(\frac{\omega'}{\omega} - i\right)\qquad(16)$$

$$\times \left[\omega - \frac{\Omega^2}{\omega} + i\omega'\left(1 - \frac{\tilde{\omega}^2}{\omega^2}\right)\right]^{-1}.$$

Substituting the parameter values yields approximately $\omega' = 0.023$, $\Omega = 1.6 \times 10^4$, and $\tilde{\omega} = 3.7 \times$

10^{-7}. It is clear that we have with a large margin $\Omega \gg \omega' \gg \omega$, $\tilde{\omega} \gg \omega$, and $\Omega \gg \omega'\tilde{\omega}^2/\omega$, so both the numerator and denominator in (16) reduce to single terms:

$$Z = -\frac{\varepsilon e_c n_c \omega'}{\Omega^2}.\qquad(17)$$

Here, an important point is the computation of the work done by the gravitational field on the moving plasma. The work per period per unit volume will be

$$W = \frac{2\pi}{\omega}\mathrm{Re}\,\varepsilon X$$

or, in view of the first equation in (11) and formula (17),

$$W = \frac{8\pi^2(e_c n_c)^2\omega'}{\omega^3\Omega^2}\varepsilon^2.$$

We are interested in the ratio of this work per period to the density of gravitational energy:

$$\mu = W\left(\frac{\varepsilon^2}{8\pi G}\right)^{-1} = \frac{64\pi^3 G(e_c n_c)^2\omega'}{\omega^3\Omega^2} \sim 2 \times 10^{-9}$$

(G is the gravitational constant). Therefore, the electrostatic effect of cosmic rays in the Galaxy is negligible.

4. A MEDIUM WITH DUST

In the presence of dust, Eqs. (8) acquire the form

$$\omega w_e - \frac{4\pi e_e}{\omega m_e}(e_e n_e w_e + e_i n_i w_i)\qquad(18)$$

$$-\frac{i}{m_e n_e}q_{ei}(w_i - w_e) - \frac{i}{m_e n_e}q_{ed}(w_d - w_e) = i\varepsilon,$$

$$\omega w_i - \frac{4\pi e_i}{\omega m_i}(e_e n_e w_e + e_i n_i w_i)$$

$$-\frac{i}{m_i n_i}q_{ei}(w_e - w_i) - \frac{i}{m_i n_i}q_{id}(w_d - w_i) = i\varepsilon,$$

$$\omega w_d - \frac{i}{m_d n_d}q_{de}(w_e - w_d) - \frac{i}{m_d n_d}q_{di}(w_i - w_d) = i\varepsilon.$$

Similarly, we expand the definition

$$X = m_e n_e w_e + m_i n_i w_i + m_d n_d w_d\qquad(19)$$

and, leaving Z unchanged, multiply Eqs. (18) by $m_e n_e$, $m_i n_i$, and $m_d n_d$ and sum them to obtain

$$\omega X + \frac{4\pi}{\omega}n_c e_c Z = i\varepsilon(m_e n_e + m_i n_i + m_d n_d).\qquad(20)$$

Multiplying the first two equations in (18) by $e_e n_e$ and $e_i n_i$ and adding the resulting equations yields

$$\frac{1}{\omega}\left[\omega^2 - 4\pi\left(\frac{e_e^2 n_e}{m_e} + \frac{e_i^2 n_i}{m_i}\right)\right]Z\qquad(21)$$

$$-i\left(\frac{e_e}{m_e}-\frac{e_i}{m_i}\right)q_{ei}(w_i-w_e)-\frac{ie_e}{m_e}q_{ed}(w_d-w_e)$$

$$-\frac{ie_i}{m_i}q_{id}(w_d-w_i)=-i\varepsilon n_c e_c.$$

We denoted the second bracketed term in (21) as Ω^2 and verified that Ω is much higher than the other characteristic frequencies. To a first approximation, we can leave only this term in (21). In this case, $Z\approx 0$, and substitution into (20) yields a purely imaginary value:

$$X\approx X_0=\frac{i\varepsilon}{\omega}(m_e n_e+m_i n_i+m_d n_d).$$

Here, we are interested in the correction X_1 with the next order of smallness. To derive this correction, we estimate the remaining terms in (21) by writing w_e, w_i, and w_d in terms of X and Z and using the third equation in (18). In fact, no correction is needed for the coefficient of Ω^2 at Z, and we can immediately set $Z=0$; i.e., we can consider w_e and w_i as a solution to the system of equations $n_e e_e w_e+n_i e_i w_i=0$ with (19) and the third equation of (18). We then substitute this solution into (21) to obtain

$$-\frac{\Omega^2}{\omega}Z=\frac{X_0}{\Delta m_i m_e}\left\{i\omega[e_e e_i(q_{ed}n_i m_i\right.\qquad(22)$$

$$-q_{id}n_e m_e)+n_c e_c q_{ei}(e_i m_e-e_e m_i)]$$

$$-\frac{e_c n_c}{m_d n_d}(e_i m_e-e_e m_i)(q_{di}q_{de}+q_{ei}q_{de}+q_{ei}q_{di})\bigg\}$$

$$+\frac{\varepsilon}{\Delta}\left[n_i n_e(e_i m_e-e_e m_i)\left(\frac{e_e}{m_e}q_{ed}+\frac{e_i}{m_i}q_{id}\right)\right.$$

$$-m_d n_d n_c e_c q_{ei}\left(\frac{e_e}{m_e}-\frac{e_i}{m_i}\right)$$

$$+m_d n_d e_e e_i\left(\frac{q_{ed}n_i}{m_e}-\frac{q_{id}n_e}{m_i}\right)\bigg]-i\varepsilon n_c e_c,$$

where

$$\Delta=i(n_e e_e q_{di}-n_i e_i q_{de})$$

$$-n_i n_e(e_i m_e-e_e m_i)\left[\omega+\frac{i(q_{de}+q_{di})}{m_d n_d}\right].$$

We now return to numerical estimates. In collisions with neutral particles, the free-flight time is determined by a well-known formula that differs from, namely:

$$\tau=\frac{1}{\pi n_d r^2 V},$$

where r is the radius of the dust particles. Accordingly,

$$q_{de}=\pi n_d n_e m_e r^2 V_e,\quad q_{di}=\pi n_d n_i m_i r^2 V_i.\qquad(23)$$

As is usual [9], we adopt $r\approx 10^{-5}$. A straightforward estimate of the de Broglie wavelength shows that the wave properties of electrons and ions are not important in this case. We also apply the thermal-equilibrium condition $m_i V_i^2\approx m_e V_e^2$. We already adopted $V_e\approx 5.5\times 10^6$ above. We now further assume [9] that $m_d n_d\approx 10\times 10^{-26}$, and, for spherical particles with a density of approximately unity, formulas (23) yield $q_{de}=3\times 10^{-43}$, $q_{di}=1.3\times 10^{-41}$.

In the formula for Δ, the parameter ω dominates over the neighboring terms. Dropping only terms that are small compared to neighboring terms in the right-hand side of (22), we can rewrite this equality in the simplified form

$$Z=\left\{\frac{X_0}{m_i m_e}n_c e_c q_{ei}\left(i\omega-\frac{q_{de}+q_{di}}{m_d n_d}\right)\right.\qquad(24)$$

$$+\varepsilon\left[n_i n_e\left(\frac{e_e}{m_e}q_{ed}+\frac{e_i}{m_i}q_{id}\right)+\frac{m_d n_d n_c e_c q_{ei}}{m_e m_i}\right]\bigg\}\frac{1}{n_e n_i}.$$

In view of (20), we have for the correction X_1

$$\mathrm{Re}X=\mathrm{Re}X_1=-\frac{4\pi}{\omega^2}n_c e_c\mathrm{Re}Z,$$

implying that in a medium with dust the ratio of the work done by the gravitational field to the proper energy of this field is

$$\mu=\frac{16\pi^2 G}{\omega\varepsilon}\mathrm{Re}X=\frac{64\pi^3 G}{\omega^3\varepsilon}n_c e_c\mathrm{Re}Z,$$

where Z is determined by (24). If $q_{ed}=q_{id}=0$, i.e., in the absence of dust, we return to the previous formula for μ. In our numerical estimates, the contributions to μ due to terms with q_{ed} and q_{id} have essentially the same order of magnitude. Therefore, the electrostatic effect remains negligible under the conditions found in the Galaxy, even in the presence of dust.

5. CONCLUSIONS

As is well known, the parameter n_d can vary over a wide range and can exceed the value adopted here by five to six orders of magnitude in very dense globules. The density n_c of cosmic rays should also increase in the vicinity of their sources. Therefore, in principle, we must allow for the possibility of a significant increase in the cosmic-ray viscosity of the medium inside very dense gas and dust clouds, especially if the cosmic-ray density is also high. This is also true for other galaxies, for which the quantitative composition of the cosmic rays remains almost completely unknown.

REFERENCES

1. S. A. Kaplan and S. B. Pikel'ner, *The Interstellar Medium* (Fizmatgiz, Moscow, 1963; Harvard Univ. Press, Cambridge, 1970).
2. V. G. Gorbatskiĭ, *Gas-Dynamical Instabilities in Astrophysical Systems* (Sankt-Peterb. Gos. Univ., St. Petersburg, 1999).
3. V. L. Polyachenko and A. M. Fridman, *Physics of Gravitating Systems* (Nauka, Moscow, 1976; Springer-Verlag, New York, 1984).
4. E. M. Lifshitz and L. P. Pitaevskiĭ, *Physical Kinetics* (Nauka, Moscow, 1979; Pergamon, Oxford, 1981).
5. J. P. Shkarofsky, T. W. Johnston, and M. P. Bachynski, *The Particle Kinetics of Plasmas* (Addison-Wesley, Reading, 1966; Atomizdat, Moscow, 1969).
6. S. Chandrasekhar, Astrophys. J. **97**, 255 (1943); **98**, 54 (1943).
7. A. S. Baranov and Yu. V. Batrakov, Astron. Zh. **51**, 310 (1974) [Sov. Astron. **18**, 180 (1974)].
8. V. A. Antonov and A. S. Baranov, Byull. Inst. Teor. Astron. **13**, 52 (1974).
9. D. Ya. Martynov, *A Course in General Astrophysics* (Nauka, Moscow, 1979).
10. L. Aller, *Astrophysics* (Ronald, New York, 1954; Inostrannaya Literatura, Moscow, 1957), Vol. 2.

Translated by A. Dambis

Logarithmic Density Range and the Percentage of Stars in the Cores of Various Subsystems of the Globular Clusters M56, M12, NGC 6535, NGC 6171, NGC 5466, and M92

Z. I. Peikov

University for Foreign Students, Sofia, Bulgaria
Received April 14, 2000

Abstract—Lower limits for the percentages of stars with various luminosities in the cores of six globular clusters are derived using stellar spatial density distributions $f(r)$ to deep limiting B magnitudes obtained earlier. For NGC 6535 and NGC 5466, the logarithmic density range and Kholopov parameters D_f and D_r are also determined. These two parameters are correlated with the mean masses of stars of various subsystems and the total mass (number) of stars in the cluster. © *2002 MAIK "Nauka/Interperiodica"*.

1. INTRODUCTION

In our previous studies [1−6], we derived the stellar density distributions $f(r)$ for various subsystems of the clusters M56, M12, NGC 6535, NGC 6171, NGC 5466, and M92 (where r is the clustercentric distance). These subsystems include stars to deep limiting B magnitudes, corresponding to regions near and below the main-sequence (MS) turnoff in the $(V, B−V)$ diagrams of the clusters. We analyzed these distributions to study the deep spatial structure of these objects and showed that this structure changes systematically with increasing limiting B magnitude below the transition region between the subgiant branch and the MS turnoff in the $(V, B−V)$ diagram.

In this connection, it is of interest to determine the percentages of stars of various luminosities in the cores of these clusters, as well as the logarithmic density ranges and Kholopov parameters D_r and D_f [7], which are correlated with the total cluster mass and the mean mass of stars in the given subsystem, respectively.

2. THEORETICAL FORMULATION OF THE PROBLEM

The distributions of various types of stars in the cores and coronas of globular clusters play an important role in the structure and dynamics of these objects. Open clusters have been studied in the most detail from this point of view. Long ago, Kholopov [7, 8] showed that the brightest and most massive stars are observed predominantly in cluster cores. The coronas contain a large fraction of the faint stars (up to 90% in rich clusters), making their total masses comparable to or even greater than the masses of the cores. Furthermore, there is a well-defined relation between the total number of cluster stars brighter than $M_V = +5^m$, N_5, and the percentage of MS stars in the core. The richer the cluster, the lower the percentage of its faint stars located in the core.

The percentage of weak MS stars in the cores of globular clusters is poorly known because of the high concentration of stars in the cluster center. According to the theory of stellar evolution in clusters, the percentage of red giants in cluster cores should be equal to the corresponding percentage for the stars on the upper MS from which the red giants evolved, i.e., 10−20%. However, observations show that the cores of rich globular clusters contain about 70% of the red-giant and horizontal-branch stars. Apparently, these percentages differ somewhat in such clusters. Differences between the distributions of stars with various luminosities in old clusters could be due to dynamical and evolutionary effects associated with mass loss from stars at the red-giant stage and their spatial redistribution [9−10]. Thus far, there is no precise explanation for this effect.

Kholopov [11] showed that star clusters display a number of relations. The cluster radius R_c is proportional to the cluster mass m_c and is correlated with the core radius r_n. Furthermore, there is also a relation between R_0/r_0 and m_c, where r_0 is the radius of the central core region, as is confirmed by a comparison of the stellar space-density distributions $f(r)$ in open and globular clusters, i.e., by an analysis of the so-called logarithmic density range. Figure 1 (adopted from [7]) shows $\log(f(r)/f_0)−\log(r/R_0)$ relations for several clusters. Here, r is the clustercentric distance and f_0 is the spatial density of
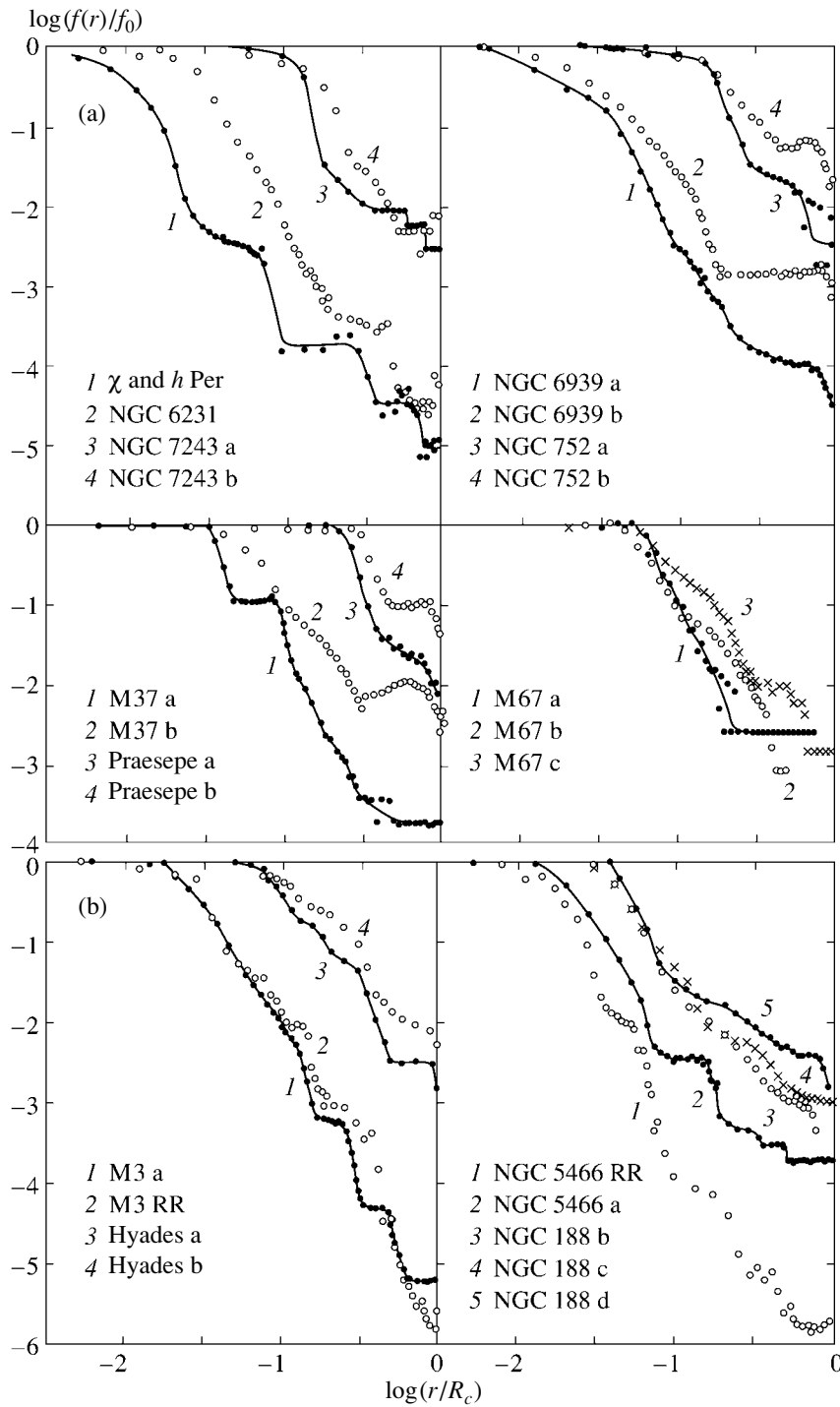
Fig. 1. $\log(f(r)/f_0)$ as a function of $\log(r/R_c)$ for the clusters (a) h and χ Per, NGC 6231, NGC 7243, NGC 752, NGC 6939, M37, M67, and Praesepe and (b) the Hyades, M3, NGC 188, and NGC 5466. See [7] for a detailed description of the notation we have adopted for this figure.

stars at the cluster center. The overall similarity of the curves is evident, supporting the idea that the structures of all stellar clusters have a common nature.

If appropriately calibrated, the plots in Fig. 1 can be used to determine the total mass of the cluster and the mean masses of stars in various subsystems. Kholopov [7] introduced the two parameters D_r and D_f.

$D_r - |\log(r_0/R_c)|$ is the distance from the coordinate origin to the intersection of the extension of
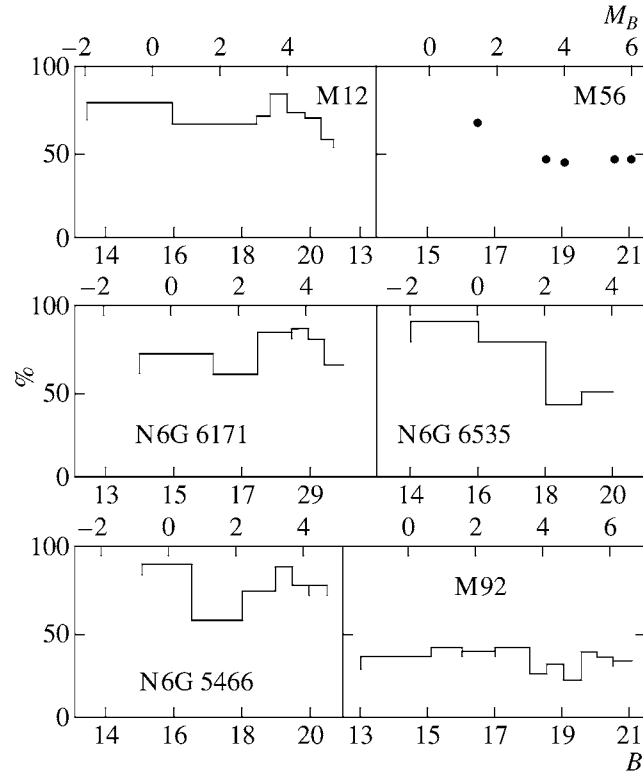
Fig. 2. Lower limit of the percentage of stars with various luminosities in the cores of the clusters studied.

the log $(f(r)/f_0)$ curve and the x axis (Fig. 1). The parameter D_r is correlated with the total mass of the cluster m_c. Unfortunately, we cannot apply the appropriate calibration here, since the total masses (and, consequently, the total numbers of stars) in the clusters are unknown.

$D_f - |\log(f(R_c)/f_0)|$ is the distance from the coordinate origin to the intersection of the extension of the log $(f(r)/f_0)$ curve and the y axis. In practice, it is the difference between the logarithms of the densities in the central core region and the corona of the cluster. The parameter D_f is a good indicator of the concentration of stars toward the cluster center. It is correlated with the mean masses of stars of the corresponding cluster subsystems containing MS stars obeying the mass–luminosity relation. Kholopov gives the following calibration for D_f based on open-cluster data:

$$\log \bar{m}_c = -0.70 + 0.37 D_f$$

for $\bar{m} \in (0.5, 3) m_\odot$, where $m_\odot$ is the solar mass. Here, we assume that D_f is independent of the total mass of the cluster and depends only on its age: for very young open clusters, D_f is systematically smaller than its mean value, whereas the situation is the opposite for very old clusters. This has to do with the dynamical evolution of the cluster. Since there are

still very few determinations of D_f for MS stars in globular clusters, we do not present a calibration for this relation.

In our previous works [1–6], we showed that the spatial structure of the clusters we are studying varies systematically as the limiting B magnitude for the corresponding stellar subsystems increases, starting from some $\bar{B}_{\rm lim}$ that corresponds to the transition region between the subgiant branch and the MS turnoff in the $(V, B-V)$ diagram. This variation is manifest as a homologous increase of the radii of spatial zones of the cluster (introduced by Kholopov [7]) and of the cluster radius in accordance with a single law, as well as a decrease in the degree of concentration of stars toward the center. When $B < B_{\rm tot}$, no systematic structural variations are evident, due to observational selection effects: high-mass stars that were located on the zero-age main sequence far above the current turnoff have long ago evolved into white dwarfs and neutron stars and are no longer observable in the cluster.

In view of the above, we expect that systematic variations of the cluster structure should also appear in variations of D_f and the percentages of stars with various luminosities in the cluster core: these parameters should remain approximately constant when $B < \bar{B}_{\rm lim}$, whereas they should decrease in

Table 1. Percentage of stars with various luminosities in the cores of clusters studied

M12								
ΔB	ΔN_1	ΔN_2	ΔN_3	ΔN_4	ΔN_5	ΔN_6	ΔN_{tot}	$(\Delta N_2 + \Delta N_3)/\Delta N_{tot}$
			$(r > 2')$				$(r > 2')$	$(r > 2')$, %
$12.5-15.0^m$	−	27	34	12	3	−	76	80
$15.0-17.5$	−	18	236	65	59	−	378	67
$17.5-17.9$	−	23	73	30	9	−	135	71
$19.9-18.4$	−	193	190	58	16	−	457	84
$18.4-18.9$	−	355	648	279	101	−	1383	73
$18.9-19.4$	−	918	1775	738	291	165	3887	69
$19.4-19.75$	−	1067*	1236	836	491	396	4026	57

M56								
B	N_1	N_2	N_3	N_4	N_5	N_6	$N_{tot}(B)$	$(N_2 + N_3)/N_{tot}$
							$(r > 0.4')$	$(r > 0.4')$, %
$m_{pg} = 16.7$	14	113	109	43	76		327	68
$B = 19.0^m$	49	231	367	245	463		1306	46
19.5	−	378	534	586	587		2085	44
21.0	−	1257*	2079	1625	1051	1180	7192	46
21.5	−	1465*	2278	1983	1013	1352	8091	46

NGC 6171								
ΔB	ΔN_1	ΔN_2	ΔN_3	ΔN_4	ΔN_5	ΔN_6	$\Delta N_{tot}(B)$	$(\Delta N_2 + \Delta N_3)/(\Delta N_2 + \Delta N_3$
							$(r > 1')$	$+\Delta N_4 + \Delta N_5 + \Delta N_6)$, %
$14.0-16.2^m$	69	86	56	24	21	10	111	72
$16.2-17.5$	42	67	76	57	33		166	61
$17.5-18.5$	47*	134	121	21	24		166	85
$18.5-19.0$	−	258*	58	52	0	0	223	86
$19.0-19.5$	−	356*	284	107	56		635	80
$19.5-20.0$	−	473*	854	452	170	92	1863	65
$20.0-20.6$	−	−	3303*	1846	980	727	−	−

Table 1. (Contd.)

NGC 6535

ΔB	ΔN_1	ΔN_2	ΔN_3	ΔN_4	ΔN_5	ΔN_{tot} ($r > 0.6'$)	$(\Delta N_1 + \Delta N_2 + \Delta N_3)/\Delta N_{\text{tot}}$ ($r > 0.6'$), %
$14.0-16.0^m$	7	18	14	3	1	14	91
$16.0-18.0$	3	14	26	8	4	34	78
$16.0-19.0$	6	22	30	20	13	57	64
$19.0-20.0$	8	18	23	33	18	74	49
$20.0-21.0$	—	79*	158	192	88	438	>46
$21.0-21.5$	—	—	147*	286	194	627*	—

NGC 5466

ΔB	ΔN_1	ΔN_2	ΔN_3	ΔN_4	ΔN_5	ΔN_6	ΔN_7	ΔN_{tot}	$(\Delta N_1 + \Delta N_2 + \Delta N_3)/\Delta N_{\text{tot}}$, %
$15.0-16.5^m$	11	42	31	6	3	—	—	93	90
$16.5-18.0$	9	42	40	32	24	11		158	58
$18.0-19.0$	43	102	70	44	11	15		285	75
$19.0-19.5$	41	184	78	23	14	—	—	340	89
$19.5-20.0$	51	363	229	111	47	24	—	825	78
$20.0-20.5$	125	626	526	183	110	29	46	1645	78
$20.5-21.0$	—	1588*	795	606	238	101	80	>3408	>70

M92

ΔB	ΔN_1	ΔN_2	ΔN_3	ΔN_4	ΔN_5	ΔN_{tot} ($r > 2'$)	$\Delta N_3/\Delta N_{\text{tot}}$ ($r > 2'$), %
$13.0-15.1^m$	—	—	44	17	12	123	36
$15.1-16.0$	—	—	60	30	8	143	42
$16.0-17.0$	—	—	81	30	9	202	40
$17.0-18.0$	—	—	245	27	24	579	42
$18.0-18.5$	—	—	212	88	26	796	27
$18.5-19.0$	—	—	416	202	52	1301	32
$19.0-19.5$	—	—	398	258	115	1755	23
$19.5-20.0$	—	—	937	225	56	2401*	39
$20.0-20.5$	—	—	1329	394	198	3719*	36
$20.5-21.0$	—	—	1604	681	379	4519*	35

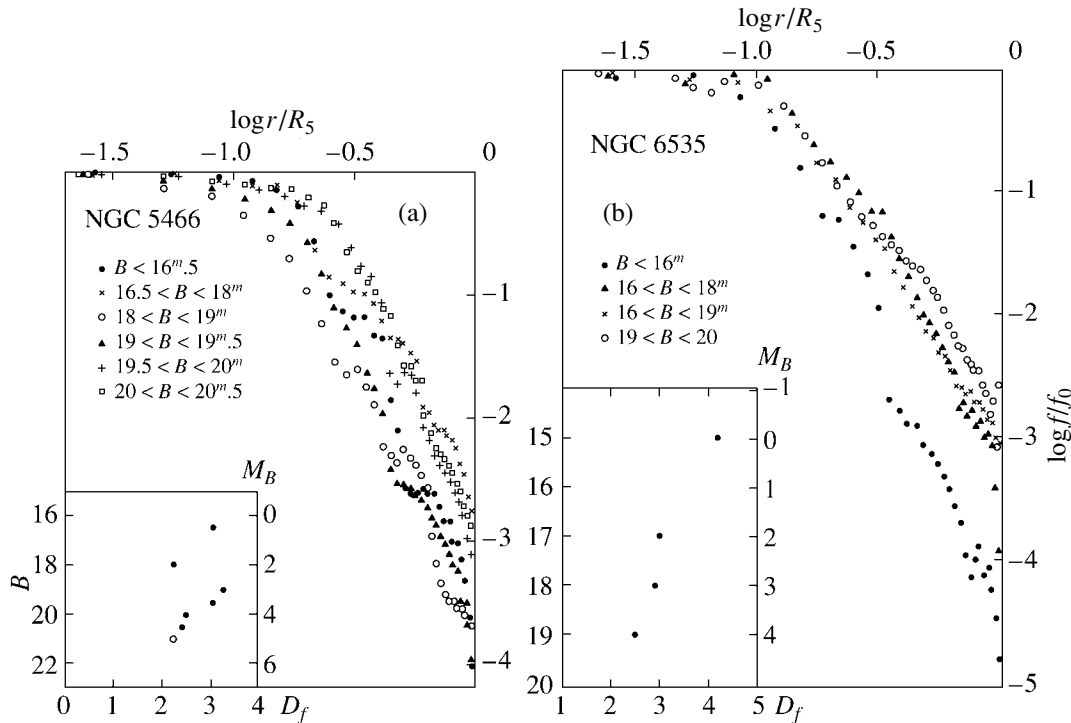Note: Asterisks indicate cases of extrapolation.

Fig. 3. Logarithmic density range and D_f for various subsystems of (a) NGC 5466 and (b) NGC 6535.

accordance with the mass–luminosity relation for MS stars and with the changes in the degree of concentration of stars toward the cluster center when $B < \bar{B}_{\lim}$. The second parameter $D_r = |\log(r_0/R_c)|$ should remain approximately constant for all B values, since these clusters have a homologous structure and the relative zone radii $\tilde{r}_i = R_i(B)/R_c(B)$ are the same for all B. According to [7], D_r is indeed correlated with the total mass of the cluster, which is independent of B.

3. PERCENTAGES OF STARS WITH VARIOUS LUMINOSITIES IN THE CLUSTER CORES

We used the numerical values of the differential curves of the spatial stellar-density distributions $\Delta f(r, \Delta B)$ for various magnitude intervals ΔB in the clusters studied [1–6] to determine the numbers of stars $\Delta N_i(\Delta B)$ in various spatial zones and the total number of stars $\Delta N_{\text{tot}}(\Delta B)$ in a given interval ΔB via numerical integration. Here, i is the zone number, which increases with distance from the cluster center: $i = 1$ corresponds to the central core, $i = 2$ to the inner core, $i = 3$ to the outer core, $i = 4$ to the inner corona, $i = 5$ to the corona, and $i = 6$ to the outer corona (we also introduced a zone $i = 7$ for one of the clusters). The quantities ΔN_i and ΔN_{tot} are statistically free of the effects of field stars and the projection of outer parts of the cluster onto inner regions. Our results are summarized in Table 1. Quantities with asterisks were obtained via linear extrapolation of the $\Delta f(r, \Delta B)$ curves slightly beyond their domains to the intersection with the radius of the corresponding zone $R_{i-1}(B)$. The table also gives the percentage of core stars of a given subsystem ΔN_{tot}. We adopted the radius $R_3(B)$ as the radius of the cluster core.

Let us now make some comments concerning the data listed in Table 1.

(1) The quantities $\Delta N_i(\Delta B)$ are nonadditive due to the $R_i = R_i(B)$ dependence for subsystems of faint stars when $B > N_{\text{tot}}$ [1–6]: the number of stars in a given zone $N_i(B)$ down to the limiting B magnitude cannot be determined via simple summation of the corresponding $\Delta N_i(\Delta B)$ down to this value.

(2) For several clusters, the $\Delta f(r, \Delta B)$ curves of many of their subsystems do not reach the center, since the cluster cannot be resolved into individual stars. We therefore did not determine the corresponding $\Delta N_1(\Delta B)$ and, to some extent, $\Delta N_2(\Delta B)$ values, and computed N_{tot} starting with some clustercentric distance r, indicated in Table 1. All this leads to underestimation of the reported percentages of stars in the cluster cores. In other words, most of the values listed in Table 1 are effectively lower limits for the corresponding percentages.

(3) For M56, we give only the integrated quantities $N_i(B)$ and $N_{\text{tot}}(B)$ and the integrated percentage

Table 2. D_r and D_f

NGC 6535		
ΔB	D_r	D_f
$14.0-16.0^m$	1.08	4.18
$16.0-18.0$	1.11	2.97
$16.0-19.0$	1.08	2.87
$19.0-20.0$	1.07	2.48
$20.0-21.0$	1.15	2.50*
$21.0-21.5$	–	–
NGC 5466		
$15.0-16.5$	0.97	3.07
$16.5-18.0$	1.00	2.22
$18.0-19.0$	1.06	3.28
$19.0-19.5$	0.95	3.07
$19.5-20.0$	0.89	2.50
$20.0-20.5$	0.90	2.43
$20.5-21.0$	0.91*	2.26*

Note: Asterisks indicate cases of extrapolation.

down to the given B magnitude as inferred from the integrated curves $f(r,B)$.

Figure 2 illustrates the results listed in Table 1.

The data presented here lead us to the following conclusions.

(1) The lower limit for the percentages of stars from various intervals ΔB in the cluster cores is no less than $50-60\%$. The only exception is M92. However, the low percentage in this case can be explained by the fact that stars of the central and inner core zones cannot be observed in this particular cluster.

(2) Most of the histograms shown in Fig. 2 remain approximately constant in the bright-star part of the B axis, despite strong fluctuations, and decrease somewhat in the faint-star domain. This confirms the relatively high percentage of bright stars in the cores of globular clusters, which must be due to a higher central concentration of these objects compared to faint stars, in agreement with the systematic variation of the cluster structure [1–6].

A comparison of the data for M56 with the histograms for other clusters in Fig. 2 is not possible, due to the nonadditive nature of $\Delta N_i(\Delta B)$ and $N_i(B)$ when $B > \bar{B}_{lim}$.

4. LOGARITHMIC DENSITY RANGE AND D_r AND D_f FOR NGC 6535 AND NGC 5466

NGC 6535 and NGC 5466 are the only clusters for which stellar density distribution curves reach the cluster centers for most subsystems. For these clusters, we used the numerical values $\Delta f(r,\Delta B)$ [3, 5] to construct the radial dependence of the density on a logarithmic scale. The resulting dependences are shown in Fig. 3, with the B-magnitude intervals indicated. We must bear in mind the following points.

(1) Due to the large heliocentric distance of NGC 5466, only a few subsystems with $B > \bar{B}_{lim}$ containing stars near and below the MS turnoff in the diagram $(V, B-V)$ can be observed. For NGC 6535, only the first four subsystems have $\Delta f(r,\Delta B)$ curves that reach the cluster center (Table 1).

(2) In the case of NGC 5466, we cannot be confident that we have accurately determined the cluster radius R_c; we therefore adopted $R_c = R_5$, with R_5 being determined with a high accuracy.

The overall similarity of the different subsystems is apparent from the logarithmic density curves in Fig. 3. This similarity must reflect general regularities in the structure of the clusters. The curves for the subsystems of the faintest stars usually come closer to the coordinate origin than those for subsystems of brighter stars. Here, it is impossible to tell whether the observed fluctuations of the curves for stars with different luminosities are real.

We also determined D_r and D_f as functions of the limiting B magnitude for NGC 5466 and NGC 6535. Note that, in accordance with [7], we take f_0 to be equal to the mean $\Delta f(r,\Delta B)$ in the central zone of the core and f_c to be equal to the mean $\Delta f(r,\Delta B)$ for the outermost corona region (zone $i = 5$ in both clusters). The results are shown in Fig. 3 and listed in Table 2. The last D_f values for $B = 21^m$ for NGC 5466 and NGC 6535 were obtained by extrapolating the $\Delta f(r,\Delta B)$ curve to the cluster center.

An analysis of Fig. 3 and Table 2 leads us to the following conclusions.

(1) In the case of NGC 5466, D_f is virtually independent of B down to $B \approx 19.5^m$, despite strong fluctuations whose nature is unclear. D_f shows a weak tendency to decrease at $B > 19.5^m$, which cannot be fully analyzed due to the insufficient amount of observational data.

(2) Similar conclusions for NGC 6535 can be made only if we ignore the D_f value for the brightest stars with $B < 16^m$. This D_f is anomalously high, apparently due to some peculiarity of the core of this cluster.

The results obtained are not surprising, and are consistent with the dependence of D_f on $\bar{m}$ for MS

stars presented by Kholopov [7]: according to stellar evolution theory, all stars above the MS turnoff have masses approximately equal to the masses of their progenitors near the turnoff. Assuming a large relaxation time τ for globular clusters, we expect these stars to maintain their spatial distributions (despite mass loss) so that the corresponding D_f vary only slightly with B. We expect the appearance of a mass–luminosity–spatial distribution relation for faint stars near and below the MS turnoff such that D_f begins to decrease with increasing B.

(3) The parameter D_r is independent of B and remains approximately constant (Table 2) within the errors of the technique employed, despite the $R_i = R_i(B)$ dependence in the clusters studied [1–6]. This can be explained by the homologous nature of the spatial structure of the clusters, since $r_0/R_c = R_1(B)/R_c(B) = \tilde{r}_1$, where $\tilde{r}_1$ is the relative radius of the central core zone normalized to $R_c(B)$, and this radius is independent of B for clusters with homologous structure.

5. CONCLUSIONS

In our opinion, the results presented in this paper are in good agreement with the observed variations of the spatial structure of the clusters studied and also with known correlations in the structures of star clusters.

REFERENCES

1. R. M. Rusev and Z. I. Peikov, Astron. Zh. **63**, 483 (1986) [Sov. Astron. **30**, 288 (1986)].
2. Z. I. Peikov and R. M. Rusev, Astron. Zh. **63**, 41 (1988) [Sov. Astron. **32**, 21 (1988)].
3. Z. I. Peikov and R. M. Rusev, Astron. Zh. **65**, 317 (1988) [Sov. Astron. **32**, 161 (1988)].
4. Z. I. Peikov and R. M. Rusev, Astron. Zh. **67**, 694 (1990) [Sov. Astron. **34**, 349 (1990)].
5. Z. I. Peikov and R. M. Rusev, Astron. Zh. **76**, 514 (1999) [Astron. Rep. **43**, 445 (1999)].
6. Z. I. Peikov and R. M. Rusev, Astron. Zh. **76**, 571 (1999) [Astron. Rep. **43**, 494 (1999)].
7. P. N. Kholopov, *Star Clusters* (Nauka, Moscow, 1981).
8. P. N. Kholopov, Astron. Zh. **45**, 1235 (1968) [Sov. Astron. **12**, 978 (1968)].
9. R. McClur and B. A. Twarog, Astrophys. J. **214**, 111 (1977).
10. B. A. Twarog, Astrophys. J. **220**, 890 (1978).
11. P. N. Kholopov, Astron. Zh. **45**, 786 (1968) [Sov. Astron. **12**, 625 (1968)].

Translated by A. Dambis

Model Radiation Spectrum for an Accretion Disk Near a Rotating Black Hole

A. F. Zakharov[1] and S. V. Repin[2]

[1]*Institute of Theoretical and Experimental Physics, Moscow, Russia*

[2]*Space Research Institute, Russian Academy of Sciences, ul. Profsoyuznaya 84/32, Moscow, 117810 Russia*

Received July 20, 2001; in final form October 19, 2001

Abstract—ASCA, RXTE, and Chandra observations of Seyfert galaxies indicate the presence in their spectra of broad emission lines with characteristic double-peaked profiles, which could arise in the inner regions of an accretion disk. In such regions, general relativistic effects must be taken into account, and may even dominate. In connection with this, we have constructed the radiation spectrum for an individual spectral line for a model isothermal Kerr accretion disk. This demonstrates the manifestation of general relativistic effects in pure form, unclouded by effects associated with models for the structure of the disk itself. It is assumed that matter in the disk moves in circular geodesics in the equatorial plane. The spectrum retains a characteristic two-peaked profile for wide ranges of values of the radial coordinate of the radiating region, angular momentum of the black hole, and viewing angle. The inner regions of the disk make an appreciable contribution to the red wing of the spectrum. © *2002 MAIK "Nauka/Interperiodica".*

1. INTRODUCTION

X-ray observations of Seyfert galaxies carried out using instruments on board the ASCA, RXTE, Chandra and other spacecraft [1−8] reveal the presence of broad iron K_α (∼6.4 keV) emission lines in their spectra, as well as a number of other weaker emission lines of other elements. In observations with sufficiently good spectral resolution, these lines display a characteristic two-peaked profile [2, 9], with a high blue and low red maximum and an extended red wing that gradually approaches the background level. The Doppler widths of the lines (a somewhat conditional concept, since the line profiles are far from Doppler) correspond to velocities of tens of thousand of km/s. Currently, the maximum velocity $v \approx 80\,000-100\,000$ km/s [2] has been measured for the galaxy MCG−6−30−15, while $v \approx 48\,000$ km/s [10] has been measured for MCG−5−23−16. The line profiles for both these galaxies are also known, although the profile for MCG−5−23−16 is less certain.

With such high velocities of motion, it is natural to suppose that the K_α line forms in the inner regions of an accretion disk, at distances ∼$(1-3)r_g$ from the black hole. Recall that the last stable circular orbit around a nonrotating black hole, whose gravitational field is described by a Schwarzschild metric, is $3r_g$ from the black hole. For this reason, that is precisely the rotation of the black hole that is important to us here. The ability to observe radiation from matter

in such strong gravitational fields enables tests of general relativity and modeling of the conditions in the accretion disk, as well as studies of astrophysical phenomena associated with extreme conditions, such as the formation of jets [11, 12] and the detection of gravitational radiation.

In connection with increased interest in these areas, a large amount of observational material has recently appeared and is in need of interpretation. For example, the results of monitoring NGC 7469 in the ultraviolet are presented in [13]. In [14], H_α observations in the optical are compared with X-ray observations of the K_α line. In some cases, rapid variations in the profile of the K_α line [15] (NGC 7314), strong X-ray variability [16], and quasi-periodic oscillations [17] (GRS 1915+105) have been detected. General relativistic numerical modeling of various observational factors associated with the shape of the K_α line have been carried out, for example, in [14, 18−23].

In the current paper, we use an approach based on numerical simulations of the motion of photons radiated by an individual hot spot moving in a circular geodesic in the equatorial plane. This method was used earlier [24−27] in general relativistic modeling of the spectra and variability of emission from hot spots in an accretion disk. The disk spectrum is obtained by integrating along the radial coordinate.

2. EQUATION OF MOTION OF PHOTONS IN A KERR FIELD

Many astrophysical processes that involve the active release of energy are associated with black holes. The vast majority of observed astronomical objects, such as stars and galaxies, rotate. There is no doubt that black holes should share this property. It is known that stationary black holes are described by a Kerr metric, which in geometrical units ($G = c = 1$) and Boyer–Lindquist coordinates (t, r, θ, ϕ) has the form [28, 29]:

$$ds^2 = -\frac{\Delta}{\rho^2} \left(dt - a \sin^2 \theta d\phi \right)^2 \qquad (1)$$

$$+ \frac{\sin^2 \theta}{\rho^2} \left[\left(r^2 + a^2 \right) d\phi - a dt \right]^2 + \frac{\rho^2}{\Delta} dr^2 + \rho^2 d\theta^2$$

or

$$ds^2 = -\left(1 - \frac{2Mr}{\rho^2} \right) dt^2 + \frac{\rho^2}{\Delta} dr^2 + \rho^2 d\theta^2 \qquad (2)$$

$$+ \left(r^2 + a^2 + \frac{2Mra^2}{\rho^2} \sin^2 \theta \right) \sin^2 \theta d\phi^2$$

$$- \frac{4Mra}{\rho^2} \sin^2 \theta d\phi dt,$$

where

$$\rho^2 = r^2 + a^2 \cos^2 \theta,$$

$$\Delta = r^2 - 2Mr + a^2.$$

The constants M and a determine the parameters of the black hole: M denotes its mass, and $a = S/M$, its specific angular momentum.

The equations of motion of particles in a Kerr field can be obtained [28–30] by separating variables in the Hamilton–Jacobi equation

$$g^{ik} \frac{\partial S}{\partial x^i} \frac{\partial S}{\partial x^k} - m^2 = 0. \qquad (3)$$

As was shown in [25, 27], the equation of motion of a photon ($m = 0$) reduces to a system of six ordinary first-order differential equations:

$$\frac{dt'}{d\sigma} = -\hat{a} \left(\hat{a} \sin^2 \theta - \xi \right) + \frac{\hat{r}^2 + \hat{a}^2}{\hat{\Delta}} \left(\hat{r}^2 + \hat{a}^2 - \xi \hat{a} \right), \quad (4)$$

$$\frac{d\hat{r}}{d\sigma} = r_1, \qquad (5)$$

$$\frac{dr_1}{d\sigma} = 2\hat{r}^3 + \left(\hat{a}^2 - \xi^2 - \eta \right) \hat{r} + (\hat{a} - \xi) + \eta, \quad (6)$$

$$\frac{d\theta}{d\sigma} = \theta_1, \qquad (7)$$

$$\frac{d\theta_1}{d\sigma} = \cos \theta \left(\frac{\xi^2}{\sin^3 \theta} - \hat{a}^2 \sin \theta \right), \qquad (8)$$

$$\frac{d\phi}{d\sigma} = -\left(\hat{a} - \frac{\xi}{\sin^2 \theta} \right) + \frac{\hat{a}}{\hat{\Delta}} \left(\hat{r}^2 + \hat{a}^2 - \xi \hat{a} \right) \quad (9)$$

with the two first integrals

$$\epsilon_1 \equiv r_1^2 - \hat{r}^4 - \left(\hat{a}^2 - \xi^2 - \eta \right) \hat{r}^2 \qquad (10)$$

$$- 2 \left[(\hat{a} - \xi)^2 + \eta \right] \hat{r} + \hat{a}^2 \eta = 0,$$

$$\epsilon_2 \equiv \theta_1^2 - \eta - \cos^2 \theta \left(\hat{a}^2 - \frac{\xi^2}{\sin^2 \theta} \right) = 0, \qquad (11)$$

where $\eta = Q/M^2 E^2$, $\xi = L_z/ME$ is the Chandrasekhar constant [31], and a hat over a letter indicates that the corresponding physical quantity appears in the equation in dimensionless form. The system of equations written in this way does not have singularities, in contrast to traditional forms of the equations of motion [28, 29] in the form of a system of four equations (one for each coordinate).

The qualitative analysis conducted in [32, 33] showed that the type of motion experienced by photons can change fundamentally in the presence of fairly small parameter variations. Accordingly, in such cases, standard analyses of geodesics associated with the computation of elliptical integrals can lead to large numerical errors. The numerical integration of such geodesics and their very complex appearance are presented in [34].

Solving the system (4)–(9) for photons radiated by a hot spot moving along a geodesic in the equatorial plane, we can obtain the spectrum of the spot that will be detected by a distant observer viewing the disk at various angles θ. It is convenient to carry out the numerical integration using a combination of the methods of Gear [35] and Adams, realized in [36–38]. As indicated above, the disk spectrum is derived via integration along the radial coordinate.

3. MODEL OF THE DISK RADIATION

To construct the disk spectrum, we must adopt some model for the radiation of the disk itself. For example, we could use the classical α-disk model presented in [39, 40]. However, a drawback of this approach is that the result will be strongly model dependent. Therefore, we would like to adopt more robust assumptions with regard to the structure of the disk, in order to demonstrate the influence of general relativistic effects in their pure form. This should enable us to identify the contributions of general relativistic effects to the disk spectrum and to separate them from the manifestation of other factors, such as the radial temperature distribution, the presence of a radiating corona above the disk, the effects of advection-dominated accretion flows, etc.

In accordance with these requirements, we will take the disk to lie in the equatorial plane of a Kerr black hole. We assume that the disk itself is infinitely thin; i.e., it does not have a physical thickness. In

addition, we assume that each disk surface element radiates isotropically into a solid angle of 2π in a locally inertial frame. Finally, we assume that all disk elements have the same temperature, which is thus constant and independent of the radial coordinate.

The question of whether such disks are realized in actual astrophysical objects is not considered here. However, we note that the conditions indicated would be fulfilled to an appreciable extent if such a disk were made up of dust-like material (with equation of state $p = 0$) and the entire system were isolated and only weakly interacted with surrounding objects.

Under these assumptions, the disk can occupy a system of narrow rings, the spectrum of each of which can be obtained by solving the system (4)–(9) for photons radiated by a hot spot moving in a circular geodesic in the equatorial plane [27]. Multiplying the resulting spectrum by the area of the ring, we obtain the contribution of this ring to the spectrum of the disk as a whole. Finally, the spectrum of the disk itself is derived by summing the contributions of individual rings, which, of course, is equivalent to integrating over the radial coordinate.

However, the area of a ring with width dr is not expressed in a Kerr field by the usual formula

$$dS(r) = 2\pi r\, dr.$$

In order to obtain the correct expressions, we must, for example, write the spatial metric tensor

$$\gamma_{\alpha\beta} = -g_{\alpha\beta} + \frac{g_{0\alpha}g_{0\beta}}{g_{00}}, \qquad (12)$$

which in a Kerr field has the form

$$dl^2 = \frac{\rho^2}{\Delta}\,dr^2 + \rho^2 d\theta^2 + \frac{\sin^2\theta}{\rho^2 - rr_g}\rho^2\Delta d\phi^2. \quad (13)$$

Hence, the area of a ring with width dr is obtained by integrating the area element

$$dS(r,\phi) = \sqrt{g_{rr}g_{\phi\phi}}\,dr\,d\phi$$

over the angular coordinate:

$$dS(r) = \int_0^{2\pi} \left(\sqrt{g_{rr}g_{\phi\phi}}\,dr\right) d\phi \qquad (14)$$

$$= 2\pi\sqrt{\frac{\rho^2}{\Delta}\frac{\sin^2\theta}{\rho^2 - rr_g}\rho^2\Delta}\,dr$$

$$= \frac{2\pi\rho^2\sin\theta}{\sqrt{\rho^2 - rr_g}}\,dr = \frac{2\pi\left(r^2 + a^2\sin^2\theta\right)\sin\theta}{\sqrt{r^2 - rr_g + a^2\sin^2\theta}}\,dr.$$

In the equatorial plane, $\sin\theta = 1$, which finally gives for the area of ring

$$dS(r) = \frac{2\pi\left(r^2 + a^2\right)}{\sqrt{r^2 - rr_g + a^2}}\,dr. \qquad (15)$$

We note in passing that this quantity has an extremum, which turns out to be a local minimum. The position of this minimum can be found from the solution of the third-degree algebraic equation

$$2r^3 - 3r_g r^2 + 2a^2 r + r_g a = 0, \qquad (16)$$

which is obtained by differentiating (15) in the radial coordinate. The solution of this equation yields

$$r_{\min} = 2\sqrt{\frac{3 - a^2}{3}} \qquad (17)$$

$$\times \cos\left(\frac{1}{3}\arccos\frac{1 - a^2}{\sqrt{-\dfrac{a^6}{27} + \dfrac{a^4}{3} - a^2 + 1}}\right) + 1.$$

This root corresponds to the position of particles below the horizon.

4. MODELING RESULTS

Figure 1 shows the model spectrum for the radiation of an individual monochromatic spectral line in an accretion disk with $a = 0.9$ and the radiating region extending from $10\,r_g$ to the last stable orbit. Such a line should be detected by a distant observer. The intensity of the radiation, plotted along the vertical axis, is expressed in terms of the relative number of photons with a given frequency detected by a distant observer (and not the total energy of these photons!). If we wish to obtain the spectral energy distribution, these plots must be corrected in accordance with the formula $E = h\nu$. In this case, the red wing will become even weaker and the blue wing stronger.

Like the spectrum of a hot spot, the spectrum of a disk has a characteristic two-peaked profile with a high blue and low red maximum. However, compared to the spectrum of a hot spot, we see here a number of important features. For example, both the blue and red edges of the spectrum become smooth and fall slowly to the background level. This is especially true of the red wing, which becomes very extended, so that the ratio of the wavelength of the reddest of the observed photons to the wavelength of the red maximum exceeds five (this cannot be seen directly in the plots, due to their small scale). In spite of this, the blue maximum is very narrow, especially for large values of θ.

It is also interesting to trace the position of the maximum as the disk inclination θ varies. At small θ, the frequency of the maximum is lower than the laboratory frequency. For example, for photons emitted perpendicular to the disk plane ($\theta = 0°$), $\nu_{\max} \approx 0.85\,\nu_{\text{lab}}$. This is the result of the joint action of the transverse Doppler effect and the gravitational redshift. At large θ, the frequency of the maximum
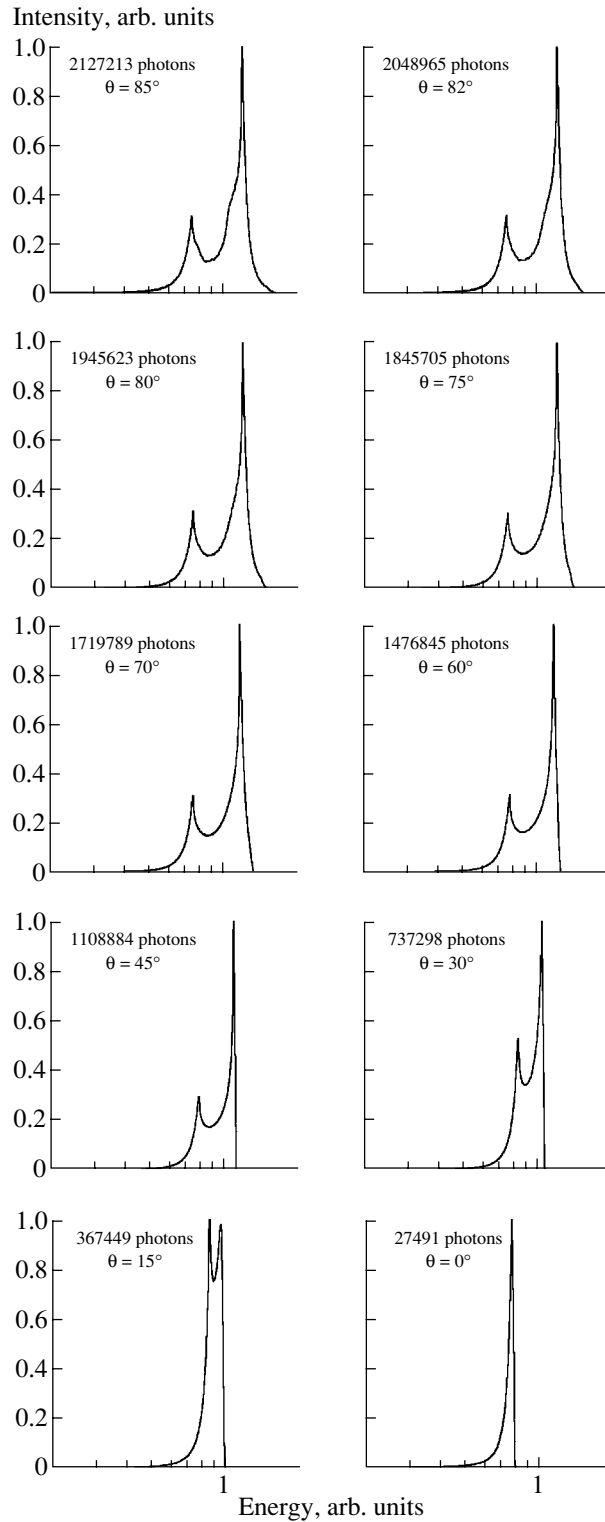
Fig. 1. Spectrum of a line in an isothermal disk with $a = 0.9$ observed for various angles θ. The intensity of the radiation is expressed in terms of the relative number of photons in the corresponding energy range. The last stable orbit is at $r = 1.16\,r_g$.

is higher than the laboratory frequency. For example, when $\theta = 60°$ $\nu_{max} \approx 1.1\nu_{lab}$. Here, the longitudinal Doppler effect is stronger than the combined action of the transverse Doppler effect and the gravitational redshift. Finally, when $\theta \approx 30°$, the maximum occurs precisely at the laboratory frequency for a fairly broad

dN/dΩ, arb. units
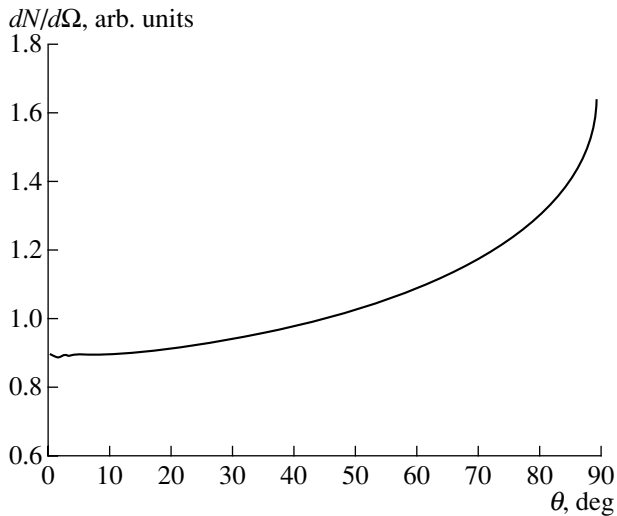
Fig. 2. The density of photons $dN/d\Omega$ detected by a distant observer for a disk with $a = 0.9$ and various angles θ. The value for $\theta = 45°$ is arbitrarily set equal to unity. The somewhat monotonic behavior near zero is associated with the statistically small number of such photons.

range of a values. In this case, the contributions of the three effects indicated above compensate each other. Precisely this case is most common in observations of real astrophysical objects. In particular, this is the case for the Seyfert galaxies MCG-6-30-15 and MCG-5-23-16 [10], for which there exist good observations.

It is also interesting to note the variation in the angular distribution of the emitted photons. Recall that the initial distribution in the comoving locally inertial reference frame was isotropic. However, as we can see in Fig. 2, a distant observer does not detect such an isotropic distribution. Photons arrive more rarely from the direction perpendicular to the plane of the disk and more often from the direction parallel to this plane. This same result can crudely be obtained from Fig. 1. Here, each plot indicates the total number of detected photons in a narrow range of θ near the nominal angle. The number of photons decreases as θ decreases, but it is easy to verify that this decrease is appreciably more rapid than the variation of the area of a ring with width $d\theta$ on the surface of a sphere. Figure 2 presents the result for $a = 0.9$. For a disk with $a = 0.99$ and outer and inner edges lying at $r_{\text{out}} = 10\,r_g$ and at the last stable orbit, the ratio of the densities of photons emitted parallel and perpendicular to the disk exceeds 1.8.

5. DISCUSSION

The modeling results show that the disk spectrum depends substantially on the inclination of the disk. When $\theta \sim 0°$, we obtain a narrow and high maximum

that is slightly redshifted. At larger values of θ, the spectrum acquires a characteristic two-peaked profile with a very extended red wing. The main contribution to this wing is made by the inner regions of the disk, located near the last stable orbit, for which the contributions of the Doppler effect and the gravitational redshift are additive.

Another distinctive feature of the spectrum is the presence of a high and narrow blue maximum, which remains narrow for virtually any disk inclination. Over a broad range in θ, the red maximum remains approximately a factor of three weaker than the blue maximum in terms of the density of the detected photons (and a factor of five to six weaker in terms of the detected energy) and also somewhat broader than the blue maximum. A number of fundamental difficulties can arise in attempts to detect such a feature of the spectrum observationally. For example, if the blue maximum exceeds the background noise level by no more than a factor of three in terms of the number of detected photons, the red maximum will be completely invisible, leading to erroneous interpretations of the observations, since the frequency of the blue peak does not coincide with the laboratory frequency. In this sense, instruments operating in a photon-counting regime have some advantage over those that measure the total energy in some narrow range. If we also take into account the fact that instruments usually have different sensitivities at different energies, and that this function itself will change when the instrument has spent a long time in space, we can understand the extreme difficulties potentially hindering a correct interpretation of the observational results.

Comparing the results in Figs. 1 and 2, we note that, in spite of the isotropy of the radiation in the locally inertial reference frame, a large fraction of the photons are detected by observers located near the equatorial plane. Moreover, this effect is enhanced as the radius of the circular orbit is decreased. An observer located at the pole ($\theta \sim 0°$)—i.e., experiencing fairly ideal conditions for observations—sees primarily regions of the disk that are far from the central black hole ($r \approx 3-5r_g$). Another observer located in the equatorial plane ($\theta \sim 90°$) sees regions that are closer to the center ($r \approx 0.5-1.5r_g$), where there is a strong gravitational field so that we expect the most interesting manifestations of strong general relativistic effects. Of course, the possibility of conducting such observational studies depends strongly on the model of the disk: its geometry, its physical nature, the presence of an opaque corona, etc. However, we cannot exclude the existence in nature of astrophysical objects in which thin accretion disks can be observed nearly edge-on. This would enable the long-awaited

possibility of directly observing the behavior of matter in a strong gravitational field.

REFERENCES

1. A. C. Fabian, K. Nandra, C. S. Reynolds, *et al.*, Mon. Not. R. Astron. Soc. **277**, L11 (1995).
2. Y. Tanaka, K. Nandra, A. C. Fabian, *et al.*, Nature **375**, 659 (1995).
3. K. Nandra, I. M. George, R. F. Mushotzky, *et al.*, Astrophys. J. **476**, 70 (1997).
4. K. Nandra, I. M. George, R. F. Mushotzky, *et al.*, Astrophys. J. **477**, 602 (1997).
5. A. Malizia, L. Bassani, J. B. Stephen, *et al.*, Astrophys. J., Suppl. Ser. **113**, 311 (1997).
6. R. M. Sambruna, I. M. George, R. F. Mushotsky, *et al.*, Astrophys. J. **495**, 749 (1998).
7. T. Yaqoob, I. M. George, K. Nandra, *et al.*, Astrophys. J. **546**, 759 (2001).
8. P. M. Ogle, H. L. Marshall, J. C. Lee, *et al.*, Astrophys. J. Lett. **545**, L81 (2000).
9. T. Yaqoob, B. McKernan, A. Ptak, *et al.*, Astrophys. J. Lett. **490**, L25 (1997).
10. K. A. Weaver, J. H. Krolik, and E. A. Pier, Astrophys. J. **498**, 213 (1998); astro-ph/9712035.
11. M. M. Romanova, G. V. Ustyugova, A. V. Koldoba, *et al.*, Astrophys. J. **500**, 703 (1998).
12. R. V. E. Lovelace, W. I. Newman, and M. M. Romanova, Astrophys. J. **484**, 628 (1997).
13. I. Wanders *et al.*, Astrophys. J., Suppl. Ser. **113**, 69 (1997).
14. J. W. Sulentic, P. Marziani, T. Zwitter, *et al.*, Astrophys. J. **501**, 54 (1998).
15. T. Yaqoob, P. J. Serlemitsos, T. J. Turner, *et al.*, Astrophys. J. Lett. **470**, L27 (1996).
16. J. W. Sulentic, P. Marziani, and M. Calvani, Astrophys. J. Lett. **497**, L65 (1998).
17. B. Paul, P. C. Agrawal, A. R. Rao, *et al.*, Astrophys. J. Lett. **492**, L63 (1998).
18. G. Matt, G. C. Perova, L. Piro, and L. Stella, Astron. Astrophys. **475**, 57 (1992).
19. B. C. Bromley, K. Chen, and W. A. Miller, Astrophys. J. **475**, 57 (1997).
20. W. Cui, S. N. Zhang, and W. Chen, Astrophys. J. Lett. **492**, L53 (1998).
21. V. I. Pariev and B. C. Bromley, in *Proceedings of the 8th Annual October Astrophysics Conference, Maryland, 1997*; astro-ph/9711214.
22. V. I. Pariev and B. C. Bromley, Astrophys. J. **508**, 590 (1998).
23. B. C. Bromley, W. A. Miller, and V. I. Pariev, Nature **391**, 54 (1998).
24. A. F. Zakharov, Preprint MPA 755 (1993).
25. A. F. Zakharov, Mon. Not. R. Astron. Soc. **269**, 283 (1994).
26. A. F. Zakharov, in *Proceedings of the 17th Texas Symposium on Relativistic Astrophysics,* Ed. by H. Bohringer, G. E. Morfill, and J. E. Trumper (The New York Academy of Science, New York, 1995); Ann. N. Y. Acad. Sci. **759**, 550 (1995).
27. A. F. Zakharov and S. V. Repin, Astron. Zh. **76**, 803 (1999) [Astron. Rep. **43**, 705 (1999)].
28. C. W. Misner, K. S. Thorne, and J. A. Wheeler, *Gravitation* (Freeman, San Francisco, 1973; Mir, Moscow, 1977).
29. L. D. Landau and E. M. Lifshitz, *The Classical Theory of Fields* (Nauka, Moscow, 1998; Pergamon, Oxford, 1975).
30. B. Carter, Phys. Rev. D **174**, 1559 (1968).
31. S. Chandrasekhar, *The Mathematical Theory of Black Holes* (Clarendon Press, Oxford, 1983; Mir, Moscow, 1986).
32. A. F. Zakharov, Zh. Éksp. Teor. Fiz. **91**, 3 (1986) [Sov. Phys. JETP **64**, 1 (1986)].
33. A. F. Zakharov, Zh. Éksp. Teor. Fiz. **95**, 385 (1989) [Sov. Phys. JETP **68**, 217 (1989)].
34. A. F. Zakharov, Astron. Zh. **68**, 58 (1991) [Sov. Astron. **35**, 30 (1991)].
35. C. W. Gear, *Numerical Initial Value Problems in Ordinary Differential Equations* (Prentice Hall, Englewood Cliffs, 1971).
36. A. C. Hindmarsh, in *In Scientific Computing,* Ed. by R. S. Stepleman *et al.* (North-Holland, Amsterdam, 1983), p. 55.
37. L. R. Petzold, SIAM J. Sci. Stat. Comput. **4**, 136 (1983).
38. K. L. Hiebert and L. F. Shampine, Sandia Report sand80-0180 (February, 1980).
39. I. D. Novikov and K. S. Thorne, in *Black Holes,* Ed. by C. De Witt and B. S. De Witt (Gordon and Breach, New York, 1973), p. 334.
40. N. I. Shakura and R. A. Sunyaev, Astron. Astrophys. **24**, 337 (1973).

Translated by D. Gabuzda

Non-Steady-State Accretion Disks in X-Ray Novae: Outburst Models for Nova Monocerotis 1975 and Nova Muscae 1991

G. V. Lipunova[1] and N. I. Shakura[1, 2]

[1]Sternberg Astronomical Institute, Universitetskiĭ pr. 13, Moscow, 119899 Russia
[2]Max Planck Institut for Astrophysics, Garching, Germany
Received June 25, 2001; in final form September 13, 2001

Abstract—We have fit outbursts of two X-ray novae (Nova Monocerotis 1975 = A 0620−00 and Nova Muscae GS 1991 = 1124−683) using a non-steady-state accretion-disk model. The model is based on a new solution for a diffusion-type equation for non-steady-state accretion and describes the evolution of a viscous α disk in a binary system after the peak of the outburst, when the matter in the disk is totally ionized. The accretion rate in the disk decreases according to a power law. We derive formulas for the accretion rate and effective temperature of the disk. The model has three free input parameters: the mass of the central object M, the turbulence parameter α, and the normalization parameter δt. The results of the modeling are compared with the observed X-ray and optical B and V light curves. The estimates for the turbulence parameter α are similar: 0.2−0.4 for A 0620−00 and 0.45−0.65 for GS 1124−683, suggesting a similar nature for the viscosity in the accretion disks around the compact objects in these sources. We have also derived the distances to these systems as functions of the masses of their compact objects. © 2002 MAIK "Nauka/Interperiodica".

1. INTRODUCTION

Accretion provides an efficient mechanism for energy release in stellar systems, which is what makes many astrophysical objects observable. Accretion occurs in a disk, provided that the matter captured by the gravitation of the central body possesses nonzero angular momentum relative to this body. This is true, for example, in binaries, where the angular momentum is associated with the orbital rotation of the components. In the course of accretion onto a compact object whose radius is comparable to the gravitational radius, a substantial fraction of the total energy of the accreted matter mc^2 is released.

Outbursts reflect one of the most fundamental properties of accretion: its non-steady-state character. Currently, a number of different models are proposed to explain non-steady-state processes in accretion disks and to describe the observed source variability. One problem is to find an adequate description for the viscosity in the accretion disk: viscosity is essential for accretion, and the viscosity parameters specify the non-steady-state character of the processes involved.

In [1], a new solution for the basic equation of non-steady-state disk accretion was found and applied to a model of an α accretion disk around the components of a close binary. One important property of the disk in a binary system is that its radius is finite. Angular momentum is carried away from the outer boundary

of the disk due to tidal forces, so that the rotation of outer parts of the disk is synchronized with the rotation of the secondary. It is assumed that the size of the accretion disk specified by tidal interaction is constant over the time interval considered. Another assumption is that the rate of mass transfer from the secondary to the disk is small compared to the rate of accretion within the disk.

This condition is satisfied, for example, in an X-ray nova outburst. The accretion rate in the disk during the outburst reaches tenths of the Eddington rate (10^{-9} $(M/M_\odot)\theta$ $M_\odot$/yr, where θ is the accretion efficiency and M is the mass of the central object) or more, while the observed rate of mass transfer from the companion in quiescent periods is $10^{-11}-10^{-12}$ $M_\odot$/yr [2, 3]. X-ray novae are low-mass binaries containing a black hole or neutron star (see, for example, [3]). The other component, a low-mass dwarf, fills its Roche lobe, so matter continuously flows into the disk around its companion [3].

Currently, more than 30 X-ray novae are known [3]. Most have light curves with similar exponentially decreasing profiles [4]. The intensity increases by a factor of 10^2-10^6 over several days, whereas the exponential decrease of the light curve lasts for several months, with a characteristic time of about 30−40 days.

There are two types of mechanisms for X-ray nova outbursts: disk instability and unstable mass transfer

from the secondary. A final choice between them has not been made, and each type of model faces some problems (see, for example, [3]). In disk-instability models, during the outburst, the central object accretes matter accumulated by the disk over decades of the quiescent state. This idea is supported by the fact that the mass-transfer rate in quiescent periods is comparable to the outburst energy divided by the time between outbursts [2].

In any case, an important point here is that we assume the presence of a standard disk at the time of maximum brightness of the source, as is confirmed by spectral observations [2]. By "standard," we mean a nonmonochromatic α disk whose inner radius coincides with the last stable orbit around the black hole, with the velocity of radial motion of material being small compared to other characteristic velocities in the disk. Then, the solution of [1] can be applied to the decay of an X-ray nova outburst. The light curve calculated using the resulting solution is consistent with observations when the contribution of the accretion disk dominates the soft X-ray radiation of the system. This phase is characterized by a definite spectral state and can be distinguished in the evolution of an X-ray nova.

Modeling of the light curves of an X-ray nova in several X-ray and optical bands can be used to derive the basic parameter of the disk—the turbulence parameter α (this is a new, independent method for determining α in astrophysical disks), as well as the relationship between the distance and mass of the compact component.

Here, we apply this type of model to Nova Monocerotis A 0620−00, which is the brightest nova in X-rays observed to the present time, and Nova Muscae GS 1124−683[1].

Currently, the most likely mechanism for turbulence and angular-momentum transfer in accretion disks is thought to be Velikhov−Chandrasekhar magnetic−rotational instability [5, 6], which was developed for application to accretion disks by Balbus and Hawley [7]. Calculations suggest that this type of instability corresponds to $\alpha \sim 10^{-2}$. The parameter α, which was introduced by Shakura [10], describes large-scale turbulent motions. The large-scale development of MHD turbulence has been simulated, for example, in [8, 9], where it was estimated that $\alpha \sim 10^{-1}$.

On the other hand, the following estimates for α were derived in comparisons between theory and observations: ~ 0.1 during outburst and ~ 0.02 in the

quiescent state for dwarf novae in a model with instability of a limiting cycle in dwarf novae (see, for example, [11]); $\sim 10^{-2}$ for disks in galactic nuclei [12]; ~ 1 for Sgr A in an advection-dominated model [13]; and $\sim 0.1 - 0.3$ in the inner, hot advective part of the disk for the X-ray novae GS 1124−683, A 0620−00, and V 404 Cyg based on spectra in the low state [14].

2. MODEL FOR ACCRETION DISKS IN X-RAY NOVAE

The evolution of a viscous accretion disk is described by the diffusion-type nonlinear differential equation [15]:

$$\frac{\partial F}{\partial t} = D\frac{F^m}{h^n}\frac{\partial^2 F}{\partial h^2}, \qquad (1)$$

where $F = W_{r\varphi}\, r^2$ is the total moment of the viscous forces acting between adjacent rings of the disk divided by 2π, $W_{r\varphi}$ is the component $w_{r\varphi}$ of the viscous stress tensor integrated over the thickness of the disk, $h = \sqrt{GMr}$ is the specific angular momentum, and M is the mass of the central object. The dimensionless constants m and n depend on the type of opacity in the disk. If the opacity is determined largely by absorption (free−free and bound−free transitions), then $m = 3/10$ and $n = 4/5$. The "diffusion coefficient" D specified by the vertical structure of the disk relates the surface density Σ, F, and h [15, 16]:

$$\Sigma = \frac{(GM)^2\, F^{1-m}}{2\,(1-m)\,D\,h^{3-n}}. \qquad (2)$$

Relation (2) is derived from an analysis of the vertical structure of the disk.

A class of solutions for (1) was derived in [16] during studies of the evolution of a torus of matter around a gravitating center under the action of viscous forces described by the turbulent viscosity α introduced in [10]. In particular, a solution was obtained for the stage when the torus has evolved to an accretion-disk configuration, from which matter flows onto the central object. When the rate of accretion through the inner edge decreases, the outer radius of the disk simultaneously increases—the matter carries angular momentum away from the center. In this model, the accretion rate decreases with time in accordance with a power law. The power-law index depends on the type of opacity in the disk.

An important property of a model non-steady-state disk in a binary system is the cutoff of the disk at an outer radius, in the region where the angular momentum is carried away in the course of the orbital motion (see, for example, [17]). Taking into account the corresponding boundary conditions, we obtained a new solution for Eq. (1) [1] in a general form for

---

[1] Observations collected from the literature and reduced to a common system can be found at http://xray.sai.msu.ru/galja/xnov/.

a disk with uniform opacity. We describe the vertical structure using calculations from [19] in the framework of the generally accepted α-disk model [18]. Following [16], we considered two opacity regimes: with the dominant contributions to the opacity made by Thomson scattering of photons on free electrons, and by free–free and bound–free transitions in the plasma. As a result, we obtained explicit expressions describing the time variations of the physical parameters of the accretion disk. The solution describes the evolution of the accretion disk in a binary during the decay after the outburst while the matter in the disk remains completely ionized. The accretion rate decreases with time according to a power law; however, in this case, the power-law index is larger than for the solution of [16]: $-5/2$ compared to $-19/16$ when Thomson scattering dominates and $-10/3$ compared to $-5/4$ when absorption dominates. The solutions in the two opacity regimes join smoothly, providing a basis for applying a combined solution to describe the evolution of a disk with a realistic opacity. Our study of disks in stellar binary systems indicates that the second opacity regime is realized in practice.

The law for the variation of the accretion rate can be easily derived from the condition of mass conservation in the disk. Let a Keplerian α disk in a binary have fixed inner and outer radii r_{in} and r_{out}. The mass of the disk is $M_{\mathrm{d}} = \int_{r_{\mathrm{in}}}^{r_{\mathrm{out}}} 2\pi r \Sigma \mathrm{d}r$. If this mass varies only due to accretion through the inner disk boundary (i.e., the accretion rate onto the outer boundary is substantially lower), then $\mathrm{d}M_{\mathrm{d}}/\mathrm{d}t = \dot{M}_{\mathrm{in}}(t)$. Let the disk parameters F and Σ be represented as the products $F(t)f(\xi)$ and $\Sigma(t)\sigma(\xi)$, where $f(\xi)$ and $\sigma(\xi)$ are dimensionless functions of the radial coordinate $\xi = h/h_{\mathrm{o}}$. The value of h_{o} is fixed and equal to the angular momentum at the outer disk boundary. Let us express the surface density Σ in the integrand in terms of F using (2). It follows from the equation for the angular-momentum transfer that $\dot{M}_{\mathrm{in}}(t) = -2\pi F(t)f'(\xi)/h_{\mathrm{o}}$ [1]; therefore we obtain

$$M_{\mathrm{d}} = -\dot{M}_{\mathrm{in}}^{1-m} \int_{r_{\mathrm{in}}}^{r_{\mathrm{out}}} \left(\frac{h_{\mathrm{o}}f(\xi)}{2\pi y(\xi)} \right)^{1-m} \quad (3)$$

$$\times \frac{\pi(GM)^2}{(1-m)Dh^{3-n}} r\mathrm{d}r = (\mathrm{d}M_{\mathrm{d}}/\mathrm{d}t)^{1-m} \times \mathrm{const},$$

where the dimensionless $y(\xi) = f'(\xi)$. We will integrate (3) over t. Using the fact that $m = 10/3$ for a Kramers law, we conclude that $M_{\mathrm{d}} \propto (t + \delta t)^{-7/3}$ and $\dot{M}_{\mathrm{in}} \propto (t + \delta t)^{-10/3}$. Note that, for the given time dependence, it is sufficient that the diffusion coefficient D be constant in time, being also a function of

the radius. In [1], the complete solution for a non-steady-state disk was found; i.e., the dimensionless functions of the coordinate were determined for the case $D = \mathrm{const}$.

The bolometric luminosity $L = \theta\dot{M}c^2$ varies according to the same law as the rate of accretion through the inner disk radius. As was shown in [1], the exponential light curve of an X-ray nova can be understood if the considered frequency interval contains the flux integrated over the exponential falloff in the Wien section of the disk spectrum rather than a fixed fraction of the bolometric luminosity.

In the model for a non-steady-state disk considered, the accretion rate depends on the distance to the center. In the central regions, this enables us to assume the accretion rate to be independent of the radius in all basic formulas for calculation of the X-ray flux. The bolometric flux from regions of the disk between rings with radii $0.1r_{\mathrm{out}}$ and r_{out} is $\approx 6\%$ lower than the values obtained for a steady-state standard disk model. The optical flux from the non-steady-state disk differs from that from a steady-state disk by a smaller amount, depending on the size of the primary region of radiation of the optical flux. This size is specified by the mass of the central object and the accretion rate in the disk.

To take into account the effects of general relativity in the vicinity of the compact object, we used a modified Newtonian gravitational potential in the form suggested by Paczyński and Wiita [20]. For a Schwarzschild black hole, this potential is

$$\psi = \frac{GM}{r - r_{\mathrm{g}}}, \quad (4)$$

where $r_{\mathrm{g}} = 2GM/c^2$. The accretion efficiency θ for this potential is a factor of ≈ 1.45 smaller than for a Newtonian potential.

3. MODELING PROCEDURE

3.1. Derivation of Theoretical Curves

In the model for a non-steady-state disk in a binary system [1], with the opacity specified by bremsstrahlung absorption, the variation of the accretion rate in the disk as a function of time is given by the formula

$$\dot{M}(h,t) = -2\pi \frac{1.214y(h/h_{\mathrm{o}})}{h_{\mathrm{o}}} \left(\frac{h_{\mathrm{o}}^{14/5}}{D(t+\delta t)} \right)^{10/3}, \quad (5)$$

where t is time, δt a normalizing shift, h the specific angular momentum, h_{o} the specific angular momentum of the matter at the outer radius of the disk, D the constant in Eq. (1), and

$$y(\xi) \approx 1.43 - 1.61\xi^{2.5} + 0.18\xi^5. \quad (6)$$

Table 1. Input model parameters

Parameter	Model parameter description	Using observed values
M	Mass of the central object	
M_{o}	Mass of the optical component	+
P	Orbital period of the binary	+
$f(M_{\mathrm{o}})$	Mass function of the optical component	+
α	Turbulence parameter in the disk	
N_{HI}	Number of hydrogen atoms per cm^2 to the source	+
μ	Molecular weight of gas in the disk, 0.5	
δt	Inner parameter of the model	

Table 1 presents the input parameters for one specific non-steady-state accretion model. We took three of the parameters to be free: the mass of the compact object M, the turbulence parameter α, and the model parameter δt. A small (allowed by the observational uncertainties) variation of the mass of the optical component M_{o} around the observed value affects the disk size, which affects the rate of variation of the accretion rate in the disk.

The following values can be obtained from these parameters.

(1) The system semiaxis a, calculated from the formula

$$a = \left(\frac{G(M + M_{\mathrm{o}})P^2}{4\pi^2} \right)^{1/3} \qquad (7)$$

(assuming the orbits to be circular).

(2) The system inclination

$$i = \arcsin \left(\left[\frac{f(M_{\mathrm{o}})(1 + q)^2}{Mq^2} \right]^{1/3} \right), \qquad (8)$$

where the mass ratio is $q = M/M_{\mathrm{o}}$.

(3) The radius of the last nonintersecting orbit around the primary, which depends on the mass ratio for the binary components and, in general, does not exceed 0.6 of the Roche lobe size (values are tabulated in [21]); this is equal to the radius of the outer boundary of the disk r_{out} [21, 17].

(4) The diffusion coefficient D from (1) and (5):

$$D = 5.04 \times 10^{34} \alpha^{4/5} (\mu/0.5)^{-3/4} \qquad (9)$$
$$\times (M/M_{\odot}) B_{\mathrm{f}} [\mathrm{g}^{-3/10} \mathrm{cm}^5 \mathrm{s}^{-16/5}],$$

where $B_{\mathrm{f}} = (\Pi_1^{1/2} \Pi_2 \Pi_3^8 \Pi_4)^{-1/10}$ is a combination of dimensionless parameters specified by the vertical structure of the disk and calculated and tabulated as

a function of the opacity in [19][2]. (Thus, B_{f} depends on the opacity, which, in turn, depends on Π_1, Π_2, Π_3, and Π_4, being a function of physical parameters of the disk. We found that this combination is more dependent on the time than on the radius in the disk, but the time dependence is also not very strong, since it is a combination of parameters raised to powers much smaller than unity. In the model, we adopted the B_{f} calculated iteratively at the half-radius of the disk and at the middle of the model time interval.)

To calculate the effective temperature in the disk, we used the formula

$$T(r) = \left[-\frac{\dot{M}}{4\pi\sigma} \omega(r) r \frac{\mathrm{d}\omega(r)}{\mathrm{d}r} \left(1 - \frac{\omega(r_{\mathrm{in}})}{\omega(r)} \left(\frac{r_{\mathrm{in}}}{r} \right)^2 \right) \right.$$

$$\left. \times \sqrt{\frac{r_{\mathrm{out}}}{r}} \frac{f(\sqrt{r/r_{\mathrm{out}}})}{f'(0)} \right]^{1/4},$$

$$(10)$$

where the function $f(\xi) = 1.43\xi - 0.46\xi^{7/2} + 0.03\xi^6$, $\omega(r)$ is the angular velocity in the disk (which is Keplerian away from the compact object), σ is the Stefan–Boltzmann constant, and r_{out} is the radius of the outer boundary of the disk. The central regions of the disk [for $r \ll r_{\mathrm{out}}$, when the last two factors in (10) yield approximately unity] make the largest contribution to the X-ray emission; here, the accretion rate is nearly constant and the distribution of the effective temperature essentially coincides with that in a steady-state disk. In (10), $\dot{M}$ is equal to the value at the disk center $\dot{M}(0, t)$ from (5). We also took into account the non-Newtonian nature of the metric

---

[2]In [19], Table 1b should read Π_4 instead of Π_3; the 5th column should be ignored. In [1], there is a misprint in D in (26) and (31).

Table 2. Zero-points, central wavelengths, and effective widths for the optical bands [23]

Band	A_i^0	λ, Å	$\Delta\lambda_i$, Å
U	8.37	3650	680
B	8.198*(8.18)	4400	980
V	8.44	5500	890

*Corrected value; the value from the handbook is given in parentheses (see explanation in the text after (15)).

around the compact object in the central regions of the disk. For the Paczyński–Wiita potential (4),

$$\omega(r) = \sqrt{\frac{GM}{r}} \frac{1}{r - r_\mathrm{g}}. \quad (11)$$

We assumed that the bulk of the optical flux comes from the disk (at distances $r \gg r_\mathrm{in}$), while the radiation from the "transition layer" at the outer boundary, where the momentum is carried away, is substantially smaller.

The spectral flux density detected by an observer can be calculated using the formula [25]

$$F_\nu = \frac{L_\nu \cos i}{2\pi d^2} \exp\left(-\tau_\nu\right) \, [\mathrm{erg/(cm^2 Hz\, s)}], \quad (12)$$

where d is the distance to the system, not specified in the model, τ_ν is the optical depth corresponding to the absorption toward the system, and L_ν is the spectral luminosity of the disk according to the formula

$$L_\nu = 2\pi \int_{r_\mathrm{in}}^{r_\mathrm{out}} B(\nu, T(r)) 2\pi r \mathrm{d}r \, [\mathrm{erg/(s\, Hz)}], \quad (13)$$

where $B(\nu, T(r))$ is the Planck function.

The model curves F_i (erg/(cm^2 s)) were derived by integrating F_ν over frequency. At X-ray energies, $\tau_\nu = \sigma(\nu) N_\mathrm{HI}$, where the cross section for absorption by hydrogen atoms $\sigma(\nu)$ is presented in the form of an analytical spline [22]. The number of hydrogen atoms in the line of sight toward the source N_HI can be found in the literature, and can also be calculated using the approximating formula [23]

$$N_\mathrm{HI} \approx 4.8 \cdot 10^{21} E(B-V) \, \mathrm{atoms/cm^2}, \quad (14)$$

provided the color excess $E(B-V)$ is known and assuming that the main contribution to the absorption is made by hydrogen atoms of the interstellar medium and not those directly related to the source.

In the optical spectrum, absorption was taken into account after integrating F_ν over frequency, using the interstellar absorption $A_\lambda = 2.5\tau / \ln 10$ instead of the optical depth τ_ν (τ is some effective value for the optical band denoted by λ).

We calculated the light curves F_i in a chosen time interval $t \in [t_1, t_2]$. We took $t = 0$ to correspond to the peak of the outburst, whose epoch was set equal to the published value. The accretion rate at the inner radius, bolometric luminosity of the disk, and fluxes in specified spectral intervals (the X-ray and optical B and V bands) were calculated with a step of $\Delta t = 1$ day.

3.2. Comparison of the Model and Observed Curves

We used the light curves in one X-ray band and in the B and V bands for our modeling.

Spectral observations of X-ray novae can be used to determine in which time intervals and at which wavelengths the flux is dominated by the disk radiation, with the contributions from other components being much smaller. In general, it is obviously desirable to use data obtained at the softest X-ray energies (to $\sim$10 keV), since the typical X-ray spectrum of an X-ray nova after the outburst peak is a combination of the disk spectrum (in most cases, taken to be a blackbody, nonmonochromatic disk) and a harder power-law component [2]. For each source, we must consider the spectral evolution and exclude time intervals when either the contribution from nondisk components (or power-law components) is substantial or the disk spectrum differs appreciably from that for a blackbody, nonmonochromatic disk model. For example, taking nondisk components in the radiation into account can alter the slope of the decaying light curve, and we found that the slope of the light curve dramatically affects the resulting values for α.

We reduced observational stellar magnitudes at optical wavelengths to fluxes (erg/(cm^2 s)) using the formula

$$F_i = \Delta\lambda_i 10^{-0.4 m_i - A_i^0}, \quad (15)$$

where the zero-points A_i^0 and effective bandwidths $\Delta\lambda_i$ are presented in Table 2. We corrected the A_B^0 values in accordance with [24], where the disk color indices were calculated using the known radial temperature distribution, taking into account the actual transmission functions for the optical filters used. The resulting values calculated with our code, using rectangular pass bands for the optical filters, coincided with those from [24] to within 0.01^m. To achieve this agreement, it was necessary to correct the zero-point in the B band.

Let us suppose that the observed accretion-disk flux in some X-ray spectral interval, $F_\mathrm{x}^\mathrm{obs}$, is known at some time $t \in [t_1, t_2]$. It is then possible to derive the distance d to the source for the chosen model parameters by comparing this value with $F_i(t)$, taking into account the absorption toward the source and the
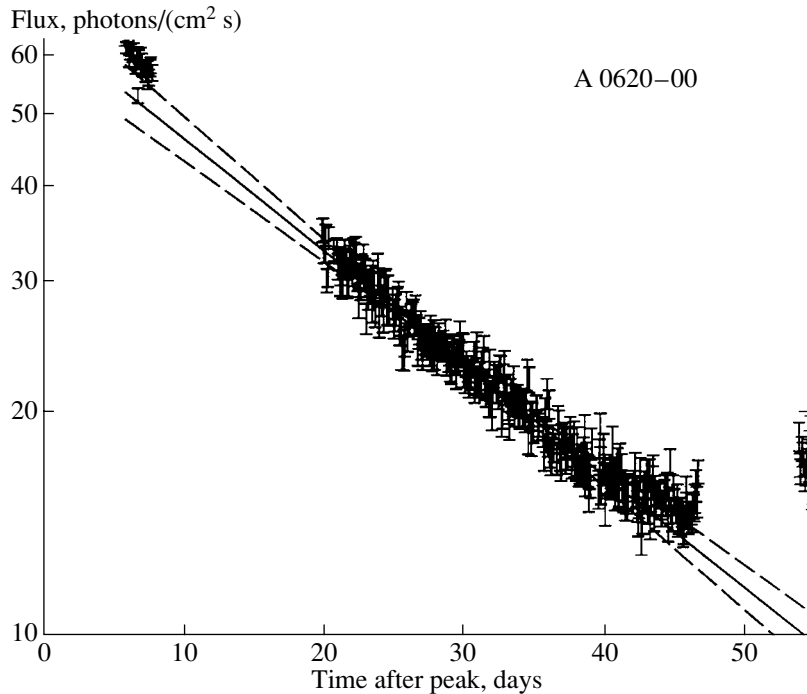
Fig. 1. Straight-line approximation of the X-ray light curve for A 0620−00. The regression line for the data in the interval $t \in [20, 40]$ days (solid line) and selection boundaries for the theoretical curves (two dashed lines) are plotted. The observational data are from [29].

inclination i calculated with (8). We assumed that the disk is coplanar to the binary orbit.

We calculated model curves F_i using the derived d. We calculated the color excess $E(B - V)^{\text{model}}$ for the curves at optical wavelengths required to obtain agreement with the observed optical flux in the B band. Each optical curve was corrected for this $E(B - V)^{\text{model}}$. We used the values $R_B = 4.2$, $R_V = 3.2$, $R_U = 5$ [23] in the formula relating the color excess and interstellar absorption:

$$A_\lambda = R_\lambda E(B - V). \qquad (16)$$

The models were selected to provide agreement between the X-ray and optical fluxes and slopes of the observed and theoretical light curves. The observations indicate that the X-ray light curves are very close to exponential and can be described using only a few parameters. This made it possible to appreciably reduce the time required for the fitting compared to a simple exhaustive search for the parameters minimizing χ^2. We approximated the observed light curves with straight lines $\log F_i = a_\text{r} t + b_\text{r}$, whose slopes a_r are compared to that of the theoretical curve at some point $t \in [t_1, t_2]$ in the middle of the model time interval. We compared the fluxes in the three spectral intervals for this t, taking into account the observed color excess $E(B - V)$ and the color of the disk $B-$

V. The value of χ^2 was calculated for the selected models.

The error of the observed disk color $B-V$ can reach 0.05 magnitudes. Such a large scatter is due to both observational errors and possible fluctuations of the disk color (due to precession, the superposition of the optical flux from the secondary, etc), which we do not consider here in detail. We also did not take into consideration the contribution of radiation from the central X-ray source reradiated from the outer parts of the disk.

For some of the light curves, the overall traces are rather close to exponential but they are not in good agreement with the observations according to a χ^2 criterion (at the 0.05 significance level), possibly due to underestimation of the observational errors and/or the superposition of fluctuations on the main curve.

4. MODELING THE X-RAY NOVA A 0620−00 IN THE 3−6 keV X-RAY AND B AND V OPTICAL BANDS

4.1. Observations

4.1.1. X-ray Light Curves

The nova outburst in Monoceros in 1975 (A 0620−00, V 616 Mon) was observed in X-rays with the orbiting observatories Ariel-5, SAS 3, Salut 4, and

LIPUNOVA, SHAKURA

Table 3. Input parameters for A 0620−00* models

Parameter	Tested values
M	$5-25 M_{\odot}$
M_{o}	$0.3, 0.5, 0.7 M_{\odot}$
P	0.322 day
$f(M_{\mathrm{o}})$	$2.7 M_{\odot}$
α	$0.1-1$
N_{HI}	$3 \times 10^{21} - 10^{22}$ atoms/cm²
μ	0.5
δt	$50-250$

* The mass of the optical component $M_{\mathrm{o}} = 0.5 M_{\odot}$, its mass function, and the binary period were taken from [3, 4].

Vela 5B [26−30]. A 0620−00 was the first X-ray transient identified with an optical burst [31, 32].

We used the 3−6 keV data of [29], obtained with the Ariel-5 All Sky Monitor. Following [4], we assumed that the peak of the outburst was on Aug 13, 1975, or JD 2442638.3. The corresponding data in Crab flux units were taken in electronic form from the HEASARC (High Energy Astrophysics Science Archival Research Center) database [4][3].

We fit the X-ray light curve in units of photons/cm² s. Figure 1 presents the model selected according to the slope of the 3−6 keV X-ray light curve. The regression line constructed using observations in the interval $t \in [20, 40]$ days has $a_{\mathrm{r}} = -0.01502 \pm 0.0002$ and $b_{\mathrm{r}} = 1.816 \pm 0.007$. The data at $t \approx 10$ days cannot be ascribed with confidence to the exponential section of the light curve specified by the disk radiation. The dashed curves indicate the boundaries within which we found acceptable models. Within these boundaries, the slopes of the lines tangent to the light curve at the point $t = 30$ days vary in the range $(0.9 - 1.1)a_{\mathrm{r}}$. χ^2 divided by the number of degrees of freedom does not exceed 1.3 in this interval.

4.1.2. The X-ray Spectrum at the Time of the Outburst

As has often been noted, X-ray novae in general and A 0620−00 in particular (see, for example, [33]) display a softening of the spectrum during the initial decay in the light curve. For A 0620−00, this was also pointed out, for example, in [34] (3.0−7.6 keV observations) and [35] (3−9 keV observations).

---

[3]ftp://legacy.gsfc.nasa.gov/FTP/heasarc/dbase/misc_files/xray_nova/.

Spectral data with high resolution (10 eV at 2 keV and 285 eV at 6.7 keV) obtained with the Columbia spectrometer OSO 8 on board the Ariel-5 spacecraft in October 1975 were analyzed in [36]. The X-ray continuum of A 0620−00 on September 17−18, 1975 (the 34th−35th day after the peak) was best fit by a blackbody model with $kT \sim 0.5$ keV.

Note that, at the energies of interest to us (>1 keV), the spectrum of a nonmonochromatic, blackbody disk can be approximated by a Wien spectrum:

$$I_E = \frac{2}{c^2 h^3} E^3 \exp\left(-E/k T_{\max}\right), \qquad (17)$$

where $T_{\max}$ is the maximum temperature in the disk, which occurs at the radius $\approx 1.58 r_{\mathrm{in}}$ in the case of the Paczyński−Wiita gravitational potential (4). In a Newtonian potential approximation, the radius for the maximum temperature is approximately $1.36 r_{\mathrm{in}}$.

4.1.3. Number of Hydrogen Atoms/cm² toward A 0620−00 and the Color Excess

The number of hydrogen atoms were estimated from the falloff in the soft X-ray spectrum due to the absorption of X-rays with energies <1 keV [27, 28, 34]. The values obtained are from 3×10^{21} to 10^{22} atoms/cm².

In [37], the estimate $E(B - V) = 0.35$ was derived using UV observations obtained with the ANS satellite, based on the 2200 Å peak in the interstellar absorption curve. Twenty-five stars near A 0620−00 were studied, and the specific absorption curve for the region was derived. Using (14), we find $N_{\mathrm{HI}} \sim 1.7 \times 10^{21}$ atoms/cm². The total number of hydrogen atoms in the Galaxy in the line of sight toward A 0620−00 from [38] is $\sim 4 \times 10^{21}$ atoms/cm².

Obviously, we cannot exclude the possibility of substantial and variable absorption of the X-ray radiation in the source itself. However, the character and origin of this variability are unknown. We modeled the observations for Nova Monocerotis for a set of N_{HI} values in the range $10^{21} - 10^{22}$ atoms/cm². We took the color excess to be 0.35 [37], with an uncertainty of ± 0.01.

4.1.4. Optical Light Curves

We used the optical observations from [39−44]. We constructed linear regression fits $\log F = a_{\mathrm{r}} t + b_{\mathrm{r}}$ to the B and V optical data in logarithmic flux units for times $t \in [0, 47]$ days using a weighted least-squares method. This yielded $a_{\mathrm{r}} = -0.0079 \pm 0.0002$, $b_{\mathrm{r}} = -9.675 \pm 0.005$ for the B band and $a_{\mathrm{r}} = -0.0071 \pm 0.0002$, $b_{\mathrm{r}} = -9.885 \pm 0.006$ for the
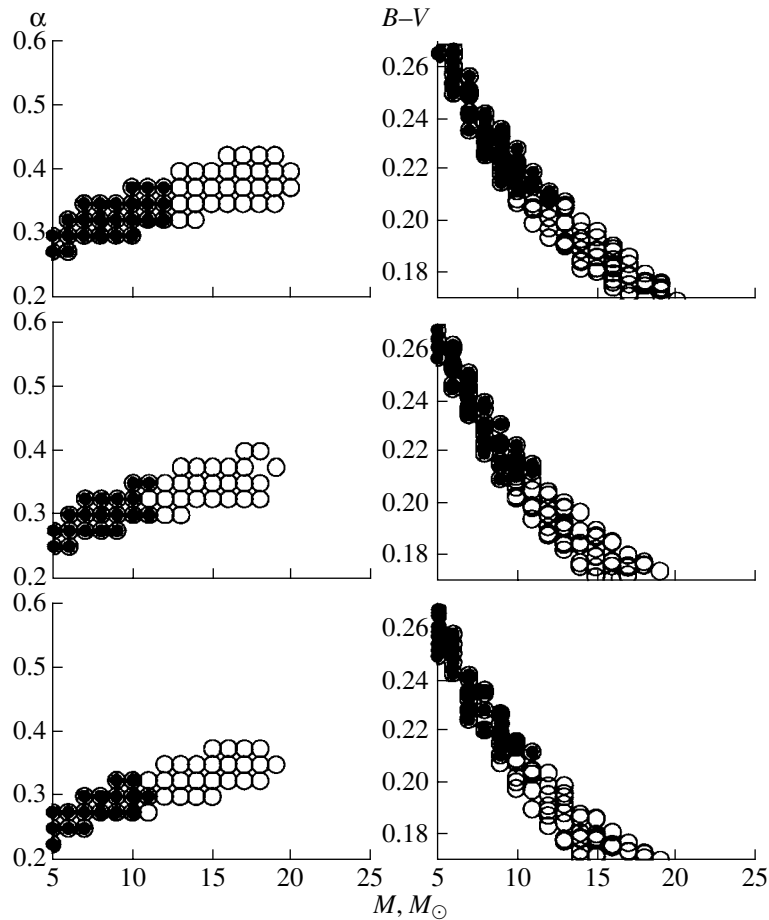
Fig. 2. Modeled α and color of the A 0620−00 disk in the 3−6 keV, B, and V bands. Results are given for the values from Table 3. The mass of the optical component varies from top to bottom: 0.3, 0.5, and $0.7M_\odot$. The filled circles satisfy the disk color condition $B{-}V = 0.24 \pm 0.03$ for $t = 30$ days.

V band (see Section 3.2). The reduced χ^2 values for these fits are roughly 12 and 43 for the B and V bands, with 102 and 89 degrees of freedom, respectively. This suggests that the adopted errors for the optical observations might be underestimated (for example, systematic deviations have not been taken into account) and/or that our assumed exponential (quasi-exponential) decrease of the optical flux does not yield a complete description of the observed curves, due to various fluctuations and variations of the optical flux superimposed on the overall trace of the light curve. Nevertheless, we assumed that the basic traces of the light curves can be fit by a quasi-exponential decay.

In the model fitting, we used the color of the disk at $t = 30$ days $B{-}V = 0.24 \pm 0.03^m$, derived from the observational data.

4.2. Results of the Modeling

We compared the theoretical and observed curves $t \in [20, 40]$ days after the outburst peak. Table 3

summarizes the parameters for which we searched for models for A 0620−00. The number of hydrogen atoms along the line of sight toward A 0620−00 does not appreciably affect the results, since the absorption at 3−6 keV is small.

Figure 2 presents the results of our modeling for the parameters from Table 3. We can see that α lies in the range 0.225−0.375 (for slightly different masses M_o). In [46], we adopted $M_o = 0.5M_\odot$ and $E(B - V) = 0.39$ and used a broader range of slopes than in Fig. 1, so a broader interval for α was obtained for A 0620−00 in that study from 0.3 to 0.5.

Figure 3 presents the resulting relationship between the distance to A 0620−00 and the mass of the black hole. The distance to A 0620−00 has been estimated to be from 0.5 to 1.2 kpc (for example, in [41, 45]; see also the reviews [3, 4]). Figure 3 indicates that, for $d \sim 0.9$ kpc [45], the mass of the black hole in A 0620−00 is $\sim 9M_\odot$. This mass for the compact object is consistent with previous estimates made in other studies (see [3] and references therein).
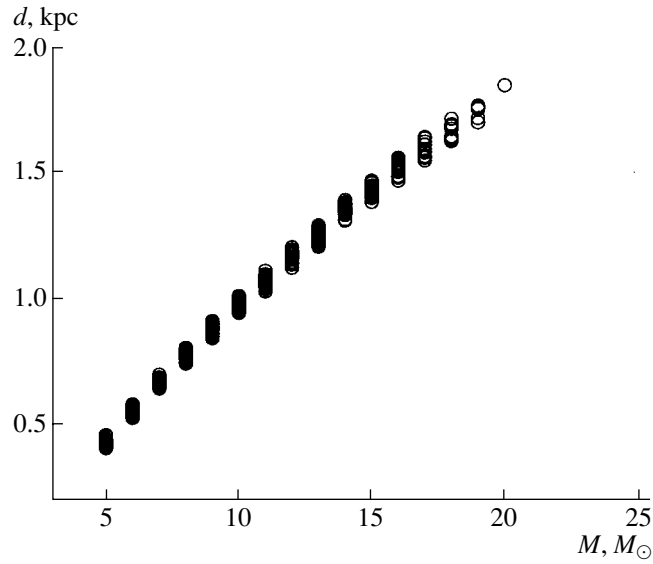
Fig. 3. The distance–black hole mass dependence for A 0620−00 for the model parameters from Table 3.
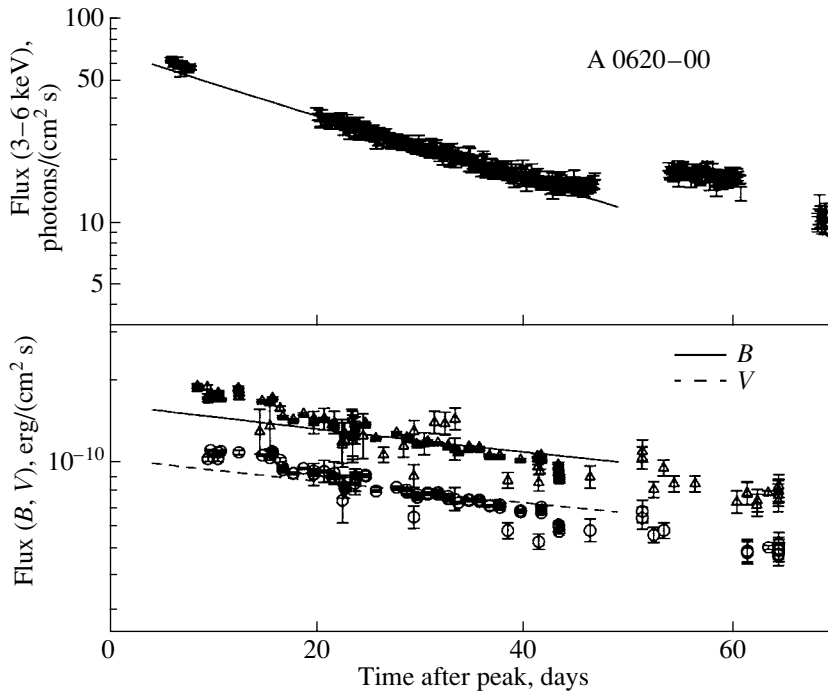

Fig. 4. Example of model light curves for A 0620−00 in the 3−6 keV, B, and V bands. The model parameters are $M = 7M_\odot$, $M_o = 0.5M_\odot$, $\alpha = 0.3$, $\delta t = 168$ days, and $N_{HI} = 3 \times 10^{21}$ atoms/cm^2.

Figure 4 presents one of the model light curves, for which $i = 47°$, $d = 0.66$ kpc, the bolometric luminosity $L_{bol}(t = 0) = 0.25L_{Edd}$, and $T_{max}(t = 35) = 0.45$ keV (cf. Section 4.1.2). The reduced χ^2 for the X-ray light curve for $t \in [20, 40]$ days is 1.17.

We were not able to obtain a satisfactory fit to the slope of the optical light curves, and further studies of the generation of optical radiation in a non-steady-state disk are necessary. In principle, steeper optical light curves can be obtained by taking into account reradiation from a thick or twisted disk. The outer parts of the disk intercept some of the X-ray flux from the central regions, causing the effective temperature of the outer disk, and accordingly its radiated flux, to increase. The intrinsic and reradiated flux depend on the accretion rate in different ways: the reradiated
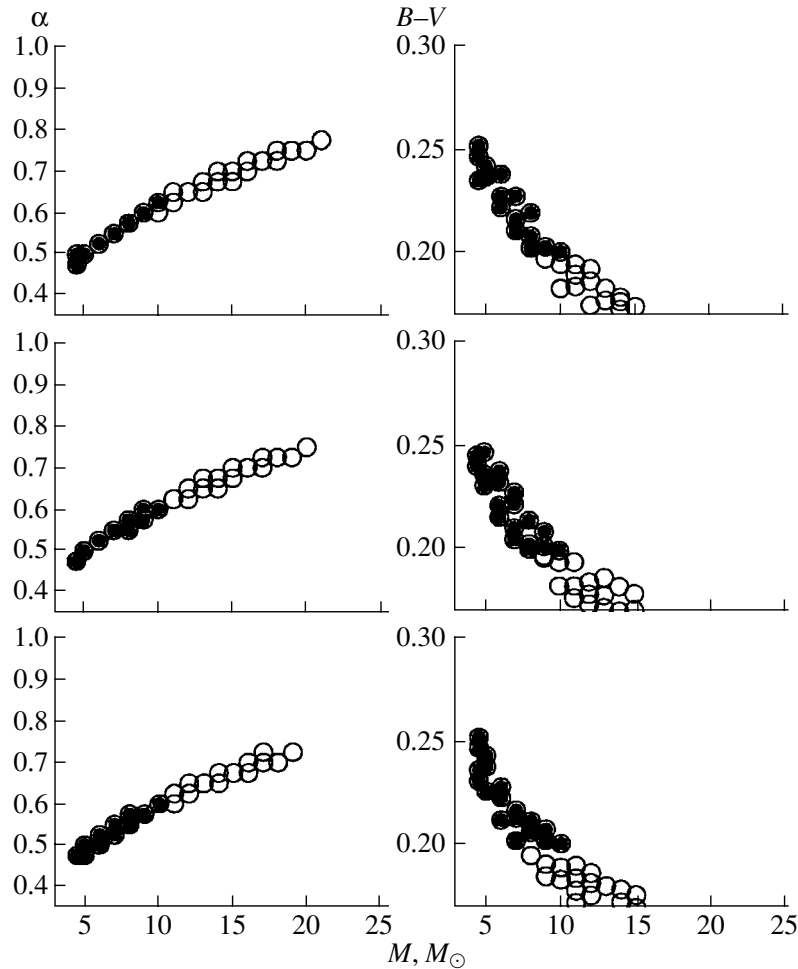
Fig. 5. Modeled α and color of the disk of GS 1124−683 in the 1.2−7.2 keV, B, and V bands for the parameters in Table 4. The mass of the optical component and the number of hydrogen atoms along the line of sight toward GS 1124−683 vary from top to bottom: $M_o = 0.8M_\odot$, $N_{HI} = 1.4 \times 10^{21}$ atoms/cm² (two upper graphs), $M_o = 0.9M_\odot$, $N_{HI} = 1.4 \times 10^{21}$ atoms/cm² (two middle graphs), and $M_o = 0.8M_\odot$, $N_{HI} = 2.5 \times 10^{21}$ atoms/cm² (two lower graphs). The filled circles satisfy the disk color condition $B-V = 0.27 \pm 0.07^m$ for $t = 48$ days.

optical flux decreases more rapidly, steepening the optical light curves. The outburst of A 0620−00 was modeled taking into account reradiation by the disk in [61], assuming a relative half-thickness for the disk of 0.12 (which is strongly overestimated compared to the standard model). In the standard α-disk model, reradiation is insignificant due to the small half-thickness of the disk, which is typically about 0.03 [1]. It is probable that we must take into account the contribution to the optical flux of reradiation by the disk, which is likely to be warped.

5. MODELING THE X-RAY NOVA GS 1124−683 IN THE 1.2−37.2 keV X-RAY AND B AND V OPTICAL BANDS

5.1. Observations

5.1.1. X-ray Light Curves

The outburst of Nova Muscae (GS 1124−683, GU Mus) was discovered independently by WATCH/GRANAT and ASM/GINGA (All-Sky X-Ray Monitor) on January 9, 1991 [47−49]. The associated optical outburst was also detected [50]. For the modeling, we used 1.2−37.2 keV data obtained with the GINGA Large Area Counters [51]. The data in erg/(cm² s) were taken from the HEASARC database [4; see Footnote 3]. As is done in [4], we took the peak of the outburst to be on January 15, 1991, or JD 2448272.7862. The X-ray modeling was carried out in erg/(cm² s).
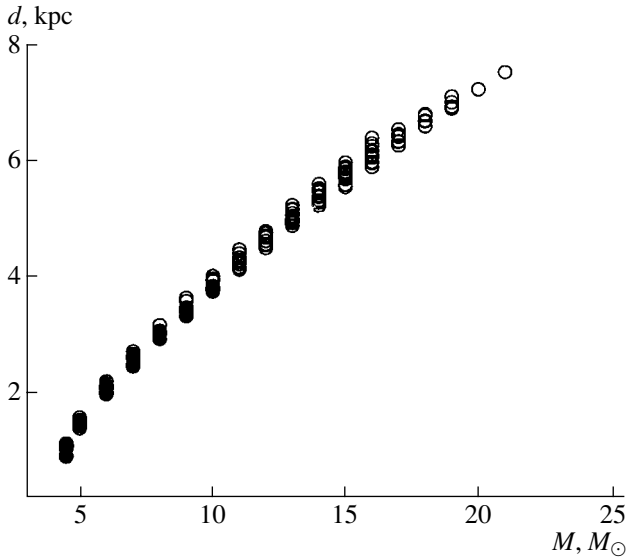
d, kpc

Fig. 6. The distance–black-hole mass relation for GS 1124–683, modeled for the parameters from Table 4.

The weighted least-squares regression line for data in the interval $t \in [35, 61]$ days yields $a_r = -0.0134 \pm 0.0001$ and $b_r = -6.511 \pm 0.005$. However, the calculated reduced χ^2 is very high, since the observational errors are small and the data show an appreciable scatter around the overall trace of the model light curve. To fit the models, we varied the slopes for lines tangent to the theoretical light curves at $t = 48$ days within the limits $(0.98 - 1.02)a_r$.

Table 4. Input parameters for GS 1124-683 models*

Parameter	Tested values
M	$5-25 M_\odot$
M_o	$0.8, 0.9 M_\odot$
P	0.433 days
$f(M_o)$	$3 M_\odot$
α	$0.1-1$
N_{HI}	$(1.4-2.5) \times 10^{21}$ atoms/cm²
μ	0.5
δt	$50-250$

* The mass of the optical component $M_o = 0.8 M_\odot$ is adopted in accordance with [4], and the binary period and mass function of the optical component $3.01 \pm 0.15 M_\odot$ are derived in [60].

5.1.2. The X-ray Spectrum at the Time of the Outburst

It follows from [51] that, after the peak, the spectrum of GS 1124−683 softened as the luminosity decreased. In [51−54], the observed X-ray spectrum was approximated by a model consisting of two components: a blackbody, nonmonochromatic disk and a harder power-law component. Figure 15 in [51] indicates that, in the time interval of interest, T_{in} for the spectral approximation [51] is roughly 0.7 keV. In a model with a Shakura−Syunaev disk, the effective temperature at the radius R_{max} is about 40% lower than T_{in} and is consistent with that obtained in our model (see p. 52).

It was suggested in [52] that 59% of the flux on January 15 (near the outburst peak) was blackbody disk radiation, while the remainder was contributed by a power-law component. During the following $25-30$ days, the power-law component decayed more rapidly than the disk component. ROSAT observations on January 25 (the 10th day after the peak) [54] suggested that the 0.3−20 keV flux at that epoch was contributed completely by the disk component. Using the approximation for the observed 1.2−37.2 keV X-ray spectrum from [53] and the derived fluxes of the spectral components, we conclude that the 1.2−37.2 keV flux $t \in [35, 61]$ days after the outburst was determined wholly by the disk radiation and can therefore be used in our modeling, since the contribution from nondisk components is apparently negligible.

5.1.3. Number of Hydrogen Atoms/cm² toward GS 1124−683 and the Color Excess

In [55], $E(B - V) \sim 0.29$ was estimated from HST observations of the interstellar absorption profile at 2200 Å. $E(B - V) = 0.3 \pm 0.05$ was found using a similar technique in [56]. In [57], the same value $E(B - V) = 0.30 \pm 0.10$ was acquired from interstellar Na D lines. Using (14), we can derive $N_{HI} \approx 1.4 \times 10^{21}$ atoms/cm² from this color excess.

Greiner *et al.* [54] obtained $N_{HI} \approx 2.2 \times 10^{21}$ atoms/cm² by modeling the combined ROSAT 0.3−4.2 keV and GINGA 1.2−37.2 keV data for January 24−25 using a composite spectrum with a blackbody, nonmonochromatic disk and a power-law component. For various nonmonochromatic disk models, they obtained values from 1.7×10^{21} to 2.5×10^{21} atoms/cm².
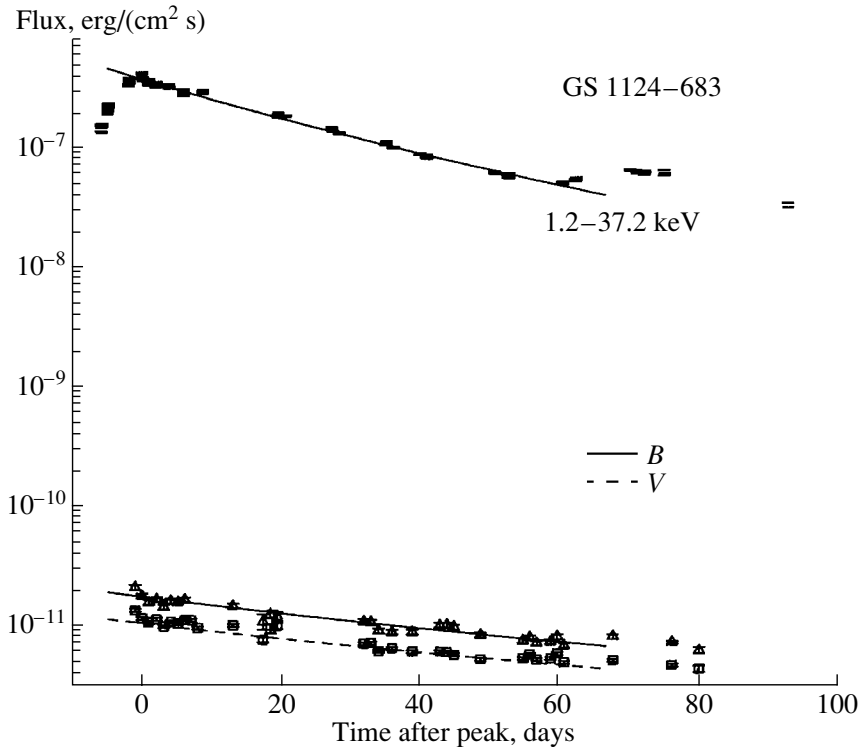
Fig. 7. Example of model light curves of GS 1124−683H in the 1.2−37.2 keV, B, and V bands. The model parameters were $M = 7M_\odot$, $M_o = 0.8M_\odot$, $\alpha = 0.55$, $\delta t = 103$ days, and $N_{\mathrm{HI}} = 1.4 \cdot 10^{21}$ atoms/cm^2.

5.1.4. Optical Light Curves

We used the observational data from [58, 59] and derived weighted least-squares regression lines for the optical B and V observations in the logarithmic flux units in the time interval $t \in [12, 61]$ days. This yielded $a_r = -0.0057 \pm 0.0006$, $b_r = -10.79 \pm 0.03$ for the B band, and $a_r = -0.0052 \pm 0.0006$, $b_r = -10.98 \pm 0.03$ for the V band. The corresponding reduced χ^2 values are 2.8 and 7.3 for B and V, respectively, with 17 degrees of freedom. This leads us to conclusions similar to those deduced from the A 0620−00 optical light curves (see Section 4.1.3). We again assumed that the overall trace of the light curves represents a quasi-exponential decay.

In the model fitting, we used the observed color of the disk for $t = 48$ days: $B - V = 0.27 \pm 0.07^m$.

5.2. Results of the Modeling

We compared the theoretical and observed curves $t \in [35, 61]$ days after the peak of the outburst. Table 4 summarizes the GS 1124−683 model parameters.

Figure 5 presents the results of our modeling for the parameters from Table 4. Comparing the lower and upper left graphs, we can see a slight dependence of the model results on the number of hydrogen atoms toward GS 1124−683. The resulting α values for the

GS 1124−683 disk lie in the range 0.475−0.625 (for small variations in M_o and N_{HI}).

Figure 6 displays the dependence of the distance to GS 1124−683 on the black-hole mass. Estimates of the distance to GS 1124−683 in the literature range from 1 to 8 kpc. For 3 kpc [3], the implied mass of the black hole in GS 1124−683 is $\sim 8M_\odot$ (Fig. 6). The probable values for the black-hole mass we have derived are consistent with the observations (see [3] and references therein). Figure 7 presents model light curves for some parameters from the obtained ranges of values. In the corresponding model, we obtained $i = 68°$, $d = 2.6$ kpc, the bolometric luminosity $L_{\mathrm{bol}}(t = 0) = 0.47L_{\mathrm{Edd}}$, and $T_{\mathrm{max}}(t = 48) = 0.44$ keV. The model satisfactorily reproduces both the X-ray and optical-light curves of GS 1124−683.

6. CONCLUSION

We have modeled outbursts of two X-ray novae— A 0620−00 and GS 1124−683—using the model for a non-steady-state α disk in a binary system considered in [1].

The turbulence parameter α was estimated to be 0.2−0.4 for A 0620−00 and 0.45−0.65 for GS 1124−683. The similarity in these α values suggests that the accretion-disk viscosities for such compact objects may have the same nature, at least in these

two sources. The value of α ($\lesssim 1$) indicates that the gas in the disks is appreciably turbulent. We have also obtained relations between the distances to the systems and the masses of the compact objects they contain.

Thus, we have described for the first time the exponentially decaying light curves of X-ray novae using a model with a thin accretion disk with constant α, simultaneously estimating the implied values of α itself.

Note that the optical B and V fluxes from GS 1124−683 can be explained as disk radiation that is generated locally in the course of heat release due to viscosity. It is likely that, in the case of A 0620−00, we must also take into account the contribution to the optical flux from reradiation by a warped disk. We will consider this problem in a subsequent paper.

7. ACKNOWLEDGEMENTS

REFERENCES

1. G. V. Lipunova and N. I. Shakura, Astron. Astrophys. **356**, 363 (2000).
2. Y. Tanaka and N. Shibazaki, Ann. Rev. Astron. Astrophys. **34**, 607 (1996).
3. A. M. Cherepashchuk, Space Sci. Rev. **93**, 473 (2000).
4. W. Chen, C. R. Shrader, and M. Livio, Astrophys. J. **491**, 312 (1997).
5. E. P. Velikhov, Zh. Éksp. Teor. Fiz. **36**, 1398 (1959) [Sov. Phys. JETP **9**, 995 (1959)].
6. S. Chandrasekhar, *Hydrodynamic and Hydromagnetic Stability* (Clarendon, Oxford, 1961), p. 384.
7. S. A. Balbus and J. F. Hawley, Astrophys. J. **376**, 214 (1991).
8. P. J. Armitage, Astrophys. J. Lett. **501**, L189 (1998).
9. J. F. Hawley, Astrophys. J. **528**, 462 (2000).
10. N. I. Shakura, Astron. Zh. **49**, 921 (1972) [Sov. Astron. **16**, 756 (1972)].
11. J. K. Cannizzo, A. W. Shafer, and J. C. Wheeler, Astrophys. J. **333**, 227 (1988).
12. A. Siemiginowska and B. Czerny, Mon. Not. R. Astron. Soc. **239**, 289 (1989).
13. R. Narayan, I. Yi, and R. Mahadevan, Nature **374**, 623 (1995).
14. R. Narayan, J. E. McClintock, and I. Yi, Astrophys. J. **457**, 821 (1996).
15. L. G. Filipov, Adv. Space Res. **3**, 305 (1984).
16. Yu. E. Lyubarskiĭ and N. I. Shakura, Pis'ma Astron. Zh. **13**, 917 (1987) [Sov. Astron. Lett. **13**, 386 (1987)].
17. S. Ichikawa and Y. Osaki, Publ. Astron. Soc. Jpn. **46**, 621 (1994).
18. N. I. Shakura and R. A. Sunyaev, Astron. Astrophys. **24**, 337 (1973).
19. N. A. Ketsaris and N. I. Shakura, Astron. Astrophys. Trans. **15**, 193 (1998).
20. B. Paczyński and P. J. Wiita, Astron. Astrophys. **88**, 23 (1980).
21. B. Paczyński, Astrophys. J. **216**, 822 (1977).
22. R. Morrison and D. McCammon, Astrophys. J. **270**, 119 (1983).
23. M. V. Zombeck, *Handbook of Astronomy and Astrophysics* (Cambridge Univ. Press, Cambridge, 1990), p. 100.
24. N. G. Bochkarev, E. A. Karitskaya, N. I. Shakura, and S. A. Zhekov, Astron. Astrophys. Trans. **1**, 41 (1991).
25. N. G. Bochkarev, R. A. Syunyaev, T. S. Khruzina, *et al.*, Astron. Zh. **65**, 778 (1988) [Sov. Astron. **32**, 405 (1988)].
26. M. Elvis, C. G. Page, K. A. Pounds, *et al.*, Nature **257**, 656 (1975).
27. R. Doxsey, G. Jernigan, D. Hearn, *et al.*, Astrophys. J. Lett. **203**, L9 (1976).
28. V. G. Kurt, E. I. Moskalenko, L. G. Titarchuk, and E. K. Sheffer, Pis'ma Astron. Zh. **2**, 107 (1976) [Sov. Astron. Lett. **2**, 42 (1976)].
29. L. J. Kaluzienski, S. S. Holt, E. A. Boldt, and P. J. Serlemitsos, Astrophys. J. **212**, 203 (1977).
30. H. Tsunemi, S. Kitamoto, S. Okamura, and D. Roussel-Dupré, Astrophys. J. Lett. **337**, L81 (1989).
31. F. Boley and R. Wolfson, IAU Circ., No. 2819 (1975).
32. F. Boley, R. Wolfson, H. Bradt, *et al.*, Astrophys. J. Lett. **203**, L13 (1976).
33. E. Kuulkers, New Astron. Rev. **42**, 1 (1999).
34. G. F. Carpenter, C. J. Eyles, G. K. Skinner, *et al.*, Mon. Not. R. Astron. Soc. **176**, 397 (1976).
35. O. Citterio, G. Conti, P. Di Benedetto, *et al.*, Mon. Not. R. Astron. Soc. **175**, 35 (1976).
36. K. S. Long and H. L. Kestenbaum, Astrophys. J. **226**, 271 (1978).
37. C.-C. Wu, R. J. Panek, A. V. Holm, and M. Schmitz, Publ. Astron. Soc. Pac. **95**, 391 (1983).
38. H. Weaver and D. R. W. Williams, Astron. Astrophys., Suppl. Ser. **8**, 1 (1973).
39. V. M. Lyutyĭ, Pis'ma Astron. Zh. **2**, 112 (1976) [Sov. Astron. Lett. **2**, 43 (1976)].
40. S. Yu. Shugarov, Perem. Zvezdy **20**, 251 (1976).
41. S. van den Bergh, Astron. J. **81**, 104 (1976).
42. H. W. Duerbeck and K. Walter, Astron. Astrophys. **48**, 141 (1976).
43. B. C. S. Robertson, P. R. Warren, and R. A. Bywater, Inf. Bull. Var. Stars, No. 1173, 1 (1976).
44. C. Lloyd, R. Noble, and M. V. Penston, Mon. Not. R. Astron. Soc. **179**, 675 (1977).
45. J. B. Oke, Astrophys. J. **217**, 181 (1977).

46. G. V. Lipunova and N. I. Shakura, Astrophys. Space Sci. Rev. **276**, 231 (2001).
47. N. Lund and S. Brandt, IAU Circ., No. 5161 (1991).
48. R. A. Sunyaev, IAU Circ., No. 5179 (1991).
49. F. Makino *et al.*, IAU Circ., No. 5161 (1991).
50. R. M. West, M. Della Valle, and B. Jarvis, IAU Circ., No. 5165 (1991).
51. K. Ebisawa, M. Ogawa, T. Aoki, *et al.*, Publ. Astron. Soc. Jpn. **46**, 375 (1994).
52. S. Kitamoto, H. Tsunemi, S. Miyamoto, and K. Hayashida, Astrophys. J. **394**, 609 (1992).
53. S. Miyamoto, S. Iga, S. Kitamoto, and Y. Kamado, Astrophys. J. Lett. **403**, L39 (1993).
54. J. Greiner, G. Hasinger, S. Molendi, and K. Ebisawa, Astron. Astrophys. **285**, 509 (1994).
55. F. H. Cheng, K. Horne, N. Panagia, *et al.*, Astrophys. J. **397**, 664 (1992).
56. C. R. Shrader and R. Gonsalez-Riestra, Astron. Astrophys. **276**, 373 (1993).
57. M. Della Valle, B. J. Jarvis, and R. M. West, Nature **353**, 50 (1991).
58. N. L. King, T. E. Harrison, and B. J. McNamara, Astron. J. **111**, 1675 (1996).
59. M. Della Valle, N. Masetti, and A. Bianchini, Astron. Astrophys. **329**, 606 (1998).
60. J. A. Orocz and C. D. Bailyn, Astrophys. J. **468**, 380 (1996).
61. A. A. Esin, E. Kuulkers, J. E. McClintock, and R. Narayan, Astrophys. J. **532**, 1069 (2000).

Translated by K. Maslennikov

Disk Wind in Young Binaries and its Impact on the Infrared Excesses of Young Stars

V. P. Grinin[1,2]

[1] *Pulkovo Observatory, Russian Academy of Sciences, Pulkovskoe shosse 65, St. Petersburg, 196140 Russia*
[2] *Crimean Astrophysical Observatory, National Academy of Sciences of Ukraine,*
p/o Nauchnyĭ, Crimea, 334413 Ukraine
Received September 14, 2001; in final form October 19, 2001

Abstract—We consider the effect of binarity of young stars on the spectral energy distribution of the IR radiation from circumstellar dust. The formation of a common dust envelope in a binary system with a low-mass secondary component is strongly affected by the disk wind from the secondary. The small velocities in peripheral areas of the wind are such that it can be partially or entirely captured by the primary, even when the distance between the components is up to several astronomical units. As a result, an envelope with a rather complex spatial and kinematic structure is formed. Its mass is many orders of magnitude smaller than that of the accretion disk around the binary. However, the thermal radiation emitted by dust particles of the envelope can be comparable to the total radiation of the accretion disk. This result is discussed in the context of the deficit at near-IR wavelengths ($2 - 10\mu$m) in current models for accretion disks around young stars. © *2002 MAIK "Nauka/Interperiodica".*

1. INTRODUCTION

The infrared excesses displayed by many young stars, associated with thermal radiation by circumstellar dust, provide basic information about the structure of their circumstellar gas—dust disks [1–4], and can also indicate the young age of the stars themselves [5]. Current theory connects this formation with absorption and subsequent reemission of the stellar radiation by circumstellar dust particles in accretion (protoplanetary) disks [6, 7]. When observed and theoretical infrared spectral energy distributions (SEDs) are compared, it is apparent that classical models of flat accretion disks are only partially consistent with the observations. The fact that the IR excesses predicted by the models are often smaller than those observed has been discussed for a long time [8–18]. The general aim of these studies is to find a way to increase the effective opening angle of the accretion disk, in order to increase the fraction of the stellar radiation absorbed by circumstellar dust.

Kenyon and Hartmann [8] made a first step in this direction by replacing the flat model accretion disk with a so-called flaring disk. In this model, the ratio between the geometrical thickness of the disk h and the current distance to the center r is a slowly increasing function of r. Peripheral layers of such a disk are able to intercept a larger fraction of the stellar radiation, making it possible to remove disagreements between the observed and theoretical SEDs of

young stars at far-IR wavelengths. However, the discrepancy between observations and theory remains at near-IR wavelengths ($2 - 10\mu$m).

Chiang and Goldreich [10] added a hot atmosphere to the flaring-disk model. Natta *et al.* [11] suggested that the additional IR radiation originates in the immediate vicinity of the star, due to an increase in the geometrical thickness of the accretion disk in a zone of intense dust sublimation. In addition, more radical attempts to solve the problem have been made by supplementing the accretion disk with a dust envelope [9, 14, 15], or even by replacing the accretion disk with a spherically symmetrical distribution of circumstellar matter [16–18].

All these studies have assumed that the young star is single. However, it follows from observations (see reviews [19], [20], and references therein) that a substantial fraction of young stars (more than 50% in some young clusters) are binary or multiple. As we noted in [21] (Paper I), under certain conditions this can appreciably affect the distribution of matter in the central area of a binary system. Here, we consider the infrared SEDs in such binaries based on the results obtained in Paper I.

2. TWO-STEP ACCRETION IN YOUNG BINARIES

Calculations made by Artimowicz and Lubow [22] indicate that complex hydrodynamical processes occur in a young binary surrounded by the remnants of

the protostellar cloud, due to the orbital rotation of the components. Periodic gravitational perturbations result in the formation of a cavity free of matter in the central area of the binary, which is periodically penetrated by streams of matter from the periphery of the system. These streams maintain the accretion onto the system components. In binaries with un-equal component masses, most of the matter from the remnants of the protostellar cloud, which we will call a circumbinary (CB) disk, is accreted onto the low-mass component (see also [23]). This asymmetry is due to the proximity of the low-mass component to the CB disk. As a result, for a component-mass ratio of $M_2/M_1 \approx 0.1-0.2$, the rate of accretion onto the low-mass component can exceed that onto the primary by a factor of ten or more (see Fig. 6 in [23]).

In this case, as was shown in Paper I, a two-step accretion mechanism becomes efficient when matter from the CB disk first accretes onto the low-mass component then is transfered to the central area of the binary. This type of accretion is possible due to the outflow from the disk under the action of turbu-lent and magnetic viscosity [24, 25]. The outflowing matter, called a disk wind, carries excess angular momentum out of the accretion disk, resulting in a radial motion of matter in the disk toward the center.

Thus, accreting matter from the CB disk, the sec-ondary loses some matter in the form of the disk wind. This forms a common envelope with a rather complex spatial and kinematic structure, which can be par-tially or totally captured by the primary (see Paper I). Dust particles located in this envelope can provide a powerful source of IR radiation, with luminosity comparable to that of the entire CB disk.

The efficiency of the two-step accretion mecha-nism is specified by two parameters. One of them

$$f = \dot{M}_w/\dot{M}_2, \qquad (1)$$

is the ratio of the rate of mass loss in the form of the disk wind $\dot{M}_w$ and the rate of accretion onto the low-mass component $\dot{M}_2$. This parameter specifies the fraction of matter from the CB disk accreted onto the secondary, which the secondary brings back into the binary in the form of the disk wind. The theoretical upper limit for this ratio, $f = 1$, corresponds to the case when most of the accreted matter does not reach the secondary and is scattered in the surrounding space in the form of the disk wind. This occurs when the specific angular momentum of the matter at the edges of the accretion disk substantially exceeds that at its inner boundary [24]. Under these conditions, to compensate for the angular momentum, the accretion disk must lose a substantial fraction of the matter accreted at its outer edge.

The presence of a strong magnetic field in the accretion disk increases the efficiency of carrying away the angular momentum by the wind [26]. In magnetic−centrifugal models of accretion disks, the parameter f is specified by the ratio of the Alfven radius r_A to the distance from the given point to the symmetry axis of the disk r_0 [27, 28]:

$$f = (r_A/r_0)^{-2}. \qquad (2)$$

According to Ouyed et al., [29], the ratio r_A/r_0 in the disk lies in the range $1.5 < r_A/r_0 < 3$, which corre-sponds to f being in the interval $\approx 0.1-0.4$. Following Shu et al., [27], we will adopt $f = 0.2$.

The second parameter, V_w/V_k, is the ratio of the terminal velocity of the wind V_w (i.e, the velocity a large distance from the secondary) to the orbital velocity of the secondary V_k. This ratio affects the fraction of disk wind material that can be captured by the primary.

The numerical simulations of Goodson et al. [30] suggest that about 80% of the mass lost by a disk wind is via the low-velocity wind component. In the case of T Tauri stars, the velocities of this component at the periphery of the wind region derived from the profiles of forbidden lines are 5−40 km/s [31, 32]. If such a star belonged to a binary that included a more massive component (for example, an Ae/Be Herbig star), the disk-wind material scattered in the course of the orbital motion could all be captured by the primary, even if the distance between the components was of the order of ten astronomical units. This ex-ample shows that the probability that the disk-wind material is captured by the primary can be close to 100%.

3. COMMON ENVELOPE MODEL

Let us consider a binary system with a low-mass secondary ($M_2/M_1 \ll 1$) moving along a circular or-bit with radius R. The secondary accretes matter from the CB disk at a rate $\dot{M}_2 = \dot{M}_a$, which is a parameter of the problem. Some of the matter ($f = 0.2$, see above) is ejected back into the binary in the form of a disk wind. Following Paper I, the disk wind is as-sumed to be axially symmetrical in the reference frame of the secondary. This means that we ignore tidal perturbations in the accretion disk around the low-mass component due to the primary. Note that the influence of tidal forces is important only at the edge of the disk, at distances from the secondary exceeding the Hill radius $r_H = R(M_2/3M_1)^{1/3}$, where M_1 and M_2 are the masses of the primary and secondary. When the component mass ratio $M_2/M_1 \approx 0.1$ and the component separation is $R = 3$ AU, $r_H \approx 1$ AU. Under these conditions, a larger fraction of the accre-tion disk of the low-mass component lies within the

radius r_H, making it possible to neglect its influence on the formation of the disk wind.

For simplicity, we will take the disk wind to be ejected from the accretion disk at 45° to the disk plane. This roughly corresponds to the maximum in the mass flux distribution as a function of polar angle in magnetic−centrifugal disk-wind models [30].

We used a ballistic approximation to calculate the trajectories of particles ejected in the course of the orbital motion of the secondary. This approach is justified by the fact that the disk wind formed in the accretion disk under the action of supersonic turbulence and the pressure of MHD waves should have a non-uniform structure, and, at large distances from the disk, it can be considered a collection of independently moving fragments of gas and dust. In a mathematical description of the trajectories, these fragments can be treated like individual particles.

We denote $\mathbf{V}_w$ to be the terminal-velocity vector for an arbitrary wind particle. By definition, this velocity corresponds to the periphery of the wind area, where the particle moves in accordance with its inertia, having overcome the gravitational force. The azimuthal velocity component, which is equal to the local Keplerian velocity of the accretion disk at the starting point for the particle and decays as r^{-1} at large distances, becomes negligibly small in the peripheral areas of the wind. Therefore, the velocity $\mathbf{V}_w$ can be taken to be purely radial in the reference frame of the secondary.

In the transformation into the center-of-mass frame of the binary (which we take to coincide with the position of the primary, due to the large inequality of the component masses), the particle velocity vector $\mathbf{V}_w$ is summed with the orbital-motion vector of the secondary:

$$\mathbf{V}_0 = \mathbf{V}_w + \mathbf{V}_k. \qquad (3)$$

This value is adopted as the initial velocity of the particle in the gravitational field of the primary. The particles start their motion from the point $\vec{r}$, which moves along a circular orbit, imitating the orbital motion of the secondary.

In the calculations, the secondary orbit was subdivided into steps of 5°. The disk wind was modeled by ejecting test particles from each fixed point of the orbit at an angle of 45° to the disk plane. Taking into account the axial symmetry of the wind, the particles in each ejection were uniformly distributed in azimuth (in the reference frame of the secondary) in steps of 5°. Thus, the total number of test particles ejected by the secondary over an orbital period was 5184. We calculated the motion of each particle while it was moving over (or under) the equatorial plane of the binary. The calculation was stopped when the particle either crossed this plane or moved away from the

center to a distance exceeding 50 orbital radii of the secondary.

Due to the symmetry of the wind about the equatorial plane of the binary, both the numbers and velocities of particles crossing this plane from above and below at any point should be equal. As a result, the vertical velocity components of particles falling onto the equatorial plane from opposite sides will cancel each other out in collisions (and the motional energy will be transformed into heat), and a geometrically thin disk will be formed[1]. The matter that ends up inside the secondary orbit is captured by the accretion disk of the primary. The rest of the matter falls onto the equatorial plane beyond this orbit and is captured by (or, more precisely, returns to) the CB disk. The structure of the inner disk, which specifies the accretion activity of the primary, must be studied using a gas-dynamical approach; this is the subject of a separate study. When calculating the IR luminosity of the inner disk and CB disk, we assumed that, on the whole, their structures were similar to that of a flaring disk around a single star whose parameters coincide with those of the primary. The inner and outer radii of the flaring disk were taken to be the same as those adopted for the Ae/Be Herbig star AB Aur in [11], which we will consider in Section 4.

We did not take into account the wind from the accretion disk around the primary, since it is appreciably less intense than the disk wind from the secondary in the model considered. Note that the role of the primary should be more important in the formation of the high-velocity component of the wind.

As an example, Fig. 1 presents the particle distribution in a common-envelope model with a disk-wind velocity of $V_w = 1$ (here and below, we take the orbital velocity of the secondary to be unity). The impact of the binary parameters on the structure of the common envelope is considered in more detail in [33]. We note here only that this structure differs appreciably from the matter distributions in models of young binaries calculated in the studies of Artimowicz and Lubow [22] and Bate and Bonnell [23]. In those models, the role of the secondary is restricted to inducing periodic gravitational perturbations in the CB disk. Under the action of these perturbations, density waves originate in the CB disk and two streams are formed, which periodically penetrate into the inner region of the binary. Both the thickness and vertical structure of the disk remain roughly the same as in the case of a single star.

In the case considered here, the role of the secondary is more active: it becomes a source of matter,

---

[1]In reality, due to the presence of density and velocity fluctuations in the disk wind, the vertical velocity components will not totally cancel, so the disk will have a finite thickness.
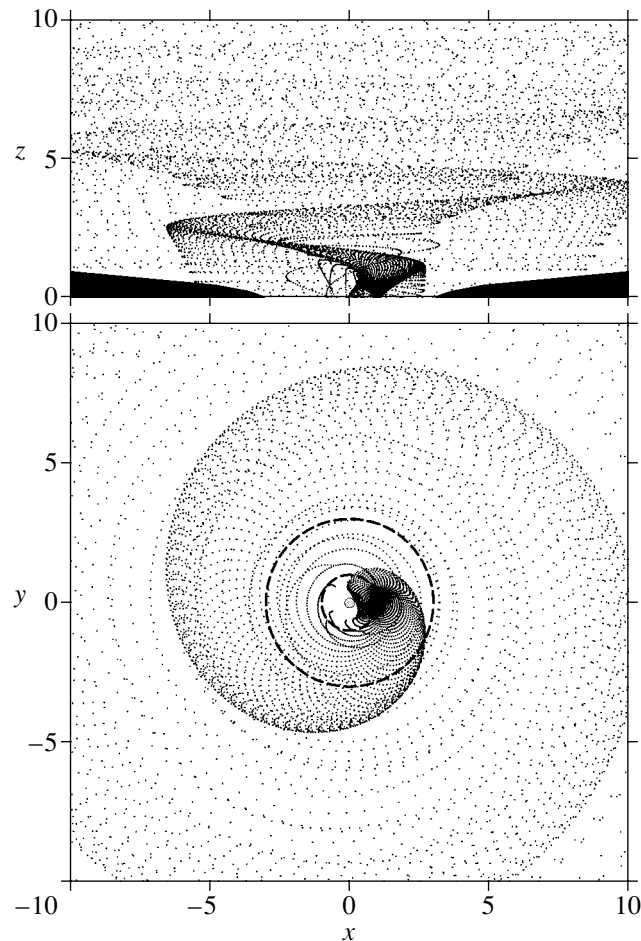
Fig. 1. Distribution of particles in the common envelope (Model 3) in the xz plane (top) and projected onto the equatorial plane of the binary (bottom). The orbital radius of the secondary is taken to be unity. The coordinates of the primary and secondary in the xy plane are (0,0) and (1,0), respectively. The dashed curves indicate the orbit of the secondary (small circle) and the inner boundary of the CB disk with radius ≈3. The CB disk is shown schematically in the upper graph.

which it scatters in the course of its orbital motion. The result is the formation of a common envelope with rather complicated spatial and kinematic characteristics (Fig. 1). In projection onto the equatorial plane of the binary, it resembles the spiral-like pattern that arises in some models for close binaries [34].

4. THE INFRARED RADIATION OF THE COMMON ENVELOPE

To calculate the IR flux, we must determine the temperature and density of the dust at various distances from the primary. To this end, we assumed that the CB disk consisted of a gas–dust mixture with the standard ratio of the masses of the dust and gas components for the interstellar medium (1/100). We also adopted this dust-to-gas ratio for the disk wind from the low-mass component, since the bulk of the wind is formed in the low-temperature region of the accretion disk, where the temperature is below

the melting point of the dust particles so that they (excluding ice) did not have time to sublimate. Note that dust is preserved to distances of several stellar radii in the accretion disks of T Tauri stars [35].

Using the above procedure, we calculated the distribution of dust in the binary for the following sets of parameters:

Model Parameters

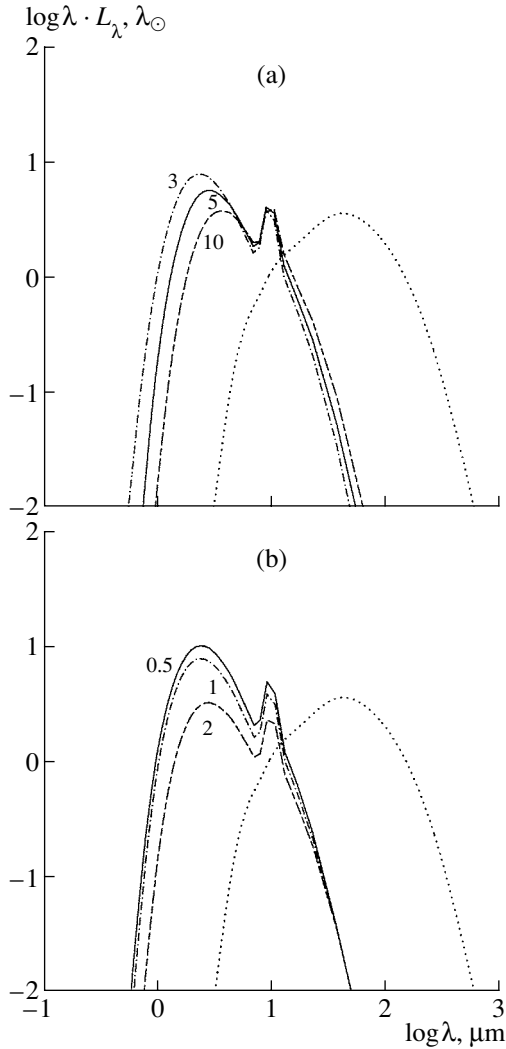| Model	V_w	R, AU	M_d, $M_\odot$
1	0.1	3	2.3×10^{-10}
2	0.5	3	8.8×10^{-10}
3	1	3	1.4×10^{-9}
4	2	5	1.8×10^{-9}
5	1	5	3.2×10^{-9}
6	1	10	9.0×10^{-9}

Fig. 2. Infrared SED for the common-envelope radiation in Models (a) 3, 5, and 6 and (b) 2, 3, and 4. The numbers 3, 5, and 10 indicate the orbital radius of the secondary in AU; the numbers 0.5, 1, and 2 indicate the dimensionless disk-wind velocity. For comparison, the dotted curves in both plots indicate the SED of the flaring disk of AB Aur taken from Natta *et al.* [11].

(1) The rate of accretion onto the secondary $\dot{M}_2 = \dot{M}_a = 3 \times 10^{-8} M_\odot$ (note that, according to Calvet *et al.* [36], this $\dot{M}_a$ corresponds roughly to the average accretion rate onto a T Tauri star).

(2) The dimensionless terminal velocity for the disk wind takes on several values in the interval $V_w = 0.1 - 2$.

(3) The efficiency factor $f = 0.2$.

(4) The ratio of the numbers of graphite and silicate particles is standard for the interstellar medium: $N_{sil}/N_{gra} = 1.12$ [37]; spherical dust particles with radius $a = 0.1 \mu$m and density 3 g/cm^3 are considered.

We chose such particles for two reasons: (1) studies of the circumstellar dust responsible for circumstellar extinction and the reddening of young stars indicates that the composition of the dust particles is approximately the same as in the interstellar medium, with the only significant difference being that the size of the dust particles is somewhat larger [38]; (2) calculations indicate that fine dust makes the largest contribution to the IR excess at near-IR wavelengths.

The transformation from test particles, whose number density was calculated in a ballistic approximation, to real dust grains was carried out by rescaling. We took into account the ratio of the total number of real dust grains ejected by the wind over an orbital period and the corresponding number of test particles (see above). The table presents the parameters of the models studied and the total dust mass in the common envelope M_d calculated using the above method. We can see that, for a fixed rate of mass loss in the form of the disk wind, M_d depends on both the orbital radius R and the ratio of the wind velocity with the orbital velocity of the secondary. For fixed R, this value decreases with the wind velocity V_w and increases with R for fixed V_w. In both cases, the mass of the common envelope is proportional to the average time that particles of the disk wind spend until they cross the equatorial plane of the system or move beyond the envelope region considered (recall that we took its radius to be 50 orbital radii of the secondary).

The calculated models indicate that the common envelope can be opaque to both the optical and UV radiation of the primary in the immediate vicinity of the secondary. The rest of the common envelope is either partially transparent or optically thin. This enables us to consider the thermal balance of the dust in the approximation of an optically thin medium:

$$\frac{1}{4\pi r^2} \int_0^\infty Q_{\mathrm{abs}}(a, \lambda) L_*(\lambda) d\lambda \qquad (4)$$

$$= 4\pi \int_0^\infty Q_{\mathrm{abs}}(a, \lambda) B_\lambda(T_d) d\lambda.$$

Here, r is the distance from a particle to the primary, $Q_{\mathrm{abs}}(a, \lambda)$ the efficiency for the absorption of radiation at wavelength λ by a particle with radius a, $L_*(\lambda)$ the luminosity of the star at wavelength λ, and the other notation is standard. We calculated Q_{abs} using Mie theory. The optical parameters for graphite and silicate (for definiteness, we considered p-obsidian) were taken from [39, 40].

The solutions to (4), obtained separately for graphite and silicate dust grains, enable us to determine the dust temperature T_d as a function of
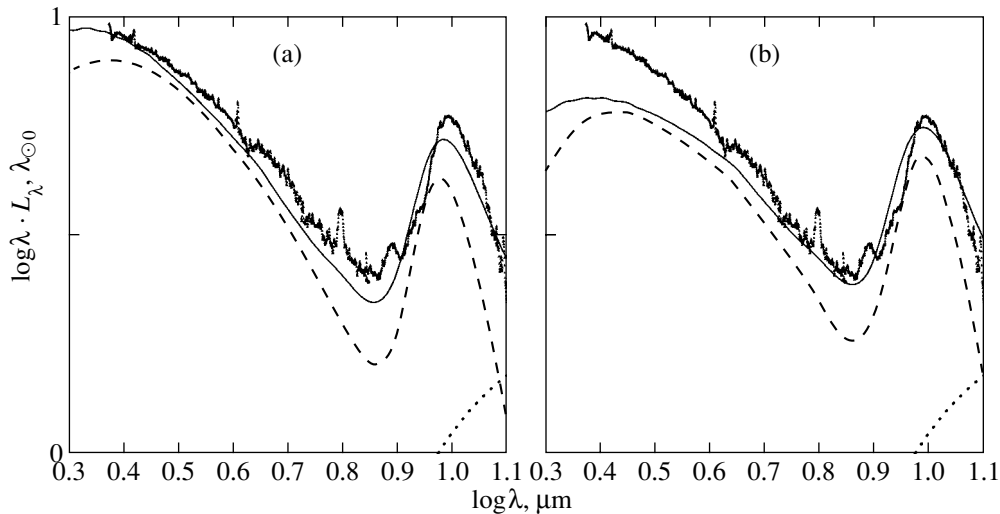
Fig. 3. Near-IR SED of AB Aur according to ISO data (Bouwman *et al.* [45], thick solid line) and the theoretical SEDs for Models (a) 3 and (b) 5. The dashed curve shows the radiation of the common envelope, and the thin solid curve, the combined radiation of the star, common envelope, and flaring disk. The dashed lines in the bottom right corners of both plots display a fragment of the IR SED for the flaring disk of AB Aur from Natta *et al.* [11].

the distance to the primary then to calculate the IR luminosity of the common envelope:

$$L_{\mathrm{en}}(\lambda) = 4\pi^2 a^2 Q_{\mathrm{abs}}(a, \lambda) \tag{5}$$

$$\times \int_{r_1}^{r_2} B_\lambda(T_{\mathrm{d}}) N_d(r) dr.$$

Here, $N_d(r)dr$ is the number of particles at distances from r to $r + dr$ from the primary.

We assumed that the temperature of the primary is $T_{ef} = 10^4 K$ and its luminosity is $L_* = 50 L_\odot$, close to those of the Ae/Be Herbig star AB Aur [11], which will be considered in the next section. When calculating the temperature of a particle in the common envelope in accordance with (1), we used the normalized radiation fluxes for the models of Kurucz [41] for a star with the above temperature and $\log g = 3.5$.

Figure 2 presents the IR spectral energy distributions calculated for several models whose parameters are given in the Table. For comparison, the SED of the flaring disk of AB Aur [11] is also shown. We can see that the luminosity of the common envelope and circumstellar disk are comparable, in spite of the fact that the dust mass in the envelope (see Table) is many orders of magnitude smaller than the dust masses in the circumstellar disks of young stars [42]. Though at first paradoxical, this result can be understood as a consequence of the fact that the disk IR radiation is emitted by a thin surface layer of dust, whose mass is comparable to that of the common envelope. In addition, the disk gives rise to most of the radiation

at far-IR wavelengths, whereas the common envelope radiates primarily at wavelengths of $1-10\mu m$.

We can see from Fig. 2b that a decrease in the dimensionless wind velocity (with other model parameters fixed) results in an increase in the IR luminosity of the common envelope. This is because, at high velocities, the disk-wind material leaves the binary entirely and the remaining common envelope is rather rarefied. At small velocities, a large fraction of the wind material is captured by the primary. As a result, the common envelope becomes more compact and concentrated around the low-mass component. Estimates indicate that, in addition, the optical depth of the envelope at optical and UV wavelengths increases. Therefore, beginning with some V_w, a larger fraction of the envelope becomes opaque to the stellar radiation and the diffusion of the radiation must be taken into account when calculating the radiation field.

When the orbital radius of the secondary is increased (with other model parameters fixed), the average distance between the dust grains in the envelope and the primary also increases. This decreases the dust temperature and shifts the maximum of the IR SED toward longer wavelengths (Fig. 2b).

We do not present the relation between the IR luminosity of the common envelope and the rate of accretion onto the secondary here, since it is trivial in the approximation of an optically thin envelope: $L_{en} \propto \dot{M}_a$. We note only that the contribution of the common envelope to the radiation of the young star at near-IR wavelengths becomes appreciable starting
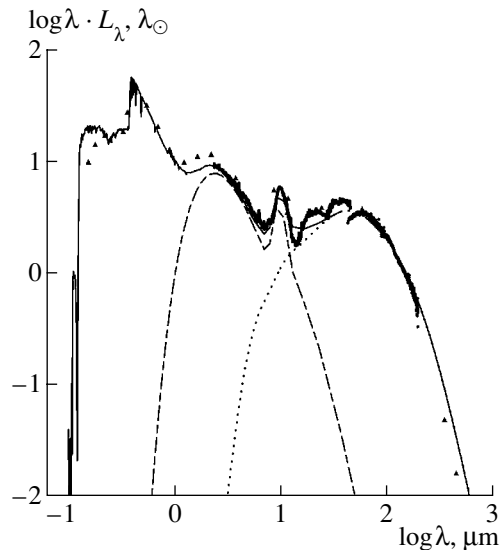
Fig. 4. Total SED for AB Aur according to ISO data [48] (thick solid curve) and ground-based observations at optical and submillimeter wavelengths ([49] and references therein; circles and triangles). The dashed curve shows the common-envelope radiation (Model 3) based on data from the present study; the dotted curve shows the radiation of a flaring disk according to Natta *et al.* [11]. The thin solid curve shows the total SED of a star derived from a Kurucz model (see text) with a common envelope (Model 3) and flaring disk.

roughly from $\dot{M}_a = 3 \times 10^{-9} M_\odot$/yr. Estimates suggest that the compact thermal radiation of the common envelope remains detectable against the background of the disk thermal radiation for even smaller $\dot{M}_a$. The isophotes of the common envelope at IR and visible wavelengths (scattered radiation) will be considered in more detail in a separate study.

To illustrate the possibilities offered by the model considered, we compare our calculated SEDs with IR data for AB Aur, one of the most thoroughly studied Ae/Be Herbig stars, often considered a prototype for young intermediate-mass stars [43]. According to Natta *et al.* [11], the effective temperature and luminosity of this star are $T_{\rm eff} = 9500$ K and $L_* = 48L_\odot$; i.e., they are close to the parameters for the above model. In their image of AB Aur obtained with the Hubble Space Telescope, Grady *et al.* [44] were able to resolve the circumstellar disk and estimate the inclination of the disk axis to the line of sight to be $<35°$. This disk orientation makes it possible to use theoretical SEDs calculated for the case when the disk is viewed pole-on.

Figure 3 presents the near-IR SED of AB Aur based on data obtained with the ISO observatory, taken from Bouwman *et al.* [45]. The same figure presents theoretical IR SEDs for two models with different radii for the secondary orbit, 3 and 5 AU. The remaining model parameters, including the rate of accretion onto the low-mass component ($\dot{M}_a = 3 \times 10^{-8} M_\odot$/yr) and the disk-wind velocity ($V_w = 1$), are the same. We can see that the first and second model SEDs are consistent with the short-wavelength and long-wavelength end of the IR spectrum of the star, respectively. It follows that a model with an intermediate orbital radius provides the best overall agreement between the theory and observations over the entire wavelength interval considered.

Figure 4 presents the total SED of AB Aur based on ISO data [45] supplemented by the results of some ground-based observations (see the study of Mannings [46] and references therein), together with the theoretical SED for the above model from UV through IR wavelengths. We can see that the model satisfactorily reproduces the observations over virtually the entire IR spectral range. At near-IR wavelengths ($\approx 1-10\mu m$), most of the radiation is provided by the common envelope, whereas in the far-IR it comes primarily from the flaring disk.

5. DISCUSSION

These results indicate that infrared excesses in the radiation of young stars in the near-IR depend strongly on whether the star is single or a member of a binary (or multiple) system. Unlike models of close binaries, which include a donor and accretor (see, for example, [47]), in our model the secondary plays the role of an intermediator, transferring matter from the remnants of the protostellar cloud into the central area of the binary. The efficiency of this process depends on the mechanism for the formation of the disk wind (the parameter f) and the orbital radius of the secondary. We have adopted the value $f = 0.2$ in the calculations but noted that, theoretically, this parameter may be close to unity in certain situations.

Unlike the models of young binaries considered by Artimowicz and Lubow [22], in which matter is transfered into the central region of the system by two streams that periodically emerge in the CB disk due to the combined effect of viscosity and tidal perturbations, in our case, viscosity does not affect the efficiency of the two-step accretion in any way. Optimal values of the dimensionless disk-wind velocity (which depend on both the mass of the primary and the orbital radius of the secondary) lie in the interval $V_w \approx 0.3-1$. For the disk-wind velocities characteristic of low-mass, young T Tauri stars (5–40 km/s) and a primary mass of about $1M_\odot$, this interval of dimensionless disk-wind velocities corresponds to distances to the primary of about 1–10 AU.

In addition to these two parameters, the power of the common envelope also depends on the rate of accretion onto the low-mass component, which, in

turn, depends on the power of the CB disk and the distance from it to the secondary orbit. If a young system forms a very close binary (for example, an eclipsing system), or, on the contrary, a very wide (visual) binary, the secondary orbit will be located far from the bulk of the material remaining after the formation of the binary. The rate of accretion onto the secondary in these cases will be small. Thus, we again conclude that, in order to obtain a powerful common envelope, the radius of the secondary's orbit must be of the order of several astronomical units.

Such distances between the binary components present the most difficulty in attempts to detect the binarity of the star, since the amplitude of radial-velocity variations due to the orbital motion of the stars will be small and the probability of eclipses is also very low. At the same time, such binaries are not wide enough to be resolved with a telescope. It is quite possible, therefore, that many young stars now considered to be single are, in fact, binary or multiple systems, with their near-IR excesses providing the only evidence for their binarity.

In this connection, it would be very interesting to test for the binarity of AB Aur. If the above model for its IR radiation is valid, then this star (which is presently considered to be single) should be a binary, or even multiple, system. According to Fig. 1, its image at near-IR wavelengths should display a characteristic, amorphous comma-shaped feature representing the common envelope. For a distance to AB Aur of 140 pc [11], the angular resolution necessary to obtain an IR image of the envelope should be about $0.03''$.

5.1. Some Consequences

Let us consider briefly the most interesting consequences arising from the above model.

(1) As noted above, the basic feature of the two-step accretion model is that it provides a supplementary inflow of material into the central region of the binary. In the model proposed by Artimowicz and Lubow [22], the central lobe of the binary is periodically penetrated by two streams of matter from the CB disk, which, according to their estimates, fill up to about 10% of the lobe volume. However, the recent observations of the young binary DQ Tau of Carr *et al.* [48] indicate that the filling factor for its central lobe is appreciably higher.

This inconsistency can now be eliminated: a supplementary inflow of material into the inner region of the binary can be provided by the disk wind from the secondary that is captured by the primary.

(2) The existence of a common envelope formed by the mechanism described above also opens new

opportunities for the interpretation of a number of phenomena observed in young stars and still generally unexplained. We noted some of these in Paper I, in particular, the fact that the asymmetrical shape of a common gas–dust envelope (Fig. 1), whose densest part coincides with the low-mass component, should result in a periodic modulation of the radial density with the orbital period. This modulation can be manifest both as a periodic enhancement of circumstellar absorption lines (shell components) and as an increase in the circumstellar extinction due to the dust component of the common envelope. This problem is considered in more detail in [33], in the context of interpreting the activity cycles of UX Ori stars.

(3) Another important consequence of the asymmetrical shape of the envelope is that the optical radiation of the primary scattered in the envelope may be polarized substantially more strongly than in axially symmetrical models for circumstellar dust disks and envelopes. This makes it possible to understand the results of polarization observations of some UX Ori stars at epochs of deep minima, when a very high linear polarization for the scattered radiation was detected (10% and higher [49]), which is difficult to explain using axially symmetrical circumstellar-disk models.

(4) Unlike axially symmetrical models for circumstellar disks and envelopes, which predict zero linear polarization when observed pole-on, our model predicts that the radiation of a young star will be polarized for this disk orientation. In the case of a circular secondary orbit, the polarization position angle will vary with a period equal to half the orbital period, while a two-component polarization cycle with a period equal to the orbital period should be observed in the case of an elliptical orbit. This simple theoretical prediction can be used to search for young binaries via polarimetric monitoring.

Note that none of these effects is predicted by the models for accretion disks around single young stars mentioned in the Introduction, including hybrid "disk + spherically symmetrical envelope" models, due to their axial symmetry.

6. CONCLUDING REMARKS

Our study, as well as Paper I, indicates that current theoretical models for young binaries (see the reviews of Lin and Papaloizou [50], Lubow and Artimowicz [51], and references therein), in which the secondary is considered only as a source of periodic gravitational perturbations, must be supplemented with a new element: a disk wind from the secondary. In this case, the secondary plays the more active role of an intermediator between the primary and the remnants of the protostellar cloud surrounding

the young binary. Its new functions are: (a) a large-scale redistribution of the angular momentum of the accreting matter, which is more efficient compared to local mechanisms based on turbulent and magnetic viscosity; (b) the formation of a common envelope. As a result, a powerful additional source of thermal and scattered radiation arises, and the inflow of matter into the central region of the binary increases, thereby increasing the accretion activity of the primary. In addition, the dust component of the common envelope produces a periodic screening effect, which can result in cyclic variability of the brightness of the young binary in both the optical and infrared, in particular, due to the formation of a variable zone of shadowing in peripheral regions of the flaring disk.

For simplicity, we restricted our consideration to a binary with a circular orbit, when the probability of capture of wind from the secondary is the same along the whole length of its orbit. In the general case of an elliptical orbit, this important parameter becomes a periodic function of time. As a result, another effect can be added to those considered above: a pulsed regime of accretion onto the primary. This is of interest in the context of possible pulsed regimes of matter outflow from the accretion disk around the primary and the formation of the periodic structures observed in the narrow, collimated jets ejected from young stars (see, e.g., [52]). It is also apparent that the parameters of the common envelope should vary periodically in the case of an elliptical orbit, which should be manifest as periodic modulations of the IR radiation of young stars, and also of the Stokes parameters of scattered radiation at optical wavelengths, which should be substantially more powerful than in the case of a circular orbit. We will consider these effects in a subsequent study.

7. ACKNOWLEDGEMENTS

REFERENCES

1. V. E. Mendoza, Astrophys. J. **143**, 1010 (1996).
2. M. Cohen, Mon. Not. R. Astron. Soc. **173**, 279 (1975).
3. A. E. Rydgren, S. E. Strom, and K. M. Strom, Astrophys. J., Suppl. Ser. **30**, 307 (1976).
4. L. A. Hillenbrand, S. E. Strom, F. Vrba, and J. Keene, Astrophys. J. **397**, 613 (1992).
5. K. Malfait, E. Bogaert, and C. Waelkens, Astron. Astrophys. **331**, 211 (1998).
6. F. C. Adams, C. J. Lada, and F. H. Shu, Astrophys. J. **312**, 788 (1987).
7. L. Hartmann, New Astron. Rev. **43**, 1 (1999).
8. S. J. Kenyon and L. Hartmann, Astrophys. J. **323**, 714 (1987).
9. A. Natta, Astrophys. J. **412**, 761 (1993).
10. E. I. Chiang and P. Goldreich, Astrophys. J. **490**, 368 (1997).
11. A. Natta, T. Prusti, and R. Neri, *et al.*, Astron. Astrophys. **371**, 186 (2001).
12. E. I. Chiang, M. K. Joung, M. J. Creech-Eakman, *et al.*, Astrophys. J. **547**, 1077 (2001).
13. C. P. Dullemond, C. Dominik, and A. Natta, Astrophys. J. **560**, 957 (2001).
14. N. Calvet, L. Hartmann, S. J. Kenyon, and B. A. Whitney, Astrophys. J. **434**, 330 (1994).
15. A. Miroshnichenko, Z. Ivezić, D. Vinković, and M. Elitzur, Astrophys. J. Lett. **520**, L115 (1999).
16. A. Miroshnichenko, Z. Ivezić, and M. Elitzur, Astrophys. J. Lett. **475**, L41 (1997).
17. N. A. Krivova, Pis'ma Astron. Zh. **23**, 371 (1997) [Astron. Lett. **23**, 327 (1997)].
18. S. Pezzuto, F. Strafella, and D. Lorenzetti, Astrophys. J. **485**, 290 (1997).
19. A. M. Ghez, in *Processes in Binary Stars,* Ed. by R. A. M. J. Wijers *et al.* (Kluwer, Dordrecht, 1996), p. 1.
20. R. D. Mathieu, in *Processes in Binary Stars,* Ed. by R. A. M. J. Wijers *et al.* (Kluwer, Dordrecht, 1996), p. 11.
21. V. P. Grinin, Astrofizika **43**, 603 (2000).
22. P. Artimowicz and S. H. Lubow, Astrophys. J. Lett. **467**, L77 (1996).
23. M. R. Bate and I. A. Bonnell, Mon. Not. R. Astron. Soc. **285**, 33 (1997).
24. N. I. Shakura and R. A. Sunyaev, Astron. Astrophys. **24**, 337 (1973).
25. D. Lynden-Bell and F. E. Pringle, Mon. Not. R. Astron. Soc. **168**, 603 (1974).
26. R. D. Blandford and D. G. Payne, Mon. Not. R. Astron. Soc. **199**, 883 (1982).
27. F. Shu, J. Najita, D. Galli, *et al.*, in *Protostars and Planets III,* Ed. by E. H. Levy and J. I. Lunine (Univ. of Arizona Press, Tucson, 1993), p. 3.
28. A. Königl and S. P. Ruden, in *Protostars and Planets III,* Ed. by E. H. Levy and J. I. Lunine (Univ. of Arizona Press, Tucson, 1993), p. 641.
29. R. Ouyed, R. E. Pudritz, and J. M. Stone, Nature **385**, 409 (1997).
30. A. P. Goodson, K.-H. Böhm, and R. Winglee, Astrophys. J. **524**, 142 (1999).
31. G. A. Hirth, R. Mundt, and J. Solf, Astron. Astrophys. **285**, 929 (1994).
32. P. Hartigan, S. E. Edwards, and L. Ghandour, Astrophys. J. **452**, 736 (1995).
33. V. P. Grinin and L. V. Tambovtseva, submitted to Mon. Not. R. Astron. Soc. (2002).
34. N. Mastrodemos and M. Morris, Astrophys. J. **497**, 303 (1998).

35. J. Bouvier, A. Chelli, S. Allain, *et al.*, Astron. Astrophys. **349**, 619 (1999).

36. N. Calvet, L. Hartmann, and S. E. Strom, in *Protostars and Planets IV,* Ed. by V. Mannings, A. P. Boss, and S. S. Russell (Univ. of Arizona Press, Tucson, 2000), p. 377.

37. B. T. Draine and H. M. Lee, Astrophys. J. **285**, 89 (1984).

38. N. V. Voshchinnikov and V. P. Grinin, Astrofizika **34**, 181 (1991).

39. J. B. Pollack, O. B. Toon, and B. M. Khare, Icarus **19**, 372 (1973).

40. P. L. Lamy, Icarus **34**, 68 (1978).

41. R. L. Kurucz, Astrophys. J., Suppl. Ser. **40**, 1 (1979).

42. A. Natta, V. P. Grinin, and V. Mannings, in *Protostars and Planets IV,* Ed. by V. Mannings, A. Boss, and S. S. Russell (Univ. of Arizona Press, Tucson, 2000), p. 559.

43. T. Böhm and C. Catala, Astron. Astrophys., Suppl. Ser. **101**, 629 (1993).

44. C. A. Grady, B. Woodgate, F. C. Bruhweiler, *et al.*, Astrophys. J. Lett. **523**, L151 (1999).

45. J. Bouwman, A. de Koter, M. E. van den Ancker, and L. B. F. M. Waters, Astron. Astrophys. **360**, 213 (2000).

46. V. Mannings, Mon. Not. R. Astron. Soc. **271**, 587 (1994).

47. D. V. Bisikalo, A. A. Boyarchuk, O. A. Kuznetsov, and V. M. Chechetkin, Astron. Zh. **77**, 31 (2000) [Astron. Rep. **44**, 26 (2000)].

48. J. S. Carr, R. D. Mathieu, and J. Najita, Astrophys. J. **551**, 454 (2001).

49. A. N. Rostopchina, V. P. Grinin, and D. N. Shakhovskoĭ, Astron. Zh. **78**, 60 (2001) [Astron. Rep. **45**, 51 (2001)].

50. D. N. C. Lin and J. C. B. Papaloizou, in *Protostars and Planets III,* Ed. by E. H. Levy and J. I. Lunune, (Univ. of Arizona Press, Tucson, 1993), p. 749.

51. S. H. Lubow and P. Artimowicz, in *Protostars and Planets IV,* Ed. by V. Mannings, A. P. Boss, and S. S. Russell (Univ. of Arizona Press, Tucson, 2000), p. 731.

52. H. Zinnecker, M. J. McCaughrean, and J. T. Rayner, Nature **394**, 862 (1998).

Translated by K. Maslennikov

A Method for Modeling the Formation of CaII Lines in the Spectra of Irradiated Stellar Atmospheres

D. V. Ivanova, N. A. Sakhibullin, and V. V. Shimanskiĭ

Kazan State University, ul. Lenina 18, Kazan, 420008 Tatarstan, Russia
Received February 5, 2001

Abstract—We have developed a method for calculating deviations from LTE of level populations and profiles of selected spectral lines in stellar atmospheres in the presence of external radiation. The influence of Thomson scattering at the frequencies of the external radiation is considered. The method used to calculate model irradiated atmospheres in a semi-grey approximation has been improved. We have modified the NONLTE3 code used to determine the level populations to make it suitable for irradiated atmospheres. A model for the CaII atom including 42 energy levels of CaII, the ground state of CaIII, and 80 linearized transitions was constructed for these calculations. This atomic model takes into account the effect of all relevant collisional processes and radiative processes at the frequencies of the internal and external radiation. We investigated the correctness of the non-LTE calculations for the CaII ion by analyzing 16 lines of ionized calcium in the solar spectrum. The influence of uncertainties in the atomic data on the non-LTE level populations and CaII line profiles was also analyzed, and the van der Waals broadening coefficients C_6 were refined. The scaling coefficient in the Dravin formula was taken to be 0.1. We found the non-LTE abundance corrections for most lines to be significant ($\Delta \log \varepsilon(\mathrm{Ca}) = 0.05 - 0.15 \mathrm{dex}$), even under the conditions for the solar atmosphere. The lines of the $\lambda = 8498, 8542, 8662$ Å infrared triplet can be adequately described. Differences in the mean calcium abundance obtained using different model atmospheres are smaller than 0.02 dex. Our final estimate of the mean calcium abundance in the solar atmosphere is $\log \varepsilon(\mathrm{Ca}) = 6.31$, in good agreement with the meteoritic abundance, $\log \varepsilon(\mathrm{Ca}) = 6.32$.
© 2002 MAIK "Nauka/Interperiodica".

1. INTRODUCTION

Modeling atmospheres has become one of the most promising tools for studying the emission of close binary systems. Its undoubted advantage is the ability to construct realistic models of binaries, directly and numerically taking into account all physical phenomena affecting their emission. Modeling atmospheres is the most efficient method for analyzing the line spectra of close binary systems, when the large amount of high-quality initial data make it possible to determine the state of the system and derive complete information about its characteristics (e.g., the component parameters, velocity fields at their surfaces, mass transfer rates, and so on).

Nevertheless, when applied to studies of the spectra of close binary systems, this method can lead to substantial errors if the calculations assume local thermodynamic equilibrium (LTE). As was found in [1, 2] based on an ionization-balance analysis, deviations from LTE are considerably stronger for irradiated stellar atmospheres in binary systems, and their character is different from the analogous deviations for single stars. The main reason for these large non-LTE effects is the presence of several sources of radiation in close binary systems. As a result, the ra-

diation fields in the atmospheres of their components are extremely nonuniform, making them incompatible with the assumptions of LTE. Such non-LTE effects are most significant in the upper atmospheric layers, where the irradiation is highly anisotropic, i.e., precisely in the regions in which lines are formed. Specific features of the non-LTE deviations for particular atoms depend on the efficiency of their interaction with the internal and external radiation fields.

This conclusion was confirmed by later studies using multilevel atomic models taking into account all significant collisional and radiative processes. The analysis of non-LTE effects for HeI lines in the atmospheres of B stars of Mitshevich and Tsymbal [3] showed that these effects increase sharply in the presence of external X-ray radiation with an amplitude of $10^{-7}-10^{-8}$ of the internal radiation of the star. The deviations from LTE, which are manifest as an overpopulation of the next ionization state, HeII, and the presence of highly-excited levels of HeI, depend on the ionization of atoms only by the external radiation, while radiative processes in the optical are negligible. As a result, a superionization state is formed, with the appearance of emission components in the line profiles. The opposite effect was found by Sakhibullin

and Shimanskiĭ [4] in their non-LTE study of the formation of NaI lines in the irradiated atmospheres of F−K stars. Ionization by external radiation is not appreciable for NaI atoms, and recombination and deexcitation via cascade transitions in the optical become the dominant processes. The combination of these processes results in the formation of a super-recombination state, in which the lower levels of NaI are overpopulated and the absorption components of all lines are enhanced compared to the LTE case.

The above results show that the profiles of the HeI and NaI lines are distorted by non-LTE effects and do not reflect the real temperatures in the atmospheres of the irradiated stars. On the other hand, non-LTE calculations are computer intensive, and it is not feasible to apply them for spectral analyses of individual stellar systems on a massive scale. Therefore, it remains important and useful to search for lines with minimal deviations from LTE, suitable for analyses of temperature distributions in the atmospheres of irradiated stars. Very strong lines of elements in the main ionization state are of particular interest in this search. For A−M stars, these requirements are obviously best satisfied for the H and K lines of the CaII resonant doublet. They are the strongest metal lines over a wide range of temperature, $T_{\text{eff}} = 4000-12\,000$ K, and are often used in studies of the chromospheres of the Sun [5−7] and single stars of late spectral classes [8−11]. The results of such investigations demonstrate that the lines of ionized calcium are good indicators of chromospheric activity and can be used to determine chromospheric structure. At the same time, the authors of these studies have indicated the presence of evident deviations of the CaII line profiles from LTE, resulting in a weakening of their emission components.

In addition, studies of non-LTE deviations of the H and K lines is important for theoretical calculations of the temperature structure of irradiated atmospheres. The contribution of these lines to the gas cooling function for solar-type stars may be as large as 30−50%. As a result, possible non-LTE deviations for the CaII levels could considerably affect the total cooling function and the temperature structure of the irradiated atmosphere.

Finally, we note that the CaII ion has a fairly simple structure for its terms, for which a set of atomic data has been established with high accuracy, and the parameters of the lines of the $\lambda = 3933, 3968$ Å resonant doublet and $\lambda = 8498, 8542, 8662$ Å infrared triplet have been studied in detail.

The analysis of non-LTE effects in the CaII ion in stellar atmospheres with external radiation and the use of its lines for analyses of the spectra of close binary systems in an LTE approximation will

be presented in two other papers. The method for deriving LTE models for the atmospheres of irradiated stars is described in Section 2.1 of the present paper, the method used to calculate the non-LTE level populations and line profiles, in Section 2.2, and the resulting model CaII ion, in Section 2.3. Section 3 is dedicated to an analysis of the results of our modeling of CaII lines in the solar spectrum and determination of the unknown atomic parameters. The results of our calculations of non-LTE effects for the CaII ion in stellar atmospheres irradiated by X-ray and ultraviolet radiation and their influence on the spectra of close binary systems will be described in a future paper.

2. CALCULATION METHOD

To carry out the calculations, we used and improved the two-step method introduced earlier by Sakhibullin and Shimanskiĭ [4], which includes the following two stages.

(1) The models for the irradiated atmospheres were determined in an LTE approximation taking into account reflection effects in a semi-grey approximation, implemented in the BINARY2 code [12] of the SPECTR package [13]. We verified the accuracy of the models obtained using the BINARY3 [14] code for the calculation of blanketed atmospheres with both convective and radiative transfer.

(2) The CaII level populations and line profiles were calculated using a complete linearization method implemented in the NONLTE3 code [12].

We implemented some changes and additions in both methods, which will be discussed below in more detail.

2.1. Calculation of the Model Atmospheres

The method used to model the reflection effects in a semi-grey approximation is based on calculating models for stellar atmospheres with external radiation by balancing the heating function for the external radiation and the cooling function for the star's proper radiation [12]. This approach yields a correct qualitative description of the temperature in the irradiated atmospheres, and possesses high accuracy if the optical absorption coefficient α_v is correctly chosen [14]. The grid of blanketed models of Kurucz [18] with solar composition were used as initial models. We introduced the following changes to the existing method to increase the accuracy of the resulting model atmospheres.

I. Thomson scattering was taken into account when solving the transfer equation at the frequencies of the external radiation. We ensured the conservation of the distribution of the external radiation as a δ function with the angle of incidence given by $I(\mu') =$
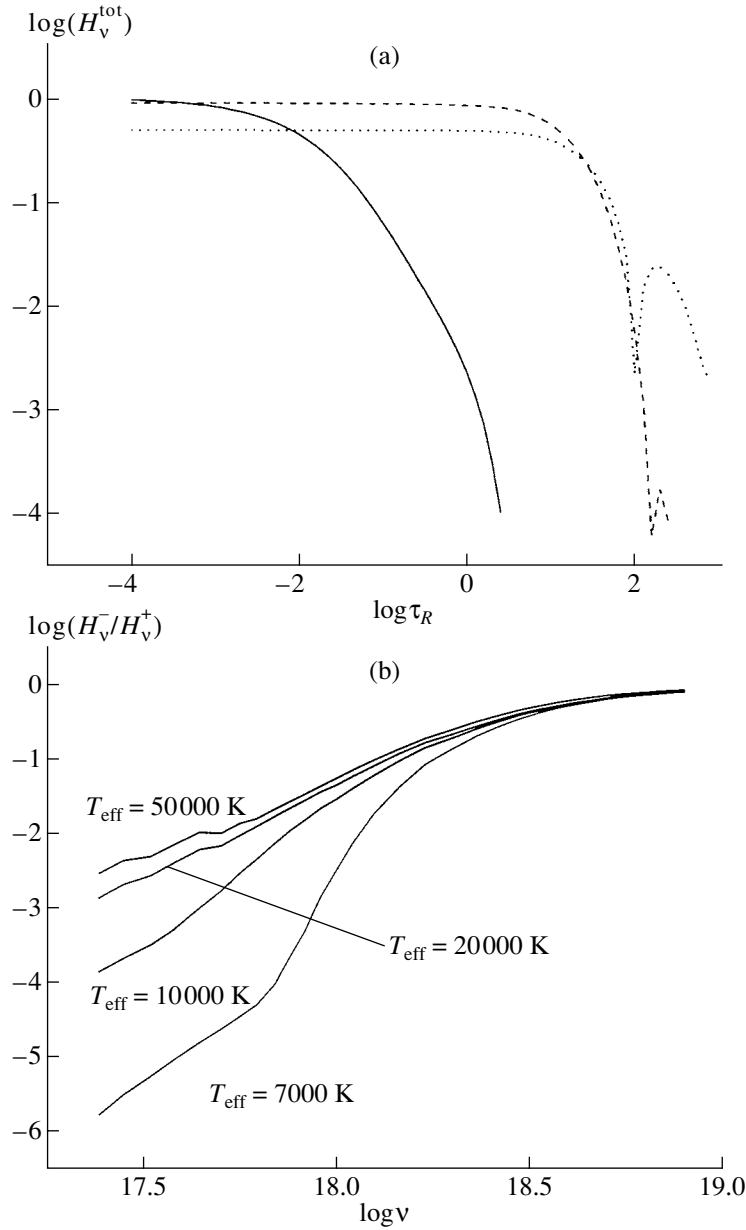
Fig. 1. (a) Distribution of the total fluxes H_ν^{tot} in the atmosphere with $T_{\text{eff}} = 10\,000$ K and $\log g = 4.0$ for unit external irradiation I_ν^+ at $E_\nu = 1.0$ keV (solid curve), $E_\nu = 6.0$ keV (dashed curve), and $E_\nu = 20.0$ keV (dotted curve). (b) Albedos of atmospheres with $\log g = 4.0$ and various T_{eff} in at $E_\nu = 1.0–40.0$ keV.

$I\delta(\mu' - \mu)$ (where $\mu = \cos\theta$) for all layers of the stellar atmosphere. We cannot use standard methods for solving the transfer equation to satisfy this condition, since they assume a smooth dependence of the specific intensities on μ.

Since the photon fluxes of the incident and proper (including scattered) radiation do not interact with each other [15], we calculated the mean intensity J_ν and flux H_ν in two successive steps.

(1) We found a solution of the equation for the external radiation

$$\mu\frac{dI_\nu}{dr} = \alpha_\nu(I_\nu - S_\nu), \qquad (1)$$

assuming absorption without reemission (i.e., with zero source function $S_\nu = 0$) for the mean intensity J_ν and flux H_ν in the form

$$J_\nu^+ = I_\nu^+ \exp\left(-\frac{\tau_\nu}{\mu}\right), \qquad (2)$$

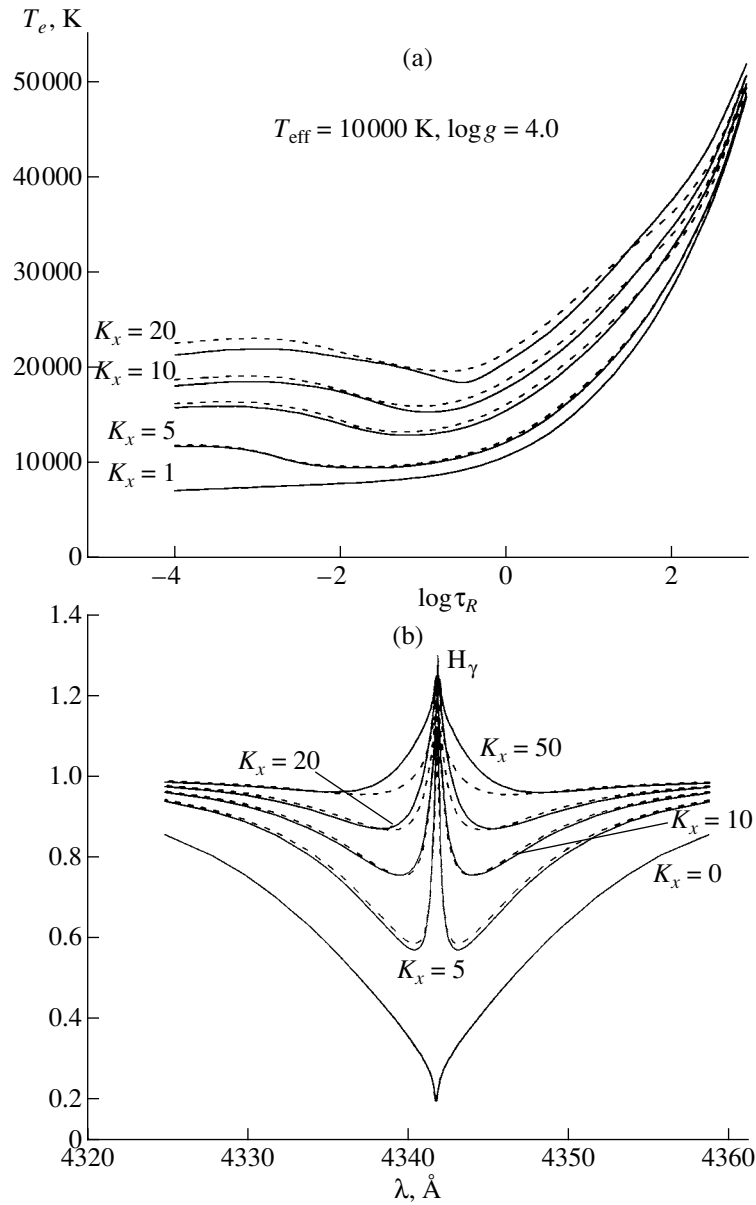$$H_\nu^+ = \mu I_\nu^+ \exp\left(-\frac{\tau_\nu}{\mu}\right), \qquad (3)$$

Fig. 2. (a) Temperature distributions and (b) profiles of the H_γ line for atmospheres with $T_{\rm eff} = 10\,000$ K, $\log g = 4.0$, and vertically incident radiation with various intensities K_x. The solid and dashed curves correspond to the cases when scattering is and is not taken into account.

where the superscript $+$ denotes external radiation, I_ν^+ is the upper boundary condition at frequency ν, and τ_ν is the optical depth. The opacity coefficient α_ν is determined as the sum of the opacities for the true absorption α'_ν and Thomson scattering σ_e.

(2) Next, we obtain a standard solution for the transfer equation using the Hermitian method [16] at three angles μ with zero upper boundary condition $I_\nu^+ = 0$ and for the source function, determined by the sum of the total scattered (including external) radia-

tion and the Planck function at the given frequency:

$$S_\nu = \frac{\sigma_e}{\alpha_\nu}(J_\nu^+ + J_\nu) + B_\nu(T). \qquad (4)$$

We did not take into consideration the effects of Comptonization. As we will show below, this approximation is valid for energies up to $h\nu = 40$ keV.

The final values of the mean intensity and flux at the current frequency of the external radiation are obtained by summing the solutions found at the two stages.

Figure 1a shows the distributions of the total fluxes with the Rosseland optical depth τ_r for the

model atmosphere with $T_{\text{eff}} = 10\,000$ K and $\log g = 4.0$ for three energies. In all these cases, we took into account the scattered component in the presence of unit vertical incident flux $I_\nu^+ = 1.0$. Taking Thomson scattering into account results in two effects: the total flux propagating into the atmosphere decreases in layers above those with optical depth $\tau_\nu = 1.0$ and substantially increases in deeper layers. These effects should obviously lead to less heating of the atmosphere in upper chromospheric layers and an increase the temperature gradient $\dfrac{dT_e}{d\tau_r}$ in deep layers.

Due to the scattering, the stellar atmospheres possess a nonzero X-ray albedo. We calculated specific albedos for various types of stellar atmospheres with solar chemical composition, presented in Fig. 1b as functions of frequency. The effect of the gravitational force on the albedo turns out to be negligible, so the albedo is determined primarily by the effective temperature of the star. Our analysis of these distributions leads us to conclude that the effect of scattering is negligible for radiation with energies up to $E_\nu = 10.0$ keV, so the atmosphere absorbs up to 90% of the incident flux. On the contrary, the albedo of atmospheres of all spectral types exceeds 50% at $E_\nu > 17.0$ keV, so scattering becomes a determining factor in the formation of the temperature distribution in the irradiated atmosphere. Note that the contribution of true absorption of radiation with $E_\nu = 40.0$ keV to heating of the atmospheric layers proves to be over twice the contribution of Compton scattering, which was estimated in a double-scattering approximation with $\Delta\lambda = 0.024$ Å. Therefore, we are able to accurately calculate the temperature structures of stellar atmospheres with energies of the incident radiation of up to $E_\nu = 40$ keV while allowing only for Thomson scattering.

Figure 2a presents temperature distributions in the model atmospheres with $T_{\text{eff}} = 10\,000$ K and $\log g = 4.0$ for the case of vertically incident external radiation $\mu = 1.0$ with various intensities $K_x = \dfrac{\mu J_x}{\sigma T_{\text{eff}}^4}$ and a spectral distribution $I_\nu^+ = \text{const } \nu^{-0.6}$ at energies $E_\nu = 1{-}40$ keV. These model atmospheres were obtained using the BINARY3 code [14] for the calculation of blanketed irradiated atmospheres with and without allowance for scattered hard radiation. If such scattering is taken into account, the heating of all layers with $\log \tau_r < 1.5$ decreases by $10{-}15\%$, while the heating of deeper layers increases by $20{-}35\%$. The strongest cooling is observed near the temperature minimum at $-1.0 < \log \tau_r < -0.5$.

Since the radiated stellar spectrum is formed primarily at depths with $\log \tau_r < 1.0$, the scattering of the external radiation results in a decrease of the radiated continuum fluxes. Our numerical calculations based on the presented temperature distributions show that, near the Paschen continuum, this flux decrease equals $6{-}9\%$ for external radiation with intensities below $K_x = 10.0$ and up to 15% for radiation with $K_x = 50.0$. The flux decrease grows monotonically in the ultraviolet, up to $25{-}30\%$ near the threshold of the Lyman continuum.

The corresponding changes in the H_γ line profile in the spectrum of an irradiated atmosphere are shown in Fig. 2b. Since most cooling takes place in regions near the temperature minimum, the absorption features are slightly strengthened (by $2{-}4\%$). On the other hand, weaker cooling of the hot chromospheric layers results in a substantial increase (by up to 50%) of the emission components. Finally, both the emission and absorption lines or their components are enhanced in the stellar spectrum when scattering of the external radiation is taken into account.

II. The previously used method for finding the terms S_2, S_3, and S_4 in the total heating function of an irradiated atmosphere [12]

$$S(\tau_v) = S_0(\tau_v) + a_2 \times S_2(\tau_v) \qquad (5)$$
$$+ \, a_3 \times S_3(\tau_v) + a_4 \times S_4(\tau_v)$$

was based on the simplifying assumptions that the source function was equal to zero in the X-ray range, $S_\nu = 0$ and that the ratio of the absorption coefficients in the X-ray and optical $\frac{\alpha_\nu}{\alpha_v}$ was constant at all depths. Obviously, taking scattering into account violates both of these assumptions. Accordingly, we redefined the terms S_2, S_3, and S_4 using the formal quadrature solutions of the transfer equation (1).

(1) We used the following expression for the term S_4, determining the work of the incident flux with optical depth:

$$S_4(\tau_v) = \int\limits_{\nu_1}^{\nu_2} \int\limits_{0}^{\tau_v} \left(S_2(\tau_v') + H_\nu^+(\tau_v') \right) d\tau_v' d\nu_x, \quad (6)$$

where the subscripts v and x refer to the proper and external radiation, respectively; $S_2(\tau_v')$ is the S_2 term, determined in the standard way [12]:

$$S_2(\tau_v') = \int\limits_{\nu_1}^{\nu_2} \frac{dH_\nu^+(\tau_v')}{d\tau_v'} d\nu_x; \qquad (7)$$

$H_\nu^+(\tau_v')$ is the total flux for an arbitrary frequency for the external radiation; and the integration is carried out over the entire energy range for the incident radiation. The component $S_2(\tau_v')$ in (6) corresponds to an additional transfer of radiation from the hot chromospheric layers to the interior of the irradiated atmosphere.
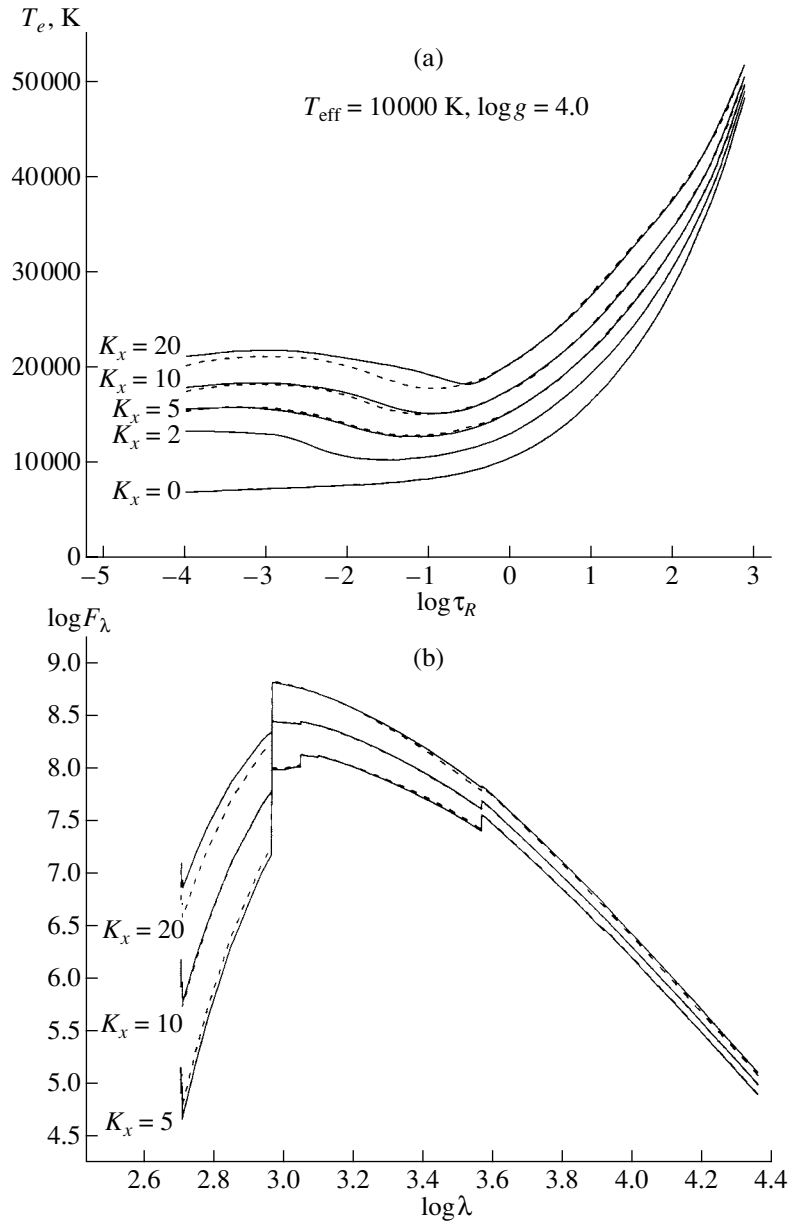
Fig. 3. (a) Temperature distributions and (b) emitted fluxes for the atmospheres with $T_{eff} = 10\,000$ K, $\log g = 4.0$, and vertically incident radiation with various intensities K_x. The solid curves correspond to the blanketed models, and the dashed curves to models with a semi-grey approximation.

(2) The corrected expression for the constant term S_3 [12]

$$S_3(\tau_v) = \int_{\nu_1}^{\nu_2} H_\nu^+(\tau_v = 1) d\nu_x \qquad (8)$$

corresponds to uniform heating of the atmosphere at depths $\log \tau_v > -0.5$ under the action of the external radiation alone, which directly reaches the region of formation of the optical continuum.

(3) Finally, we refined the approximation for the optical-absorption coefficient α_v [14] and redefined

the scaling coefficients a_2, a_3, and a_4 in (5). This was done by finding the best-fitting models for the irradiated atmospheres calculated in the semi-grey approximation using the BINARY2 code [12] and for the blanketed atmospheres using the BINARY3 code [14]. The temperature distributions derived using the two methods are shown in Fig. 3a for the model with $T_{eff} = 10\,000$ K, $\log g = 4.0$, and $\mu = 1.0$, and the corresponding continuum fluxes are presented in Fig. 3b.

As a result, we obtained the following approxima-

tion:

$$\alpha_v = \left(\alpha_r^{(5.97+0.73\times\log(\tau_r))} \times \alpha_p\right)^{\frac{1}{6.97+0.73\times\log(\tau_r)}}, \quad (9)$$

where α_r and α_p are the Rosseland and Planck absorption coefficients with the new scaling coefficients $a_2 = 0.67$, $a_3 = 0.51$, and $a_4 = 0.63$.

We can see in Fig. 3a that, in the semi-grey approximation, the refined method can be used to calculate models of irradiated atmospheres whose maximum temperature uncertainties are 3% in chromospheric and deep layers and 7% in the narrow transition region from the chromosphere to the layer of the temperature minimum. The results for various frequency distributions of the external radiation indicate that this method is suitable for calculating atmospheres for which the external radiation has intensities up to $K_x = 100$, is incident at angles $\mu \geq 0.05$, and has wavelengths 0.30 Å $\leq \lambda \leq 50.0$ Å and 250 Å $\leq \lambda \leq 3000$ Å. The corresponding errors in the emitted fluxes are below 3–8% near the Paschen and Balmer continua.

2.2. Calculation of Non-LTE Populations

We used the NONLTE3 software developed by Sakhibullin [17] to calculate the CaII level populations and line profiles, which employs the complete linearization method of Auer and Heasley [19]. We solved the transfer equations in the optical and determined the total rate matrix using existing methods. When calculating the absorption coefficient at each frequency, we allowed for all main sources of continuous absorption, about 300 000 of the strongest lines at $\lambda > 525$ Å from the lists of Kurucz [18], and the most important molecular bands according to the theory of Nersisyan *et al.* [20], which were calculated and courteously provided to us by Ya. Pavlenko (Main Astronomical Observatory, National Academy of Sciences of the Ukraine).

We modified the NONLTE3 software for the case of irradiated atmospheres. The START code was supplemented with a block of subroutines for calculating the radiation field at X-ray energies and the corresponding ionization and recombination rates for the CaII ion. We calculated the radiation field using the standard OPREN and OPRALL subroutines from the SPECTR package [13] using the method described above. We analyze here the results for three frequency dependences of the external radiation: with the X-rays specified by a power law in the range 0.5–40.0 keV and with the ultraviolet radiation described by black-body distributions with the two temperatures $T_{\rm rad} = 15\,000$ and $50\,000$ K. Since the incident and proper radiation of the star are always in different spectral ranges, we consider their transfer in

the atmosphere separately (i.e., with the source function in (1) determined only by the scattering factor).

The opacity sources at X-ray energies taken into account were the cross sections for ionization from all levels of hydrogen, helium, and the 20 other most abundant chemical elements according to the data of Kurucz [18, 21], Yakovlev *et al.* [23], and Hofsaess [22]. The level populations for these elements were calculated in an LTE approximation using the POPS and PHSAHA subroutines, taken from the ATLAS6 [24] and STARDISK [25] code. The relative contribution of CaII to the total absorption coefficient at the frequencies of the external radiation varied from 10^{-3} to 10^{-10}. Therefore, we took the radiation field at these energies to be constant and the corresponding induced transitions to be fixed. The ionization and recombination rates were determined taking into account all inner and outer shells of CaII and were directly included in the total rate matrix.

2.3. The Model Atom

We constructed a model atom including 42 energy levels of CaII and the ground state of CaIII. The data on these levels are presented in Table 1, and the corresponding Grotrian diagram is given in Fig. 4. The principal quantum number varies from $n = 3$ to $n = 10$, and the orbital quantum number, from $l = 0$ to $l = 5$ (i.e., from s to h). The fine splitting of the $3d$ and $4p$ levels was also taken into account. The importance of this splitting was demonstrated in several earlier studies [26–28]. The energy of ionization from the lowest level was taken from the data of [29]. The energies of ionization from all excited levels were calculated using wavelengths taken from the review of Kurucz [18]. The energy of ionization from the last level is $E_{\rm ion} = 0.39$ eV, so this model atom can be used for stellar atmospheres whose temperatures are no lower than 4000 K. Since the ionization potential of CaI is $E_{\rm ion} = 6.11$ eV, the fraction of calcium atoms in this state in the atmospheres of such stars does not exceed 10% and, as was shown in [4], cannot appreciably affect the populations in the main ionization state.

The CaII model involves 291 bound–bound and 42 bound–free radiative transitions, 80 of which were taken to be linearized.

We adopted the basic set of oscillator strengths for the bound–bound transitions from the results of the calculations of Seaton *et al.* [30], carried out using the tight-bond method, which are presented in the TOPBASE database. Their comparison of their results with the oscillator strengths given in several other studies [18, 29, 31–33, 40] indicates that, for all the strongest transitions between low levels, the differences between the various data are less than 10%.

Table 1. Data on the CaII levels: the ionization energy E_{ion} (eV), statistical weight g, lifetime τ (s), and parameters approximating the ionization cross section σ_0, α, and s

No.	T	g	E_{ion}	$\log \tau$	α	$\log \sigma_0$	s	No.	T	g	E_{ion}	α	$\log \sigma_0$	s
1	4s	2	11.721	∞	49.3	-21.77	3.019	23	8p	6	1.116	0.56	-17.13	3.186
2	3d	4	10.029	∞	10.0	-18.97	2.281	24	7f	14	0.968	1.94	-16.61	3.746
3	3d	6	10.021	∞	10.0	-18.97	2.281	25	7g	18	0.691	1.60	-16.35	4.825
4	4p	2	8.597	-8.16	137.	-21.83	3.076	26	7h	22	0.960	1.60	-16.35	4.825
5	4p	4	8.570	-8.16	137.	-21.83	3.076	27	9s	2	0.901	242.	-23.90	3.004
6	5s	2	5.252	-8.43	24.4	-21.55	3.039	28	8d	10	0.851	142.	-23.07	4.773
7	4d	10	4.672	-8.54	29.0	-20.54	3.033	29	9p	6	0.803	2.47	-16.98	3.122
8	5p	6	4.212	-7.44	16.2	-19.55	3.202	30	8f	14	0.705	1.83	-16.41	3.640
9	4f	14	3.283	-8.54	5.23	-18.54	4.186	31	8g	18	0.700	1.51	-16.07	4.644
10	6s	2	2.956	-8.23	13.8	-21.08	3.070	32	8h	22	0.699	1.51	-16.07	4.644
11	5d	10	2.702	-8.22	10.8	-20.11	3.090	33	10s	2	0.659	273.	-24.11	3.004
12	6p	6	2.484		3.25	-17.71	3.332	34	9d	10	0.625	143.	-22.46	6.169
13	5f	14	2.046		2.62	-17.38	4.029	35	10p	6	0.592	2.39	-16.98	3.073
14	5g	18	2.029	-7.85	2.17	-17.50	5.345	36	9f	14	0.525	2.25	-16.67	3.308
15	7s	2	1.870		196.	-23.54	3.005	37	9g	18	0.521	1.55	-16.02	4.369
16	6d	10	1.737		216.	-23.59	3.005	38	9h	22	0.521	1.55	-16.02	4.369
17	7p	6	1.616		2.72	-17.33	3.266	39	10d	10	0.468	91.5	-21.71	6.067
18	6f	14	1.373		2.13	-16.89	3.883	40	10f	14	0.396	2.54	-16.71	3.113
19	6g	18	1.363	-7.62	1.77	-16.77	5.053	41	10g	18	0.393	1.55	-16.02	4.369
20	6h	22	1.361		1.77	-16.77	5.053	42	10h	22	0.393	1.55	-16.02	4.369
21	8s	2	1.268		180.	-23.54	3.006	43	con	1				
22	7d	10	1.119		185.	-23.94	3.035							

The discrepancies in f_{ij} for moderately weak lines associated with low levels can reach 50%. Finally, the uncertainties in the oscillator strengths can be as large as one to two orders of magnitude only in very rare cases for the least important lines. Therefore, we carried out test calculations for model atmospheres with $T_{eff} = 6000$ K, $10\,000$ K, $\log g = 4.0$, and $[A] = 0.0$ using the oscillator strengths presented in [30] and [18]. These calculations showed the differences in the level populations to be quite small (below 3%). On the other hand, the populations of the CaII levels in the upper layers of the atmosphere obtained using the f_{ij} from [40] differ by 10% for the $4f$ level and up to 40% for the $5p$ and $6p$ levels. However, the discrepancies in the equivalent widths for most of the observed lines do not exceed 0.03% in all three versions of the calculations and can be neglected. The only exceptions are the $\lambda = 11\,839$ Å, $11\,949$ Å lines

of the $5s-5p$ transition, for which the equivalent-width discrepancies vary from 0.05% for dwarfs with $\log g = 4.0-4.5$ to 0.25% for supergiants with $\log g = 0.0$.

We also used the data of Seaton *et al.* [30] for the cross sections for photoionization from all levels. These were approximated by the formula

$$\sigma = \sigma_0 \left(\frac{\lambda}{\lambda_0} - \alpha \right)^2 \lambda^s, \qquad (10)$$

where σ is the ionization cross section, λ and λ_0 the current and threshold wavelengths, and α, σ_0, and s the approximation coefficients, presented in Table 1. The approximation errors for most of the cross sections are below 10%. Exceptions are the $4p$ level, for which this error is 18%, and highly-excited d levels, for which the errors are $20-45\%$. We compared the cross sections used with those given by Hofsaess [22] and, for the $4s$ level, with the data
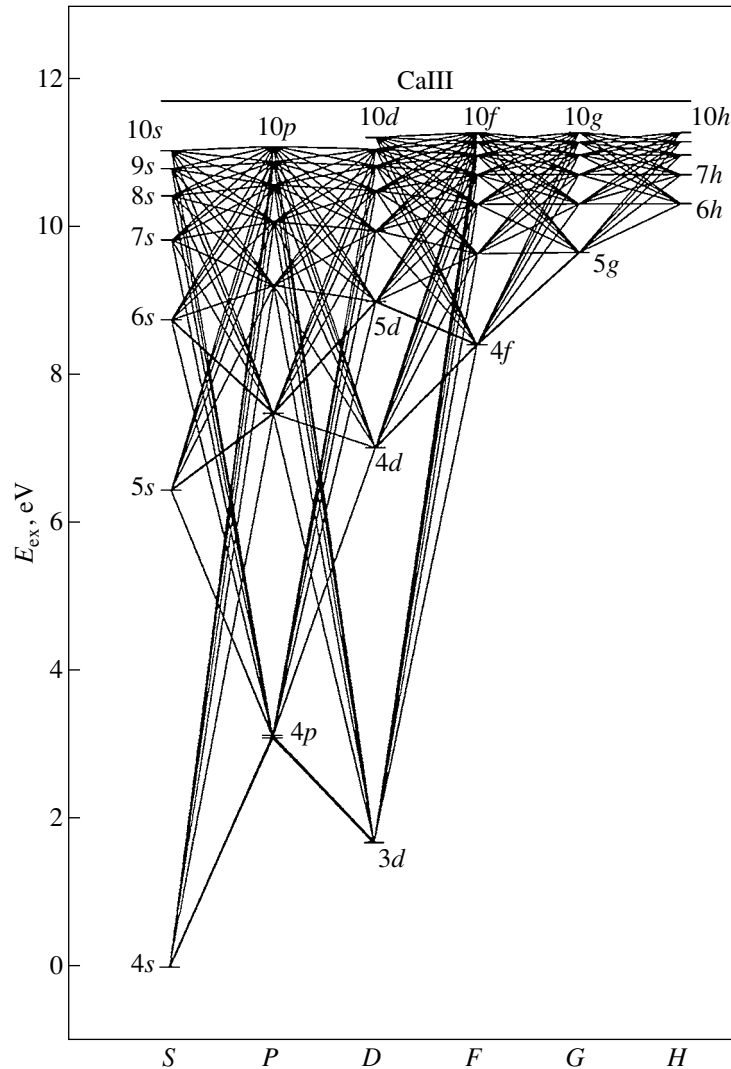
Fig. 4. The model of the CaII atom.

of Yakovlev *et al.* [23]. Substantial differences (up to 70%) were revealed only for the 4s level. Therefore, we carried out test calculations using the data for σ for the 4s level of [22] and [23], which were in the worst agreement. These showed that the indicated discrepancies do not appreciably affect the level population ($\Delta n_{\mathrm{nonLTE}} < 0.1\%$), since the cross section for ionization from this level is relatively small: $\sigma_0 = 0.39$ Mb. The errors in σ for most of the other states do not exceed 10%, except for the highly-excited d levels, for which they vary from 30 to 290%.

We calculated the collision rates for bound–bound transitions due to collisions with free electrons using several approximations:

(1) the data of Vainshtein *et al.* [34] for all transitions whose parameters are listed there;

(2) the formula of Regemorter [35] for other allowed transitions;

(3) the approximation $\Omega = 1$ [36] for other forbidden transitions.

The collision rates for free–bound transitions were determined using the formula of Lotz [37].

In addition, we took into account inelastic collisions with atoms of neutral hydrogen using the formula from [38] with the scaling coefficients $k_H = 0.0, 0.1$, and 1.0.

The formulas we have used do not take into consideration the specific properties of the CaII ion, so errors in calculating the collision rates may reach 50%, even for the main transitions. To estimate the influence of these errors on the CaII line profiles, we carried out calculations using the alternative set of rates of Burgess *et al.* [39, 40] for all transitions between the first 10 levels. Our comparison of the calculations using these two sets of collision rates showed that the largest equivalent-width differences for the atmospheres of solar-type stars ($T_{\mathrm{eff}} =$

5500−6000, $\log g = 4.0$, $[A] = 0.0$) occur for the lines of the $\lambda = 8498, 8542, 8662$ Å triplet (up to 1.5%) and the $\lambda = 8912, 8927$ Å doublet (up to 2%). The errors in the equivalent widths are negligible (below 1%) for model atmospheres with low metallicity ($[A] \leq -1.0$) or surface gravity $\log g \leq 3.0$. However, the chosen set of collision rates strongly influence the profiles and equivalent widths of the $\lambda = 8498, 8542, 8662$ Å triplet in calculations with the model solar atmosphere including the chromosphere (see Section 4). Figure 5c shows that using the rates of Burgess *et al.* [40] results in a substantial decrease in the absorption core of the $\lambda = 8542$ Å line, in contradiction to observations. Therefore, we concluded that the approximation of [40] overestimates the collision rates, at least for the $3d$−$4p$ transitions, and we did not use this approximation in subsequent calculations.

We calculated the rates of ionization and recombination by external radiation using the cross sections presented in [23]. We allowed for additional ionization from the corresponding outer shells for the low $4s$, $3d$, and $4p$ states. The ionization thresholds for more highly excited levels are at $\lambda > 2200$ Å, where the role of external radiation is small and was not taken into account. We assumed that any ionization channel for the CaII ion brings it to the next ionization state, CaIII. The effect of shaking off electrons and the Auger effect were not taken into account, due to the small influence of processes occurring at subsequent states (below 1%) on the populations in the main ionization state [4].

When modeling the theoretical profiles and equivalent widths of the CaII lines, we allowed for Doppler broadening by thermal motion and microturbulence ξ_{turb}, natural damping (with constants derived from the set of oscillator strengths used), Stark broadening (with the coefficients C_4 of [41, 42]), and van der Waals broadening calculated using the formula of Gray [43]. As shown in several earlier papers [27, 28, 46], the C_6(Uns) values obtained from the classical estimate of Unsold [43] are underestimated by one-half to two orders of magnitude. Therefore, we adopted the constants C_6 for the lines of the $\lambda = 3933, 3968$ Å resonant doublet and $\lambda = 8498, 8542, 8662$ Å infrared triplet in accordance with the data of Barklem and O'Mara [47], Smith and Drake [48], and Chmielewski [5]. The values of C_6(prof) for other lines were determined by analyzing the lines in the solar spectrum. The method used to derive the C_6(prof) will be described below. We used the value $\xi_{turb} = 2.0$ km/s in all calculations of line profiles in the irradiated atmospheres, while $\xi_{turb} = 1.2$ km/s was adopted in our analysis for the solar spectrum. When modeling the line profiles in the solar spectrum, we also took into account additional line-broadening mechanisms: the rotational velocity $V \sin(i) = 1.9$ km/s, instrumental profile, and macroturbulence V_{macr}, whose values were determined for each line individually.

We calculated the equilibrium states of CaII in the irradiated atmospheres for the solar abundance $\log \varepsilon(\text{Ca}) = 6.32$, taken from [49]. When analyzing the solar spectrum, we chose the abundance for each line individually to obtain a good agreement between the observational and theoretical data.

3. ANALYSIS OF CaII LINES IN THE SOLAR SPECTRUM

The most trustworthy way to verify non-LTE calculations is to model as completely as possible a set of lines for the element in question using a high-resolution spectrum of a star whose atmospheric parameters are well known. It is virtually impossible to perform such checks for irradiated atmospheres of stars in close binary systems, since the observed spectra do not possess the required quality and the theoretical modeling requires a large number of uncertain parameters. In addition, verifying our non-LTE method for the calculation of CaII lines using stars without irradiated atmospheres is interesting in its own right, from the viewpoint of subsequent applications in analyses of the spectra of single stars.

Accordingly, we used the spectrographic Solar Atlas [50], which presents data on the total fluxes at wavelengths $\Delta\lambda = 2960−13\,000$ Å with signal-to-noise ratios of 2000−9000 and a resolution of $\dfrac{\lambda}{\Delta\lambda} = 522\,000$. We consider the Sun to be the optimum test object: although CaII is the main ionization state in the solar atmosphere and does not appreciably deviate from LTE, the high-quality data of this atlas can enable us to study profiles of the maximum number of lines. Moreover, the profiles of the resonant doublet and infrared triplet of CaII in the solar spectrum show effects due to chromospheric layers, so we can analyze the accuracy of our calculations of non-LTE populations in these layers.

We performed the non-LTE calculations using combined models for the solar atmosphere derived from the models of [18] and [52] (which we will call the Kur + Val model) and the models of [51] and [52] (which we will call the HM + Val model) joined in the region of the temperature minimum.

A set of 16 lines without significant blending in the cores and one of the wings was chosen for our analysis. This enabled the simultaneous derivation of the
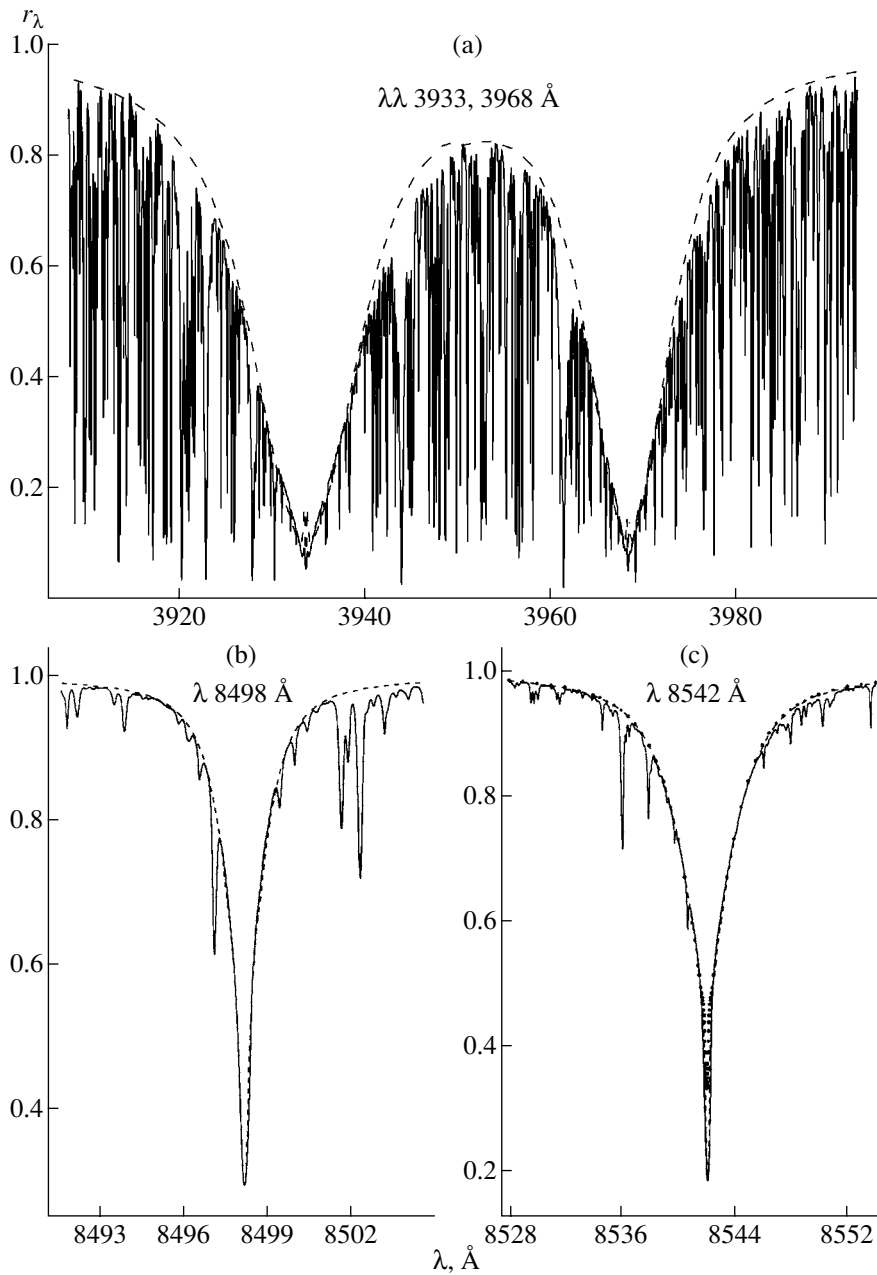
Fig. 5. Observed (solid curves) and theoretical (dashed curves) profiles of the (a) λ 3933, 3968, (b) 8498, and (c) 8542 Å lines in the solar spectrum. The dashed curve for the λ 8542 Å line was calculated using the collision rates of Burgess *et al.* [40].

calcium abundance, van der Waals broadening constant C_6(prof), and macroturbulence velocity V_{macr}. The equivalent widths of the corresponding lines were obtained using several methods (direct integration of the profile and half-profile, approximation using Gaussian or Lorentzian curves, and a convolution of several such curves, followed by a determination of the areas for individual components). A complete set of information on the CaII lines studied is presented in Table 2, and the transitions corresponding to these lines are shown by the thick lines in Fig. 4.

Our analysis of the CaII lines was based primarily on fitting the observed and theoretical non-LTE profiles using the method described in [27]. We attempted to achieve a maximum agreement between the abundances derived from strong lines (corresponding to transitions between the low-excitation $4s$, $4p$, and $3d$ levels) and weak lines.

Figures 5 and 6 show the theoretical and observed profiles of a number of lines; the non-LTE and LTE

Table 2. Studied lines of CaII: transitions; oscillator strengths f_{ij}; constants for natural damping γ_R, Stark broadening C_4, and van der Waals broadening C_6(Uns); equivalent widths W_λ; and corrections to the Unsold constants $\Delta \log(C_6) = \log(C_6(\text{prof})) - \log(C_6(\text{Uns}))$ for the model Kur + Val.

λ, Å	Transition	f_{ij}	$\log \gamma_R$	$\log C_4$	$\log C_6(Uns)$	W_λ, mÅ	$\Delta \log(C_6)$
3933.682	$4s^2 S_{1/2} - 4p^2 P^0_{3/2}$	0.663	8.154	-13.80	-32.34		0.32
3968.486	$4s^2 S_{1/2} - 4p^2 P^0_{1/2}$	0.332	8.154	-13.80	-32.34		0.32
8662.167	$3d^2 D_{3/2} - 4p^2 P^0_{1/2}$	0.0473	8.187	-13.65	-32.03	2600 ± 90	0.57
8542.125	$3d^2 D_{5/2} - 4p^2 P^0_{3/2}$	0.0574	8.187	-13.65	-32.03	3250 ± 50	0.49
8498.040	$3d^2 D_{3/2} - 4p^2 P^0_{3/2}$	0.0096	8.187	-13.65	-32.03	1050 ± 50	0.57
11949.77	$5s^2 S_{1/2} - 5p^2 P^0_{1/2}$	0.504	8.474	-13.34	-31.74	170 ± 10	1.43
11839.01	$5s^2 S_{1/2} - 5p^2 P^0_{3/2}$	0.998	8.474	-13.34	-31.74	210 ± 20	1.52
9931.374	$5p^2 P^0_{3/2} - 6s^2 S_{1/2}$	0.295	8.292		-31.11	43 ± 3	1.89
9854.734	$5p^2 P^0_{1/2} - 6s^2 S_{1/2}$	0.296	8.292		-31.11	35 ± 2	1.89
8201.723	$5p^2 P^0_{1/2} - 4d^2 D_{3/2}$	0.890	8.287		-31.13	45 ± 1	1.86
8248.812	$5p^2 P^0_{3/2} - 4d^2 D_{5/2}$	0.900	8.287		-31.13	65 ± 2	1.78
8254.725	$5p^2 P^0_{3/2} - 4d^2 D_{3/2}$	0.104	8.287		-31.13	20 ± 2	1.83
9890.630	$4f^2 F^0_{5/2,7/2} - 5g^2 G_{7/2,9/2}$	0.134	8.620		-31.01	71 ± 3	1.90
6456.875	$4f^2 F^0_{5/2,7/2} - 6g^2 G_{7/2,9/2}$	0.184	8.588		-30.40	16.5 ± 2	1.58
8927.391	$4d^2 D_{5/2} - 4f^2 F^0_{5/2,7/2}$	1.080	8.839	-13.26	-31.59	127 ± 2	1.19
8912.096	$4d^2 D_{3/2} - 4f^2 F^0_{5/2,7/2}$	1.080	8.839	-13.26	-31.59	113 ± 1	1.37

abundances derived from our analysis of the profiles and equivalent widths are given in Table 3.

Varying the microturbulence velocity in the range $\xi_{\text{turb}} = 1.0 - 1.4$ km/s leads to changes in the calcium abundances derived using different lines that do not exceed $\Delta \log \varepsilon(\text{Ca}) = 0.009$ dex; the sum over all lines varies by $\Delta \log \varepsilon(\text{Ca}) = 0.002$ dex at constant dispersion. The corresponding differences in the empirical constants $C_6(\text{prof})$ are below 15% for the $\lambda = 6456, 8201, 8254$ Å lines and considerably less for all remaining lines. Therefore, the CaII profile analyses do not depend on the adopted microturbulence velocity, which we fixed at the value $\xi_{\text{turb}} = 1.2$ km/s.

The value of the scaling coefficient $k_H = 0.1$ was established by requiring that the abundances derived from the $\lambda = 11\,949, 11\,839$ Å lines agree with the mean abundance. Table 3 shows that these lines are very sensitive to variations in k_H, even if the equivalent widths are used, and are the most efficient lines to use when determining this quantity. After fixing the value of k_H, we varied the calcium abundance, $C_6(\text{prof})$, and macroturbulence velocity V_{macr} to obtain the best fit between the observed and theoretical non-LTE profiles. This analysis led to the following conclusions.

(1) Adequate reproduction of the observed triplet line profiles is difficult when using a single value for V_{macr}, since the higher values $V_{\text{macr}} = 4-5$ km/s are necessary to fit the line cores, while the modeling of the wings requires $V_{\text{macr}} = 0.0-1.5$ km/s, characteristic of all weak lines.

(2) The wings of the theoretical profiles of the $\lambda = 8498, 8542, 8662$ Å lines obtained using the C_6 values from [47, 5] agree well with the observed profiles. This is also true of the lines of the $\lambda = 3933, 3968$ Å doublet. Unfortunately, the presence of multiple strong blends in this wavelength range results in substantial uncertainties in C_6. The analysis for the profiles of weak lines confirms the data of several previous studies [27, 28, 45] that indicate an increase in the corrections for the Unsold constants $\Delta \log(C_6) = \log C_6(\text{prof}) - \log C_6(\text{Uns})$ as the excitation energy of the lower and upper levels of the corresponding transitions increases. For example, the corrections were $\Delta \log(C_6) \approx 0.5$ for strong lines of CaII, $\Delta \log(C_6) = 1.2-1.5$ for lines of the $5s-5p$ and $4d-5p$ transitions, and, on average, $\Delta \log(C_6) \approx 1.85$ for other lines.

(3) The empirical constants $C_6(\text{prof})$ obtained in the calculations with the HM + Val model are
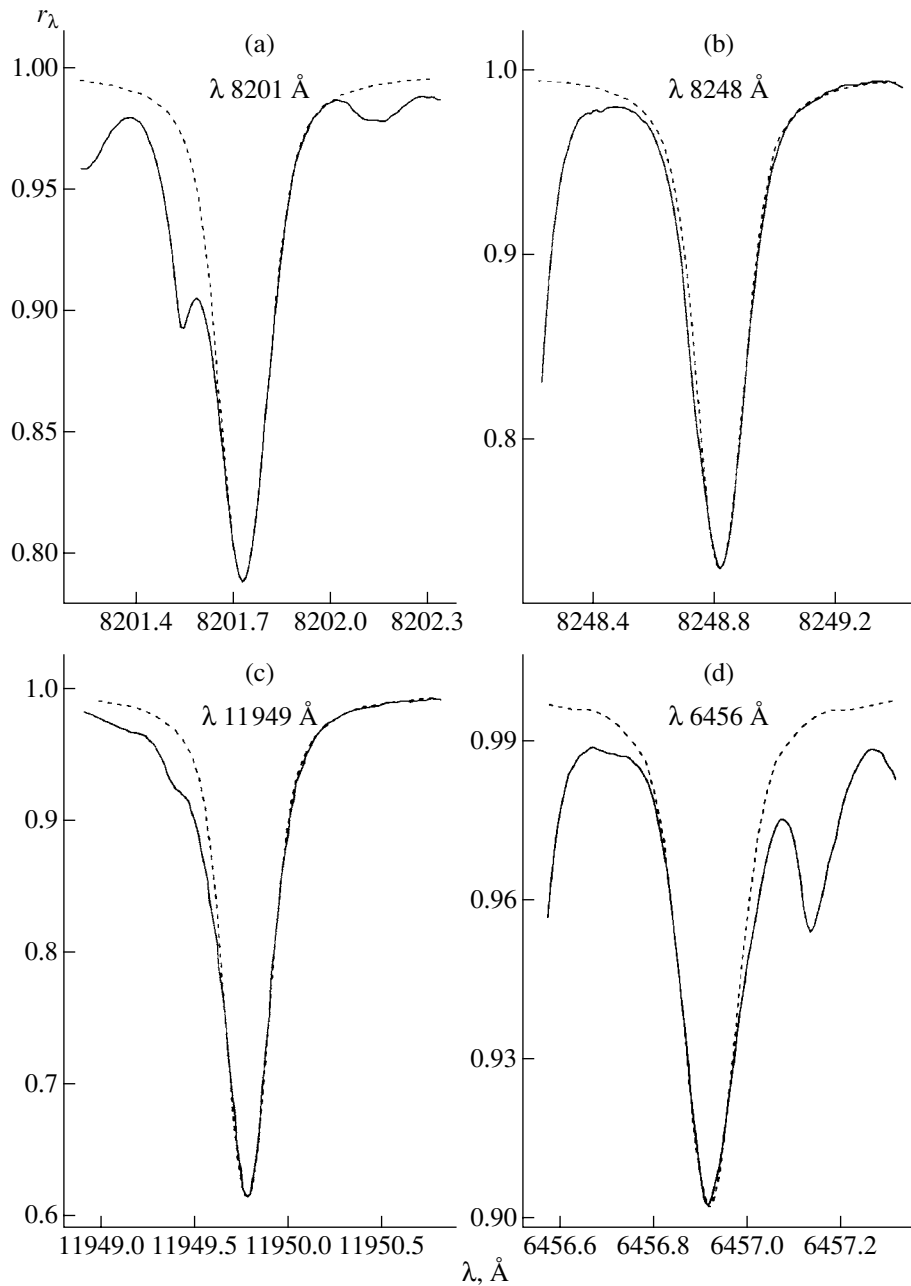
Fig. 6. Observed (solid curves) and theoretical (dashed curves) profiles of the (a) λ8201, (b) 8248, (c) 11 949, and (d) 6456 Å lines in the solar spectrum.

slightly greater than the values used in the Kur + Val model. This increase was 20 to 40% for lines of the $\lambda = 8498, 8542, 8662$ Å triplet and was less than 7% for all weak lines. Therefore, the presented values of C_6(prof) are suitable for calculating the lines of CaII for various model atmospheres.

(4) The non-LTE corrections $\Delta \log \varepsilon$ to the abundances of most of the CaII lines are appreciable, even in the solar atmosphere. A comparison of the data in Tables 2 and 3 shows that the non-LTE corrections

are $\Delta \log \varepsilon = 0.10 - 0.15$ dex for lines with equivalent widths $W_\lambda > 100$ mÅ and, on average, $\Delta \log \varepsilon = 0.06$ dex for weaker lines. Finally, the correction for the effects of deviations from LTE to the abundance derived using all lines of CaII is $\Delta \log \varepsilon = 0.08$ dex and should be taken into account in analyses of the solar spectrum.

(5) The individual calcium abundances derived from the profiles of CaII lines for the HM + Val model are lower than those for the Kur + Val model by

Table 3. Calcium abundance from CaII lines in the solar spectrum

λ, Å	HM + Val	Kur + Val				
	$\log\varepsilon$(profile)	$\log\varepsilon(W_\lambda)$				
		non–LTE				LTE
	$k_H = 0.1$	$k_H = 0.1$	$k_H = 0.0$	$k_H = 0.1$	$k_H = 1.0$	
3933.682	6.320	6.320				
3968.486	6.320	6.320				
8662.167	6.298	6.284	6.294	6.294	6.296	6.385
8542.125	6.269	6.307	6.285	6.288	6.289	6.369
8498.040	6.249	6.311	6.168	6.172	6.173	6.307
11949.77	6.269	6.260	6.346	6.370	6.410	6.458
11839.01	6.394	6.399	6.310	6.339	6.387	6.453
9931.374	6.284	6.307	6.232	6.234	6.256	6.287
9854.734	6.341	6.363	6.462	6.463	6.487	6.521
8201.723	6.324	6.337	6.264	6.264	6.286	6.319
8248.812	6.206	6.223	6.182	6.182	6.205	6.241
8254.725	6.357	6.377	6.385	6.385	6.399	6.417
9890.630	6.223	6.252	6.185	6.210	6.243	6.261
6456.875	6.383	6.403	6.344	6.349	6.359	6.362
8927.391	6.218	6.228	6.171	6.190	6.243	6.340
8912.096	6.234	6.244	6.222	6.240	6.290	6.372
Mean	6.293	6.307	6.275	6.284	6.309	6.364
σ	0.059	0.059	0.089	0.087	0.088	0.080

0.01−0.02 dex. Therefore, the differences between the mean calcium abundances derived from CaII lines in the HM + Val and Kur + Val model atmospheres are below 0.02 dex, i.e., a factor of three to four less than the differences found earlier for the KI [27], MgI [28], and NaI atoms [44]. The dispersion of the abundances for the two model atmospheres is about 0.06 dex, and the mean abundances derived from groups of strong and weak lines are in agreement.

(6) The mean calcium abundance obtained by modeling the line profiles is 0.02 dex lower than that calculated using the equivalent widths. However, Table 3 shows that the differences in the abundances for particular lines vary from 0.05 dex to 0.15 dex. These differences are due to errors in the equivalent widths associated with uncertainties in defining their wings in the presence of blending features. In general, we did not find CaII lines that enabled us to obtain calcium abundances with an accuracy better than

0.05 dex using the equivalent widths, and recommend profile modeling to determine $\log \varepsilon(\mathrm{Ca})$.

The final mean abundance established using all the calculation results is $\log \varepsilon(\mathrm{Ca}) = 6.31 \pm 0.05$, which corresponds very well to the meteoritic abundance $\log \varepsilon(\mathrm{Ca}) = 6.32 \pm 0.03$ [49]. The analyses of the profiles of the resonant doublet and infrared triplet using the Holweger–Muller model [51] by Smith and Drake [48] and Chmielewski [5] led to the values $\log \varepsilon(\mathrm{Ca}) = 6.36 \pm 0.03$ and $\log \varepsilon(\mathrm{Ca}) = 6.37 \pm 0.01$, respectively.

4. CONCLUSION

We have developed and tested a method for calculating deviations from LTE for the level populations and profiles of spectral lines of CaII in stellar atmospheres with and without external radiation. The modeling procedure includes the following.

(1) A method for calculating model atmospheres with external radiation in the ranges $0.30 \text{ Å} \leq \lambda \leq 50.0 \text{ Å}$ and $250 \text{ Å} \leq \lambda \leq 3000 \text{ Å}$. This method was implemented in the BINARY2 package and enabled us to derive model atmospheres for which the uncertainties in the radiated fluxes are usually about 3% and reach 8% only in exceptional cases.

(2) A method for calculating deviations from LTE in irradiated stellar atmospheres, with exact solution of the transfer and statistical-equilibrium equations for the atom in question. Our very general numerical code for this method was based on the NONLTE3 package and makes it possible to easily adapt existing model atoms for calculations of irradiated atmospheres.

(3) A model for the CaII atom taking into account all radiative and collisional processes occurring in normal and irradiated atmospheres. We using this model atom to analyze the CaII lines in the solar spectrum. The observed and theoretical profiles can be brought into good agreement for the entire set of lines considered using approximately the same calcium abundances. This has enabled us to refine some uncertain atomic parameters and to obtain the mean solar abundance $\log \varepsilon(Ca) = 6.31$, which is close to the meteoritic value [49].

Thus, the developed method is fully ready and can be used for studies of deviations from LTE of lines of the CaII ion in various types of stellar atmospheres.

ACKNOWLEDGMENTS

REFERENCES

1. L. Anderson, Astrophys. J. **244**, 555 (1981).
2. D. Proga, S. J. Kenyon, J. C. Raymond, and J. Micolaewska, Astrophys. J. **471**, 930 (1996).
3. A. S. Mitshevich and V. V. Tsymbal, Astron. Astrophys. **260**, 303 (1992).
4. N. A. Sakhibullin and V. V. Shimanskiĭ, Pis'ma Astron. Zh. **26**, 369 (2000) [Astron. Lett. **26**, 309 (2000)].
5. Y. Chmielewski, Astron. Astrophys. **353**, 666 (2000).
6. J. G. Doyle, G. H. J. van den Oord, E. O'Shea, and D. Banerjee, Astron. Astrophys. **347**, 335 (1999).
7. P. Judge, M. W. Carlson, and K. Wilhelm, Astrophys. J. Lett. **490**, L195 (1997).
8. M. Cuntz, W. Rammacher, P. Ulmschneider, *et al.*, Astrophys. J. **522**, 1053 (1999).
9. S. V. Berdyugina, I. Ilym, and I. Tuominen, Astron. Astrophys. **349**, 863 (1999).
10. S. V. Mallik, Astron. Astrophys. **338**, 623 (1998).
11. G. H. Smith and C. W. Churchill, Mon. Not. R. Astron. Soc. **297**, 388 (1998).
12. N. A. Sakhibullin and V. V. Shimanskiĭ, Astron. Zh. **73**, 73 (1996) [Astron. Rep. **40**, 62 (1996)].
13. N. A. Sakhibullin and V. V. Shimanskiĭ, Astron. Zh. **74**, 432 (1997) [Astron. Rep. **41**, 378 (1997)].
14. N. A. Sakhibullin and V. V. Shimanskiĭ, Astron. Zh. **73**, 793 (1996) [Astron. Rep. **40**, 723 (1996)].
15. V. A. Ambartsumyan, E. R. Mustel', A. B. Severnyĭ, and V. A. Sobolev, *Theoretical Astrophysics* [in Russian] (Gostekhizdat, Moscow, 1952).
16. L. H. Auer, J. Quant. Spectrosc. Radiat. Transf. **16**, 931 (1976).
17. N. A. Sakhibullin, Tr. Kazan. Gop. Astron. Obs. **4S**, 9 (1983).
18. R. L. Kurucz, SAO CD-ROMs (Smithsonian Astrophysical Observatory, Cambridge, 1994).
19. L. H. Auer and J. Heasley, Astrophys. J. **205**, 165 (1976).
20. S. E. Nersisyan, A. V. Shavrina, and A. A. Yaremchuk, Astrofizika **30**, 247 (1989).
21. R. L. Kurucz, SAO Spec. Rep. **309**, 1 (1970).
22. D. Hofsaess, At. Data Nucl. Data Tables **24**, 285 (1979).
23. D. G. Yakovlev, L. M. Band, M. B. Trzhaskovskaya, and D. A. Verner, Astron. Astrophys. **237**, 267 (1990).
24. R. L. Kurucz, Astrophys. J., Suppl. Ser. **40**, 1 (1979).
25. V. F. Suleymanov, Astron. Astrophys. Trans. **2**, 197 (1992).
26. J. H. Bruls, R. J. Rutten, and N. Shchukina, Astron. Astrophys. **265**, 237 (1992).
27. D. V. Ivanova and V. V. Shimanskiĭ, Astron. Zh. **77**, 432 (2000) [Astron. Rep. **44**, 376 (2000)].
28. N. N. Shimanskaya, L. I. Mashonkina, and N. A. Sakhibullin, Astron. Zh. **77**, 599 (2000) [Astron. Rep. **44**, 530 (2000)].
29. A. A. Radtsig and B. M. Smirnov, *Reference Data on Atoms, Molecules, and Ions* (Energoatomizdat, Moscow, 1986; Springer-Verlag, Berlin, 1985).
30. M. J. Seaton, C. J. Zeippen, J. A. Tully, *et al.*, Rev. Mex. Astron. Astrofis. **23**, 19 (1992).

31. W. L. Wiese and M. W. Smith, *Atomic Transition Probabilities* (National Bureau of Standards, Washington, 1969), Vol. 2, NSRDS−NBS Ref. Data Ser. 22.

32. B. Warner, Mon. Not. R. Astron. Soc. **139**, 115 (1968).

33. J. H. Black, J. C. Weisheit, and E. Laviana, Astrophys. J. **177**, 567 (1972).

34. I. I. Sobelman, L. A. Vainshtein, and E. A. Yukov, *Excitation of Atoms and Broadening of Spectral Lines* (Nauka, Moscow, 1979; Springer-Verlag, Berlin, 1981).

35. H. van Regemorter, Astrophys. J. **132**, 906 (1962).

36. J. I. Castor and H. Nussbaumer, Mon. Not. R. Astron. Soc. **155**, 293 (1972).

37. W. Lotz, Z. Phys. **232**, 101 (1970).

38. W. Steenbock and H. Holweger, Astron. Astrophys. **130**, 319 (1984).

39. A. Burgess and J. A. Tully, Astron. Astrophys. **254**, 436 (1992).

40. A. Burgess, M. C. Chidichimo, and J. A. Tully, Astron. Astrophys. **300**, 627 (1995).

41. J. Chapelle and S. Sahal-Brechot, Astron. Astrophys. **6**, 415 (1970).

42. R. A. Shine and J. L. Linsky, Sol. Phys. **39**, 19 (1974).

43. A. Unsold, *Physik der Sternatmospheren* (Springer-Verlag, Berlin, 1955, 2nd ed.).

44. Y. Takeda, Publ. Astron. Soc. Jpn. **47**, 463 (1995).

45. D. Baumuller, K. Butler, and T. Gehren, Astron. Astrophys. **338**, 637 (1998).

46. G. Zhao, K. Butler, and T. Gehren, Astron. Astrophys. **333**, 219 (1998).

47. P. S. Barklem and B. J. O'Mara, Mon. Not. R. Astron. Soc. **300**, 863 (1998).

48. G. H. Smith and J. J. Drake, Mon. Not. R. Astron. Soc. **231**, 115 (1988).

49. E. Anders and N. Grevesse, Geochim. Cosmochim. Acta **53**, 197 (1989).

50. R. L. Kurucz, I. Furenlid, J. Brault, and L. Testerman, *Solar Flux Atlas from 296 to 1300 nm* (National Solar Observatory, Sunspot, New Mexico, 1984).

51. H. Holweger and E. Muller, Sol. Phys. **39**, 19 (1974).

52. P. Maltby, E. H. Avrett, M. Carlsson, *et al.*, Astrophys. J. **306**, 284 (1986).

Translated by Yu. Dumin

The Spectrum of EG UMa

V. V. Shimanskiĭ[1] and N. V. Borisov[2]

[1]Kazan State University, Kazan, Russia

[2]Special Astrophysical Observatory, Russian Academy of Sciences,
Nizhniĭ Arkhyz, Stavropol'skiĭ kraĭ, 357147 Russia
Received November 22, 2000; in final form November 23, 2001

Abstract—Spectra and radial-velocity curves for the precataclysmic variable EG UMa are analyzed. The system ephemeris has been improved and all system parameters determined. The parameters of the secondary are consistent with current evolutionary models for single main-sequence M stars with atmospheric metallicities exceeding the solar value by 0.5 dex. We have verified that the rotational velocity of the red dwarf exceeds the velocity corresponding to synchronous orbital motion by a factor of two to three. This suggests that the efficiency of tidal interactions between the components in the synchronization of their motion is low. The observed Ca II emission lines display reflection effects in a number of uniform spectra of EG UMa obtained during the quiescent state of the secondary. © *2002 MAIK "Nauka/Interperiodica".*

1. INTRODUCTION

EG UMa ≡ Case 1 is one of the oldest and best studied close binaries belonging to the class of precataclysmic variables [1]. Case 1 was detected by Stephenson [2] in the course of a search for white dwarfs in the area of the Ursa Majoris cluster. Greenstein [3] detected emission lines in its spectra, providing evidence for the presence of a close dM2 red dwarf [4]. The orbital period of the system ($0^{d}667651$) was determined by Lanning [5] based on radial velocities derived from the H_{α} emission lines. Photometric observations of the star at phases close to $\varphi = 0.00$ showed an absence of eclipses with brightness decreases exceeding 3% [5]. A more complete study of the radial-velocity curves was carried out by Stauffer [6], who determined the amplitudes of the radial velocities for both components and estimated their masses. In their analysis of IUE ultraviolet spectra of the system at $\Delta\lambda = 1200-3000$ Å, Sion *et al.* [7] found that the atmospheric temperature of the primary is close to $T_{\rm eff} = 13\,000$ K. As a consequence, they concluded that EG Uma had the same origin as other close detached binaries that have undergone a common-envelope stage [8], but differs in the low temperature of the white dwarf. A refined estimate of the spectral type of the red dwarf based on JHK photometry and computer simulations yielded dM(4– 4.5) [9, 10].

Thus, in accordance with the results of studies carried out in the 1980s, EG UMa was classified [1, 11] as a classical precataclysmic variable with a lifetime exceeding 3×10^8 yr [7]. However, analyses of

physical processes in the system faced certain fundamental problems. Although the presence of the low-brightness white dwarf suggested that reflection effects were insignificant in the total radiation of the star, its spectra displayed strong emission lines of hydrogen (up to and including H_{10}) and ionized calcium ($\lambda\lambda 3933, 3968$ Å). Stauffer [6] found that the average equivalent width for the CaII $\lambda 3933$ Å lines was $W_\lambda = 1.5$ Å with rapid variations up to $W_\lambda = 7.5$ Å. The stability of the IR brightness of EG UMa within 0.02^m was confirmed by the photometry of [9]. However, in his analysis of photographic archival data of the Sternberg Astronomical Institute obtained from 1968 to 1984, Shugarov [12] discovered two 0.30^m bursts in the V band, which were interpreted as accretion outbursts, in contradiction with the hypothesis that the components were fully detached.

These difficulties were explained by Bleach *et al.* [13] in their analysis of spectroscopic and photometric IR observations of EG UMa. The amplitudes of the radial velocities of the red dwarf derived from groups of emission and absorption lines coincide, but the equivalent width of the NaI $\lambda\lambda 8183, 8194$ Å doublet does not vary appreciably with the orbital phase. This suggests the absence of a hot spot due to reflection effects on the surface of the secondary. At the same time, R-band photometry revealed a dark spot with variable intensity on the surface of the red dwarf, as well as a flare whose shape and intensity was similar to those typical of UV Ceti stars. As a result, Bleach *et al.* [13] concluded that the brightness variability of EG UMa and the presence of emission lines in its spectra are both due to magnetic

Table 1. Observations: block number N, signal-to-noise ratio for a single spectrogram s/n, Julian date JD, orbital phase φ, radial velocities V_l of the primary (1) and secondary (2) derived from groups of emission (em) and absorption (abs) lines, and their dispersions σ

N	s/n	JD 2451000+	φ	$V_l^1 \pm \sigma$, km/s	$V_l^2(\mathrm{em}) \pm \sigma$, km/s	$V_l^2(\mathrm{abs}) \pm \sigma$, km/s
1	55	277.432	0.938	18 ± 13	-74 ± 13	-68 ± 6
		277.437	0.945		-65 ± 16	
		277.441	0.951		-57 ± 17	
2	28	278.512	0.556		-64 ± 9	
3	47	279.260	0.676	59 ± 11	-152 ± 13	-105 ± 6
		279.264	0.682		-153 ± 10	
		279.268	0.688		-140 ± 15	
4	44	279.470	0.991	17 ± 17	-44 ± 14	-35 ± 1
		279.474	0.997		-59 ± 18	
		279.478	0.003		-30 ± 12	
		279.482	0.009		-28 ± 15	

activity of the red component and that no reflection effects are present in the system.

However, most of the system parameters presented in [13] were derived only from statistical mass–radius and mass–luminosity relations for white and red dwarfs and cannot be considered firmly established. In the current study, we have analyzed independently obtained spectra of EG UMa and determined a set of system parameters without using any statistical assumptions. In addition, we have simulated the manifestation of reflection effects and estimated their contribution to the total observed radiation of the star. Section 2 describes our observations and data reduction. The spectroscopic data are analyzed in Section 3, and Section 4 contains a complete set of the derived parameters for EG UMa. We consider the results of our modeling of reflection effects in the spectra of the star in Section 5.

2. OBSERVATIONS AND DATA REDUCTION

We carried out spectroscopic observations of EG UMa with the 6-m telescope of the Special Astrophysical Observatory in April 1999, using an SP-124 spectrograph at the Nasmyth-1 focus [14] with a PM1024 CCD (pixel size 24×24 μm). The spectrograph was equipped with a B2 diffraction grating (1200 slits/mm), which provided a dispersion of 1.3 Å/pixel within the spectral range studied, $\Delta\lambda = 3920{-}5250$ Å. The size of the stellar images was 2", making it possible to obtain spectra with a two-pixel resolution of about 2.9 Å. Thirteen individual spectrograms of EG UMa were obtained in four observing

blocks from April 8th to 10th. Table 1 presents the block distribution of the spectrograms, Julian dates of the observations JD, orbital phases φ according to the refined ephemeris (see below), signal-to-noise ratios for the individual spectrograms s/n, the average radial velocities of the components $V_l(\mathrm{obs})$ derived from groups of emission and absorption lines, and their dispersions σ. Unfortunately, the data in block 2 were obtained under unfavorable weather conditions and can be used only for a restricted set of problems.

The spectrograms were reduced in the MIDAS package using standard techniques [15]. The single white dwarf Feige 34 [16] was used as a spectrophotometric standard for all the EG UMa spectrograms. Subsequent reduction and analysis of the EG UMa spectra were carried out using the Origin 4.0 Windows package.

3. RADIAL VELOCITIES AND EPHEMERIDES OF EG UMa

Table 1 presents heliocentric radial velocities for both components of the system. We studied the radial velocities of the red dwarf using the H_β, H_γ, H_δ, and CaII $\lambda\lambda 3933, 3968$ Å emission lines, as well as the strongest absorption lines of metals we identified in the spectra (CaI $\lambda\lambda 4435, 4454, 4578, 4585$ Å, FeI $\lambda 4482$ Å, TiI $\lambda 4535$ Å). The laboratory wavelengths were adopted from [17]. We determined the wavelengths for all the lines in the same way. We established the local continuum level in the area surrounding a measured line and subtracted it from the observed spectrum. The continuum level for the

Balmer emission lines was specified using the wing of the absorption component of the line. The observed wavelength was derived as a weighted average of the resulting line profiles:

$$\lambda_0 = \frac{\int\limits_{\lambda_1}^{\lambda_2} F_\lambda \lambda d\lambda}{\int\limits_{\lambda_1}^{\lambda_2} F_\lambda d\lambda}. \tag{1}$$

The wavelengths of intense emission lines were measured in each individual spectrogram in observing blocks 1, 3, and 4 and in the average spectrogram in block 2; weaker absorption lines of metals were studied only in the averaged spectrograms in blocks 1, 3, and 4.

We derived the radial velocities of the white dwarf by comparing the theoretical and observed profiles of the H_β, H_γ, and H_δ absorption lines. The observed profiles for all the lines were corrected by removing previously determined emission components. We used superpositions of two synthetic spectra as theoretical comparison spectra—one for a white dwarf with a hydrogen atmosphere with $T_{\text{eff}} = 13\,125$ K and $\log g = 8.05$ [13] and the other for a red dwarf with $T_{\text{eff}} = 3400$ K, $\log g = 5.0$, and $[\text{M/H}] = 0.0$. The model atmosphere of the cool component was obtained by extrapolating data from the model grid of Kurucz [18] in T_{eff} in accordance with the procedure presented in [19]; the model atmosphere of the hot component was calculated using the BINARY3 code [20]. When calculating the spectra, we took into account all continuous sources of opacity tabulated in the ATLAS5 [21], STARDISK [22], and SPECTR [23] packages, hydrogen lines broadened in accordance with the theory of Vidal *et al.* [24], about 500 000 lines of heavy elements from the lists of Kurucz [18], and basic molecular bands in accordance with the theoretical study of Nersesyan *et al.* [25], for which data were kindly presented by Ya. Pavlenko (Main Astronomical Observatory of the National Academy of Science of Ukraine). The van der Waals constants C_6 for broadening of the lines of heavy elements were found using the classical formula of Unsold [26] with the scaling factor $\Delta \log C_6 = 0.7$. We also took into account broadening due to rotation, with $V\sin(i) = 50.0$ km/s [13], and the instrumental profile, described by a Gaussian with its half-width corresponding to the spectral resolution. The resulting theoretical spectrum of EG UMa was calculated varying the ratio of the component radii r_1/r_2 in order to correctly fit the observed continuum level both at the center and edges of the studied wavelength interval $\Delta\lambda = 3920$–5250 Å.

Doppler shifts were derived by shifting the observed spectra until reaching the best fit to the observed profiles within ± 30 Å of the line centers. This procedure requires spectra with $s/n > 80$, and we used only the averaged spectrograms obtained in blocks 1, 3, and 4.

The data in Table 1 show that the procedure used to derive the red-dwarf radial velocities provides average velocity errors as low as $\sigma_e = 9.0$ km/s using the emission lines and $\sigma_e \approx 3.0$ km/s using the absorption lines. The radial-velocity differences derived from these two groups of lines, as well as from different spectrograms within the same observing block, are generally consistent. The only exception is the data from block 3, for which the absorption-line radial velocity is $\Delta V_l(\text{obs}) \approx 40.0$ km/s higher than the emission-line radial velocity. This contradicts the conclusion of [13] that the amplitudes of the red-dwarf radial velocities derived from different types of lines coincide. The accuracy of our average white-dwarf radial velocities is $\sigma_e \approx 9.0$–11.0 km/s.

Comparison of the observed red-dwarf velocities with those calculated using the refined ephemeris [13] revealed substantial discrepancies. We accordingly made a number of refinements to the ephemeris [5] using our data in combination with other published data [5, 6, 13]. The total duration of the observational interval was 7000 days, and the uncertainty in the orbital period was decreased to 10^{-6} days. We obtained the best-fit period using a gradient-descent method assuming a circular orbit, monitoring the accuracy using a χ^2 criterion. This yielded the EG UMa ephemeris

$$\text{JD} = 2451279.476(\pm0.001)$$
$$+ 0.6675779E(\pm0.0000010).$$

The derived orbital period differs from that given in [13] by 8×10^{-5} days, which can be understood as an effect of the incorrect estimation of the error in the ephemeris of Lanning [5] for the epoch of the observations of [13].

In our subsequent analysis, we did not use the $V_l(\text{obs})$ values from [5], since they yield a lower amplitude for the radial velocities of the red dwarf, K_r, compared to later studies. The red-dwarf radial-velocity curve was studied for models with circular and elliptical orbits, while we assumed the orbit of the white dwarf to be circular. Figure 1 presents the resulting radial-velocity curves, and Table 2 the derived parameters. Using the elliptical-orbit models, we confirmed the absence of eccentricity in EG UMa at a level of 0.02, as found in other studies [5, 13].

The derived amplitude K_r and velocity γ for the red dwarf are consistent with data from previous studies
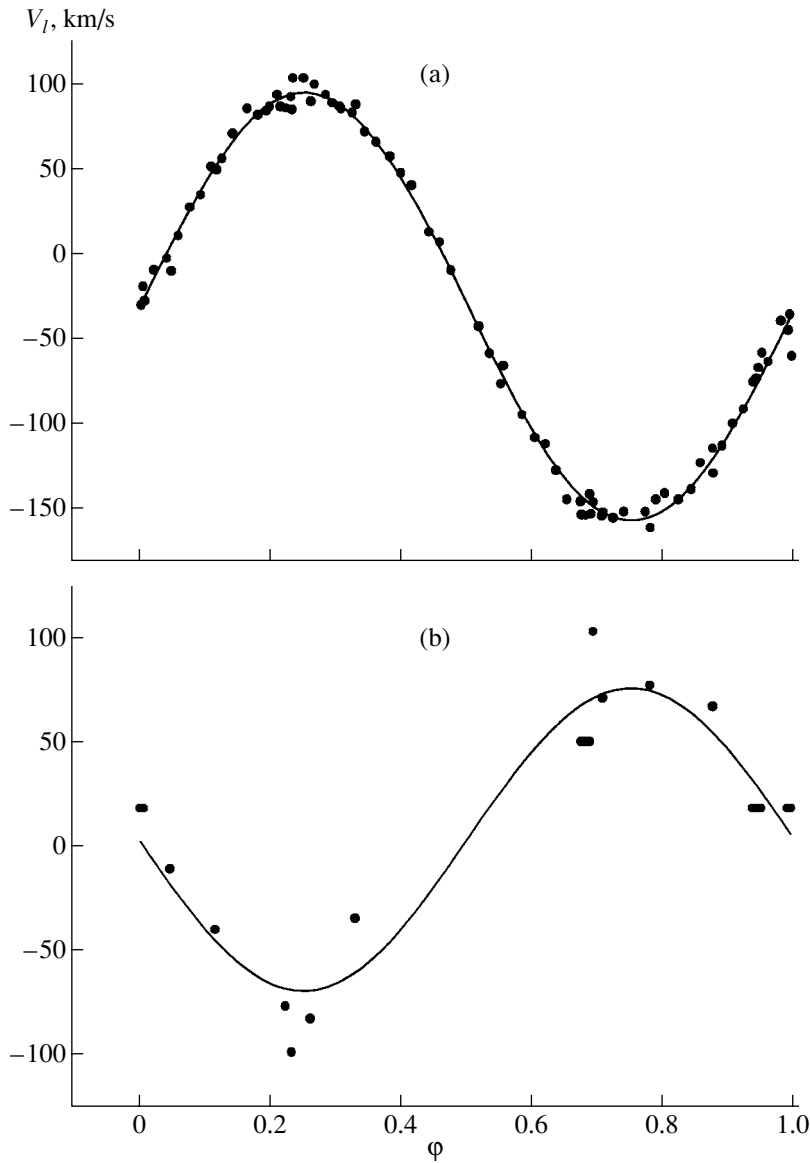
Fig. 1. Radial velocity curves for the (a) red and (b) white dwarfs in EG UMa.

($K_r = 124.7$ km/s, $\gamma_r = -32.9$ km/s [6] and $K_r = 125.9$ km/s, $\gamma_r = -29.0$ km/s [13]); their rms errors do not exceed 1.0 km/s. The corresponding parameters of the white dwarf differ from those in [6] ($K_w = -81.7$ km/s, $\gamma_w = 6.3$ km/s) by 4.0–7.0 km/s due to the low accuracy (8.0–15.0 km/s) of both techniques used to determine the radial velocities. We estimate the real uncertainty in the component mass ratio $q = M_w/M_r = 1.72$ to be roughly 5% and the uncertainty in the difference of their γ velocities $\Delta\gamma = \gamma_w - \gamma_r = 32.4$ km/s to be 3.0 km/s.

4. PARAMETERS OF EG UMa

The potential at the white-dwarf surface

$$\Omega_1 = \frac{Gm_1}{r_1} + \frac{\omega^2 \cos^2(\varphi) r_1^2}{2}, \qquad (2)$$

where ω is the angular velocity of the rotation and φ is the latitude, is calculated from the difference of the γ velocities of the components:

$$\Omega_1 = c\Delta\gamma + \Omega_2 = 50.6\Omega_\odot + \Omega_2. \qquad (3)$$

According to current models of stellar evolution [27], the gravitational potential at the surface of an M main-sequence (MS) star lies in the range $\Omega_2 = 1.0$–$1.2\,\Omega_\odot$. Neglecting the contributions of the centrifugal accelerations of the objects to the total poten-

Table 2. Parameters of EG UMa and their dispersions

Parameter	Primary	Secondary
P_{orb}, days	0.667579 ± 0.000001	
φ_0, JD	2451279.476 ± 0.001	
K, km/s	-73.0 ± 5.4	125.5 ± 0.9
γ, km/s	2.4 ± 3.6	-30.0 ± 0.6
e	0.01 ± 0.01	
ω	$170° \pm 20°$	
q	0.58 ± 0.03	
T_{eff}, K	$13125^* \pm 125$	3440 ± 70
$m/m_\odot$	0.63 ± 0.05	0.36 ± 0.04
$r/r_\odot$	0.0122 ± 0.0009	0.32 ± 0.04
$a/r_\odot$	3.20 ± 0.06	
i	$58°4 \pm 3°1$	
π	$0''.028$	

* We used the value from [13].

tial and their mutual gravitational effects, we obtain $\Omega_1 = 51.7\ \Omega_\odot$.

The mass m and radius r of a star can be derived using the known potential and gravitational force at its surface. Based on UV spectra, Sion *et al.* [7] determined $T_{eff} = 13\,000$ K and $\log g = 8.0$ for the atmosphere of the white dwarf. The similar values $T_{eff} = 13\,125 \pm 125$ K and $\log g = 8.05 \pm 0.05$ are presented in [13], and we use these values below. The adopted Ω_1 and $\log g_1$ values specify the mass of the white dwarf $m_1 = 0.63\ m_\odot$ and its radius $r_1 = 0.012\ r_\odot$. According to current models [28] for white-dwarf cooling, these parameters for the primary correspond to a star with a degenerate oxygen core with an admixture of some carbon and neon.

Bleach *et al.* [13] suggest for the secondary $m_2 = 0.42\ m_\odot$, $r_2 = 0.45\ r_\odot$, and $T_{eff} = 3150$ K. However, on evolutionary tracks for MS stars [27], this mass and radius correspond to an effective temperature of $T_{eff} = 3800-4000$ K. In addition, stars with temperatures below $T_{eff} = 3200$ K have spectral types of dM5 and later, in contrast to available estimates for the spectral type of the red dwarf (dM2 [4], dM4 [9]). Such an inconsistency could reflect disturbances in the evolution of the MS stars as they passed through the common-envelope phase and the substantial (more than 10^8 years) time for the relaxation of the red dwarf toward a quiescent state after the ejection of the envelope [7]. Therefore, estimation of the parameters of the secondary requires special attention.

We derived the mass of the red dwarf $m_2 = 0.37\ m_\odot$ from the mass of the primary and the component mass ratio. Its effective temperature was obtained from the color indices of EG UMa: $J-H = 0.68$, $H-K = 0.27$ [9], $R-H = 1.38$ [29]. The contribution of the white dwarf to the total brightness

of the system at the wavelengths studied does not exceed 10% and was taken into account in the iterative procedure used to determine the parameters. According to the photometric calibrations of [9, 18], these color indices correspond to stars with temperatures of $T_{eff} = 3200-3650$ K (assuming [M/H] = 0.0 and $\log g = 4.8-5.0$). The large differences in the obtained values are due to the presence of excess radiation in the H band [9]. To solve this problem, we carried out preliminary modeling of the NaI, FeI and TiI lines in the IR spectra [13] using the model atmosphere of [18] with $T_{eff} = 3500$ K, $\log g = 5.0$, and [M/H] = 0.0. The modeling indicated that the abundances of these elements are 0.5 dex higher than the solar values. Since the abundances of Fe, Ti, and Na are sensitive indicators of the abundances of other heavy elements, we reestimated the effective temperature using the calibration of [18] for a star with [M/H] = 0.5 and obtained $T_{eff} = 3440 \pm 70$ K.

Detailed calculations of the line profiles in the IR spectra of EG UMa [13] were carried out using the model atmosphere of [18] with $T_{eff} = 3450$ K, $\log g = 5.0$, and [M/H] = 0.5 following the procedure described above (Section 3). The profiles were calculated taking into account the microturbulence velocity ξ_{turb}, natural damping, van-der-Waals broadening, rotational broadening, and the instrumental profile. We tried to achieve the best consistency between the theoretical and observed profiles, varying the rotational velocity and the abundance of a given element. For the NaI $\lambda\lambda 8183, 8194$ Å doublet, we took into account deviations from LTE calculated in accordance with the technique proposed in [30]. Note that, in the range $\xi_{turb} = 0.7-1.8$ km/s, the lowest dispersion for the derived iron abundances was attained for $\xi_{turb} = 1.2$ km/s, and we adopted this value.

We obtained consistency between the profiles for most lines for the set of abundances [Na/H] = 0.48, [Fe/H] = 0.52 ± 0.07, and [Ti/H] = 0.53 ± 0.06, confirming the correctness of the derived atmospheric parameters. Figures 2a, 2b present examples of the consistency between the observed and theoretical line profiles. The derived rotational velocity for the red dwarf was $V \sin i = 59.2 \pm 4.2$ km/s. Bleach *et al.* [13] found the lower value $V \sin i = 44$ km/sm, with a substantial scatter for the results derived from different lines. The differences between the $V \sin i$ obtained here and in [13] are primarily due to the high heavy-element abundance in the atmosphere of the secondary. Bleach *et al.* [13] noted that their rotational velocity for the red dwarf may have been distorted by anomalies in its chemical composition. On the other hand, the formation of the spectrum of EG UMa [13] could have been affected by some additional broadening factors not taken into account
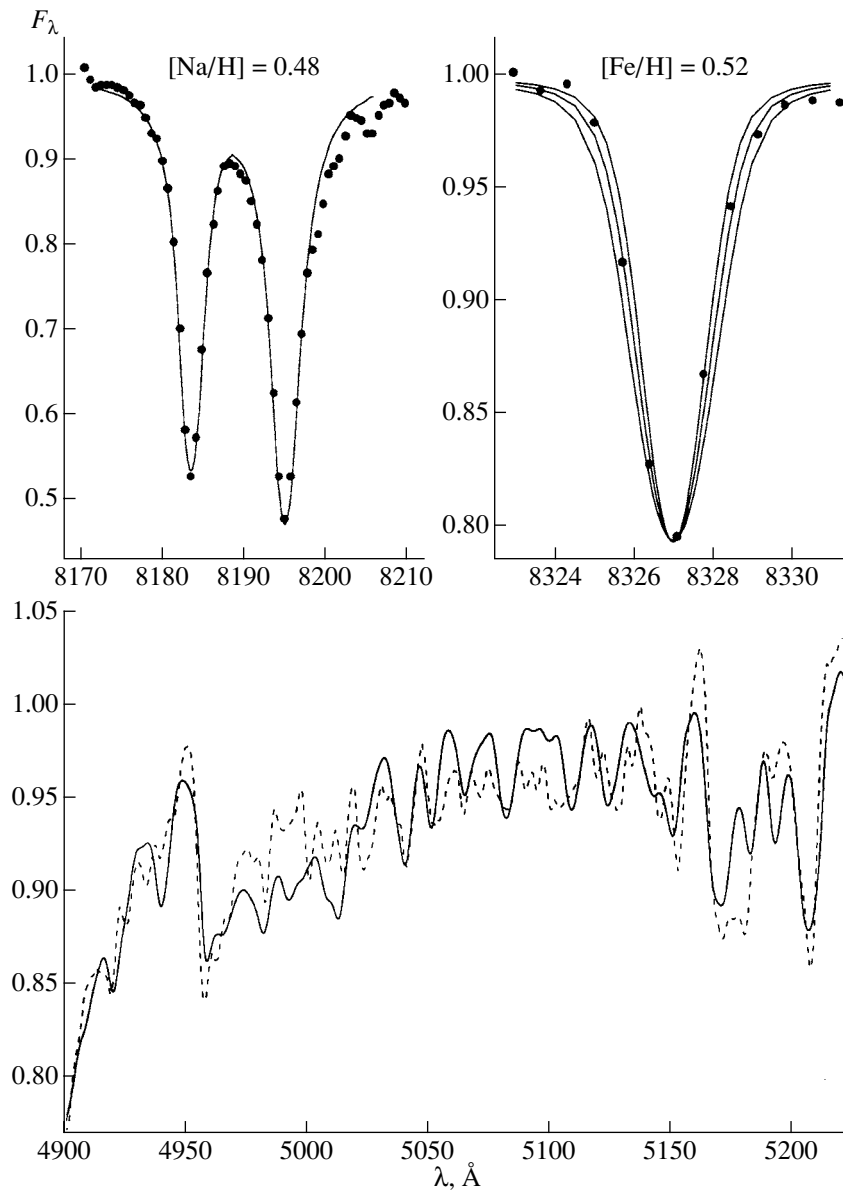
Fig. 2. Theoretical (solid curves) and observed (dots and dashed curve) spectra of EG UMa (the dots correspond to the data of Bleach *et al.* [13], and the dashed curve to the present study). In the upper left and right plots, theoretical line profiles are given for $V \sin(i) = 59$ km/s and $V \sin(i) = 45, 55, 65$ km/s, respectively.

in the modeling (incomplete correction for the radial velocity in some of the spectrograms, the presence of magnetic and velocity fields at the surface of the secondary). Therefore, our $V \sin i$ value may be somewhat overestimated (by up to $\Delta V \sin i \approx -10$ km/s); i.e., our result represents an upper limit for this parameter.

Overall, however, our line-profile analysis has confirmed the suggestion of Bleach *et al.* [13] that the rotational velocity of the secondary exceeds the velocity of synchronous rotation $V \sin(i) \approx 20$ km/s. The origin of the excess velocity is not clear, but it

may be related to the accretion of matter from the supergiant when the system underwent its common-envelope phase.

We determined the radius r_2 by modeling the observed intensities of absorption features at wavelengths $\Delta\lambda 4900-5230$ Å, where the contributions of both components to the total radiation of the system are comparable [7]. A comparison of the averaged spectrograms of EG UMa in blocks 1, 3, and 4 confirms the conclusion of Bleach *et al.* [13] that the intensities of metallic absorption lines and molecular bands are independent of orbital phase. Therefore, to increase the signal-to-noise ratio in the
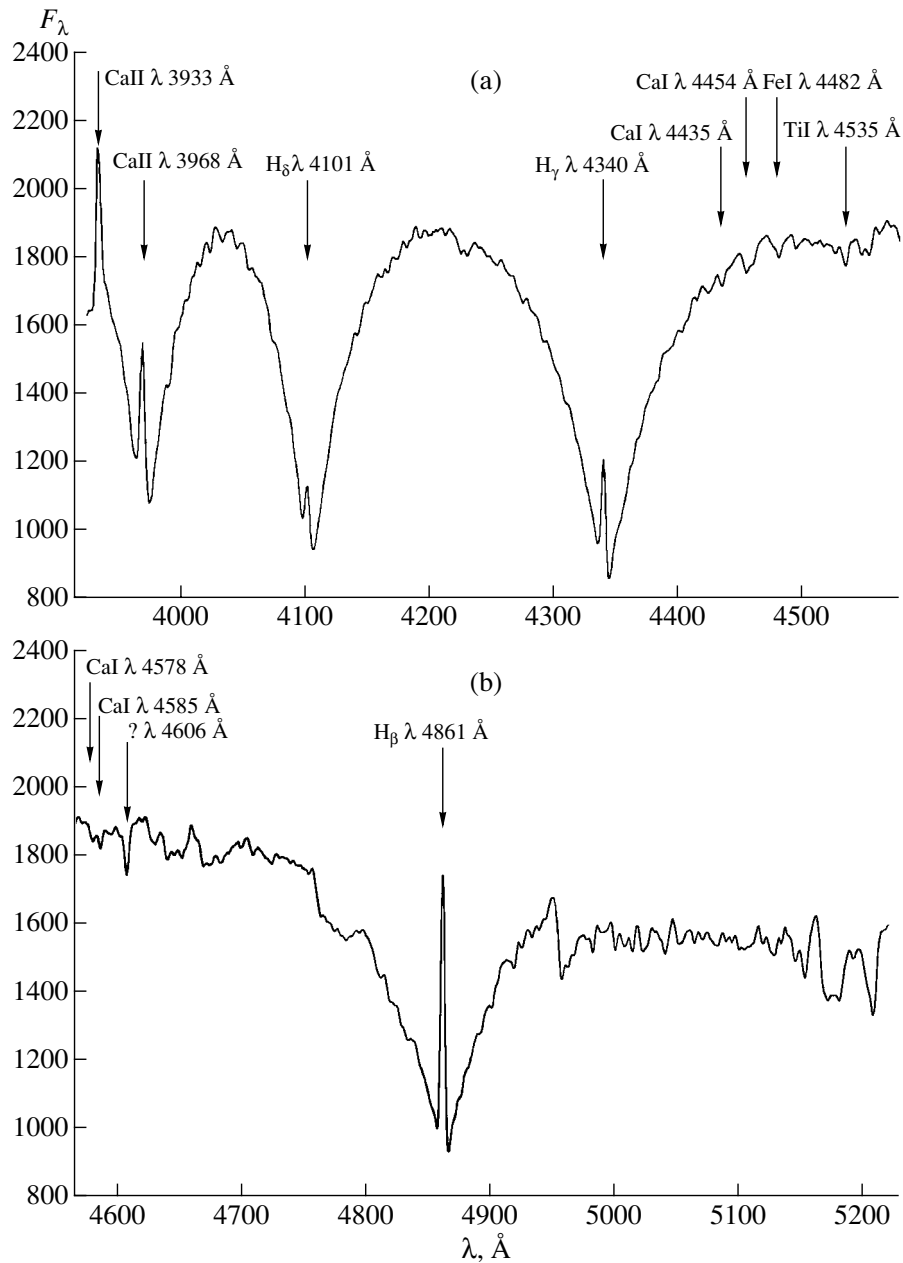
Fig. 3. Observed spectrum of EG UMa. Arrows indicate studied lines.

studied spectra, we combined all spectrograms from blocks 1, 3, and 4 after transforming them into the reference system of the secondary. Figure 3 presents the resulting spectrum of the EG UMa, which has $s/n = 150$.

Theoretical spectra for both components of EG UMa were modeled using the procedures and atmospheric parameters described, varying the ratio of their radii r_2/r_1 to achieve the best consistency with the observed spectrum. Overall, we were only able to reach moderately good consistency between the theoretical and observed spectra. The residual

differences between the spectra are probably due to insufficient accuracy of the atomic data for molecular bands at the studied wavelengths. Decreasing the magnesium abundance improves the fit, since this decreases the number density of MgH molecules while increasing the fraction of free electrons. The example of the best agreement achieved between the spectra presented in Fig. 2c corresponds to a red-dwarf radius of $r_2 = 0.32 \, r_\odot$ and a magnesium abundance of $[\mathrm{Mg/H}] = 0.15$.

In general, the new set of parameters for the secondary we have derived is consistent with current

evolutionary models for single stars. For example, on evolutionary tracks of MS stars with metallicity [M/H] = 0.50 [27], its mass and radius correspond to $T_{\text{eff}} = 3610 \pm 70$ K. We conclude that the common-envelope phase does not appreciably affect the present status of the secondary.

We calculated the parallax of EG UMa $\pi = 0.''0287$ using the effective temperature and radii of the components, the apparent V magnitude $m_v = 13.34$ [12], and the photometric calibration of [18]. The similar values $\pi = 0.''0259$ and $\pi = 0.''0334$ presented in the review [31] confirm the correctness of the parameters for EG Uma in Table 2.

5. REFLECTION EFFECTS IN EG UMa

EG UMa is characterized by a broad variability spectrum: low-amplitude brightness variations $\Delta m_R = 0.^m05$ [13], flares in broad wavelength intervals of up to $\Delta m = 0.^m5$ [12, 13], and rapid strengthening of emission lines by factors of three to five [6]. Most of the variability is stochastic and nonperiodic, and is associated with the fact that the red dwarf is a UV Ceti magnetic flare star. However, periodic variations due to reflection effects can also be seen in the radiation of EG UMa. These are typical of precataclysmic variables, but they have low amplitude and are difficult to detect in EG UMa due to the low temperature of the white dwarf. At the same time, the detection and quantitative estimation of reflection effects can help in further refinement of the system parameters and provide insight into physical processes occurring in the system.

We investigated reflection effects in EG UMa using the SPECTR package [23], based on a modified method for modeling irradiated atmospheres in a semi-grey approximation [20]. In this method, the surface of the secondary is divided into elements, and the radiation fluxes directed toward the observer are calculated for each element using models for irradiated atmospheres. The procedure for the flux calculation is similar to that used to derive the unnormalized synthetic spectrum (see Section 3). The total spectrum of EG UMa is calculated by adding the fluxes from the primary and secondary, taking into account their radii and radial velocities; it is then convolved with the sensitivity curves in the $UBVR$ bands in accordance with the data of [32]. We specified all system parameters in accordance with the data in Table 2 and supplemented the initial model of a non-irradiated secondary atmosphere [18] with a empirical model for the chromosphere to provide a correct description of the profiles of the CaII $\lambda\lambda3933, 3968$ Å emission lines at phase $\varphi = 0.0$.

Figure 4a presents the electron temperature T_e as a function of the Rosseland optical depth τ_r at various points of the hot spot, the upper panel, corresponds to the center of the spot, and the lowest panel, to a non-irradiated atmosphere. We can draw the following conclusions from these distributions.

(1) The temperature at layers $\log \tau_r > -2.0$ does not increase, and reflection effects in the continuum spectra of EG UMa are extremely small. Detailed calculations indicated that the corresponding amplitudes of brightness oscillations are from $\Delta m = 0.^m003$ in the B band to $\Delta m_R = 0.^m005$ in the R band and are therefore not detectable with the sensitivities of modern photometric observations.

Reflection effects also appear to be small for metallic lines in the first ionization state, since they originate primarily in layers with low electron temperatures. In addition, non-LTE calculations carried out using the NaI atom as an example [33] have indicated that, under the conditions present in irradiated atmospheres, the intensities of these lines are virtually independent of the temperature distribution in the chromosphere and are determined by the temperature at the depth of formation of the continuum.

(2) Chromospheric layers with $-6.0 < \log \tau_r < -4.0$ are subject to additional heating by external radiation, by up to $\Delta T_e > 500$ K, which should result in variations of the intensities of emission lines formed in these layers. In the case studied, these are the CaII $\lambda\lambda3933, 3968$ Å lines. The Balmer lines can form only when $T_e > 5000$ K; in EG UMa, such temperatures are present in the rarefied envelope around the secondary.

Figure 4c presents the results of our modeling of the CaII resonance doublet profile at several phases φ, and Figure 4b shows the variations of the equivalent width W_λ of the CaII $\lambda = 3933$ Å emission lines. The amplitude of the W_λ oscillations is substantial ($\Delta W_\lambda \approx 1.0$ Å) and should easily be detected in spectroscopic observations with a moderate resolution. However, the flare activity of the magnetic red dwarf very much complicates the detection of reflection effects in emission lines. For example, of the ten observations of Stauffer [6], four fall during an intense flare with $W_\lambda \approx 7.0$ Å and another occurs during a strengthening of the CaII $\lambda = 3933$ Å lines to $W_\lambda \approx 2.8$ Å. Five of the observations correspond to the quiescent state of the red-dwarf chromosphere, with $1.15 < W_\lambda < 1.86$ Å, and these show a dependence close to the theoretical one (Fig. 4b). Our spectra obtained on April 10 at phases $\varphi = 0.65$ and 0.00 in the quiescent state of the chromosphere have intensity ratios for the CaII lines that are in good agreement with the theoretical values (Figs. 4c, 4d). On the contrary, the observations of April 8 (phase $\varphi = 0.95$) show a strengthening of all emission lines, indicating the occurrence of a weak local flare.
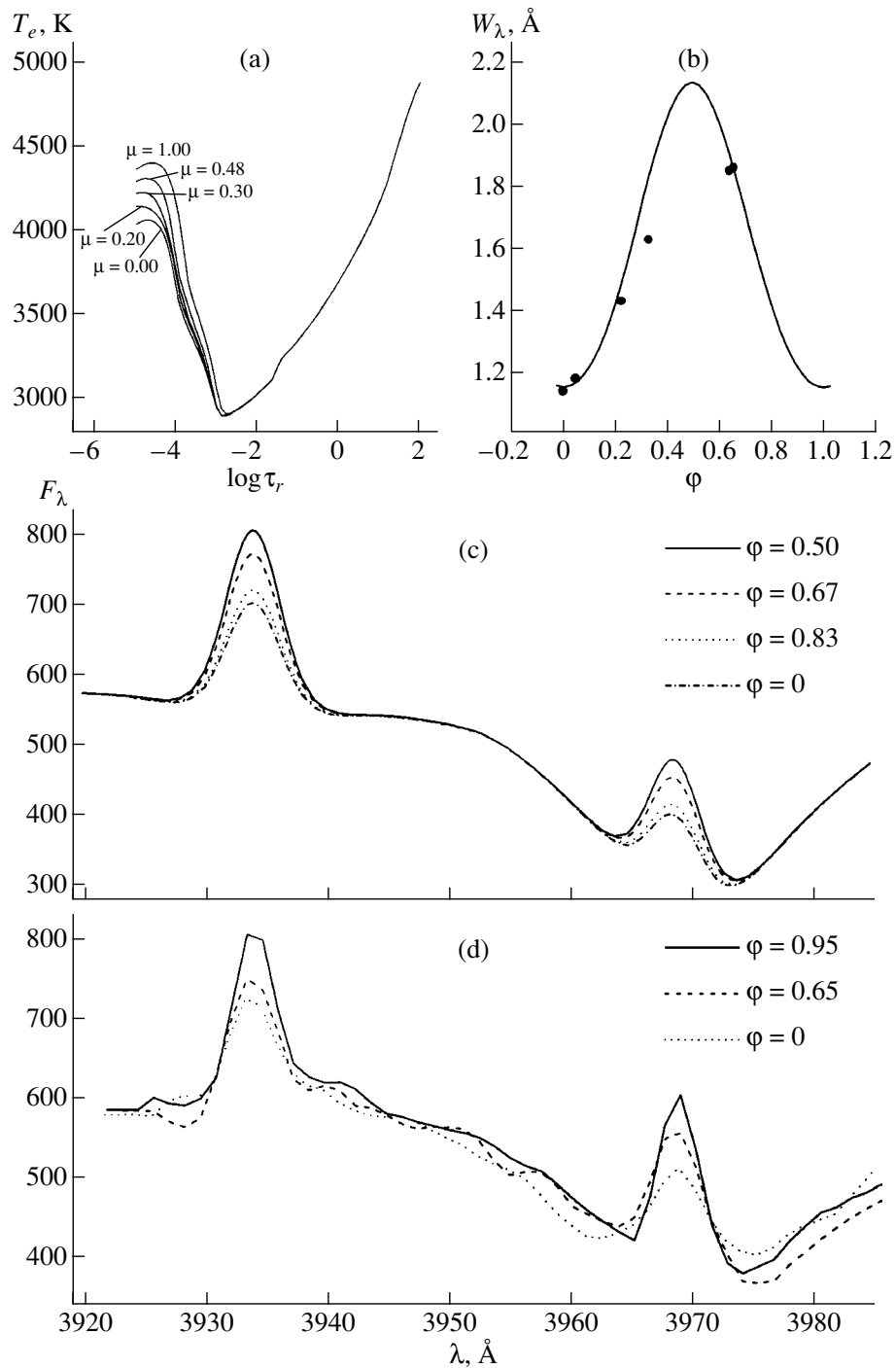
Fig. 4. Reflection effects in EG UMa: (a) distribution of the temperature T_e as a function of optical depth τ_r in the atmosphere of the red dwarf for various cosines of the angle of incidence of the external radiation μ; (b) theoretical (solid curve) and observed (dots) [6] equivalent widths for the CaII $\lambda 3933$ Å line as a function of orbital phase; (c) theoretical and (d) observed spectra at several orbital phases.

Thus, reflection effects in the CaII $\lambda\lambda 3933, 3968$ Å emission lines of EG UMa can be detected in uniform sets of observations made during a single night in the quiescent state of the red-dwarf chromosphere.

6. CONCLUSION

The latest reviews concerning precataclysmic variables [34, 35] include ~ 50 objects, of which only RR Cae contains a white dwarf with an effective

temperature lower than that of EG UMa. According to current models for the evolution for detached binaries that have passed through a common-envelope stage [8], the cooling of the white dwarf does not depend on the presence of the secondary or its parameters. Therefore, RR Cae and EG UMa stand out among currently known precataclysmic variables as having the longest periods of evolution after the ejection of the common envelope. For this reason, the following recent results for EG UMa are of special interest for the theory of the evolution of close binaries.

(1) The parameters of the secondary are consistent with the predictions of current evolutionary models for single MS stars [27]; i.e., the relaxation time for red dwarfs to reach a normal state after the common-envelope stage does not exceed the lifetime of the system $T = 3 \times 10^8$ yr [7]. At the same time, the rotational velocity of the red dwarf exceeds the synchronous-rotation velocity by a factor of two to three, suggesting a low efficiency for the tidal interactions between the components in the present state of EG UMa.

(2) The inner chromospheric activity of the red dwarf appears to be the determining factor in the formation of emission lines in the spectrum of EG UMa. It is obvious that similar effects of chromospheric activity may occur in other old precataclysmic variables, in which the presence of emission lines is treated as a manifestation of reflection effects. Examples of such activity for several systems detected by Wood *et al.* [36] will make it possible to estimate the commonness of magnetic red dwarfs in close binaries.

(3) Reflection effects in the CaII emission lines in the spectra of EG UMa can be distinguished, provided certain conditions are satisfied. At present, such effects have been studied for only 14 detached systems [35, 37] whose primaries have high effective temperatures ($T_{\text{eff}} \geq 30\,000$ K). The fact that reflection effects can be observed in the spectrum of EG UMa, which contains one of the coolest white dwarfs, provides evidence that these effects should be measurable quantitatively for essentially all precataclysmic variables with $P_{orb} \leq 1^{\text{d}}0$. It is desirable to obtain such measurements for as wide a set of objects as possible, since they can provide further input for the development of the theory of radiative interaction of components in close binaries.

7. ACKNOWLEDGMENTS

REFERENCES

1. H. Ritter, Astron. Astrophys. **169**, 139 (1986).
2. C. B. Stephenson, Publ. Astron. Soc. Pac. **72**, 387 (1960).
3. J. L. Greenstein, in *Proceedings of the First Conference on Faint Blue Stars, 1965,* p. 97.
4. C. B. Stephenson, in *White Dwarfs (IAU Symp. 42), 1971,* p. 61.
5. H. H. Lanning, Astrophys. J. **253**, 752 (1982).
6. J. R. Stauffer, Astron. J. **94**, 996 (1987).
7. E. M. Sion, F. Wesemael, and E. F. Guinan, Astrophys. J. **279**, 758 (1984).
8. I. J. Iben and A. Tutukov, Astrophys. J. **418**, 343 (1993).
9. R. G. Probst, Astrophys. J., Suppl. Ser. **53**, 335 (1983).
10. R. G. Probst and W. O. O'Connell, Astrophys. J. Lett. **252**, L69 (1982).
11. M. De Kool and H. Ritter, Astron. Astrophys. **267**, 397 (1993).
12. S. Y. Shugarov, Inf. Bull. Var. Stars, No. 2612 (1984).
13. J. N. Bleach, J. H. Wood, M. S. Catalan, *et al.*, Mon. Not. R. Astron. Soc. **312**, 70 (2000).
14. V. L. Afanas'ev, V. A. Lipovetskiĭ, V. P. Mikhaĭlov, *et al.*, Astrofiz. Issled. Spets. Astrofiz. Obs. Ross. Akad. Nauk **31**, 128 (1991).
15. P. Ballester, in *Proceedings of the Data Analysis Workshop: 4th ESO/ST-ECF Garching, 1992,* p. 177.
16. P. Massey, K. Strobel, and E. Anderson, Astrophys. J. **328**, 315 (1988).
17. A. R. Striganov and N. S. Sventitskii, *Tables of Spectral Lines of Neutral and Ionized Atoms* (Atomizdat, Moscow, 1966; Plenum, New York, 1968).
18. R. L. Kurucz, SAO CD-ROMs (Smithsonian Astrophysical Observatory, Cambridge, USA, 1994).
19. V. F. Suleĭmanov, Pis'ma Astron. Zh. **22**, 107 (1996) [Astron. Lett. **22**, 92 (1996)].
20. N. A. Sakhibullin and V. V. Shimanskiĭ, Astron. Zh. **73**, 793 (1996) [Astron. Rep. **40**, 723 (1996)].
21. R. L. Kurucz, SAO Spec. Rep. **309**, 1 (1970).
22. V. F. Suleymanov, Astron. Astrophys. Trans. **2**, 197 (1992).
23. N. A. Sakhibullin and V. V. Shimanskiĭ, Astron. Zh. **74**, 432 (1997) [Astron. Rep. **41**, 378 (1997)].
24. C. R. Vidal, J. Cooper, and E. W. Smith, Astron. Astrophys., Suppl. Ser. **25**, 37 (1973).
25. S. E. Nersisyan, A. V. Shavrina, and A. A. Yaremchuk, Astrofizika **30**, 247 (1989).
26. A. Unsold, *Physik der Sternatmospheren* (Springer-Verlag, Berlin, 1955, 2nd ed.).
27. L. Girardi, A. Bressan, G. Bertelli, and C. Chiosi, Astron. Astrophys., Suppl. Ser. **141**, 371 (2000).
28. J. A. Panei, L. G. Althaus, and O. G. Benvenuto, Astron. Astrophys. **353**, 970 (2000).

29. T. Zwitter and U. Munari, Astron. Astrophys., Suppl. Ser. **107**, 503 (1994).
30. L. I. Mashonkina, V. V. Shimanskiĭ, and N. A. Sakhibullin, Astron. Zh. **77**, 893 (2000) [Astron. Rep. **44**, 790 (2000)].
31. G. P. McCook and E. M. Sion, Astrophys. J., Suppl. Ser. **65**, 603 (1987).
32. V. L. Straizys, *Multicolor Stellar Photometry* (Mokslas, Vil'nyus, 1977; Pachart Publ. House, Tucson, 1992).
33. N. A. Sakhibullin and V. V. Shimanskiĭ, Pis'ma Astron. Zh. **26**, 369 (2000) [Astron. Lett. **26**, 309 (2000)].
34. H. Ritter and U. Kolb, Astron. Astrophys., Suppl. Ser. **129**, 83 (1998).
35. T. C. Hillwing, R. K. Honeycutt, and J. W. Robertson, Astron. J. **120**, 1113 (2000).
36. J. H. Wood, S. Harmer, and J. J. Lockley, Mon. Not. R. Astron. Soc. **304**, 335 (1999).
37. H. Ritter, Z. Y. Zhang, and U. Kolb, Astron. Astrophys. **360**, 969 (2000).

Translated by K. Maslennikov

Motion of an Eruptive Prominence in the Solar Corona

B. P. Filippov[1], N. Gopalswamy[2], and A. V. Lozhechkin[1]

[1]*Institute of Terrestrial Magnetism, Ionosphere, and Radio Wave Propagation, Russian Academy of Sciences, Troitsk, Moscow oblast, 142190 Russia*
[2]*Catholic University of America, Washington DC, USA*
Received August 13, 2001; in final form September 13, 2001

Abstract—A model for the nonradial motion of an eruptive prominence in the solar corona is proposed. Such motions, which can sometimes be inaccessible to observation, result in an apparent break in the causal link between eruptive prominences and coronal mass ejections. The global magnetic field of the Sun governs coronal plasma motions. The complex structure of this field can form prominence trajectories that differ considerably from a simple vertical rise (i.e., radial motion). A solar filament is modeled as a current-carrying ring or twisted toroidal magnetic rope in equilibrium with the coronal magnetic field. The global field is described using two spherical harmonics. A catastrophic violation of the filament equilibrium followed by its rapid acceleration—eruption—is possible in this nonlinear system. The numerical solution of the equations of motion corresponds well to the eruption pattern observed on December 14, 1997. © 2002 MAIK "Nauka/Interperiodica".

1. INTRODUCTION

Coronal mass ejections (CMEs) into the heliosphere occur almost every day, even in periods of minimum solar activity, with their number usually increasing to four to five events per day during periods of maximum activity [1, 2]. The plasma sporadically released in such events represents a considerable fraction of the matter in the slow solar wind, and, therefore, substantially affects the geomagnetic environment. To forecast the arrival of interplanetary plasma clouds at the Earth, we must know the characteristic conditions and regions on the Sun that can produce such outbursts of matter. Observations with orbiting coronographs often reveal the appearance of a CME from a coronal streamer, which disappears after the passage of the disturbance and is restored only the next day, or even later [3, 4]. However, there are also many cases when a CME is not followed by the disruption of a streamer or is observed in a region that does not contain streamers [5].

A large fraction of CMEs are observed near lines of polarity reversal of the large-scale magnetic field, where $B_r = 0$ [4, 6]. This suggests an electromagnetic mechanism for the acceleration of the ejected material and can explain the statistical relation between CMEs and other phenomena associated with lines of polarity reversal, such as streamers, flares, and filaments (prominences). Of phenomena observed in lower layers of the solar atmosphere, eruptive prominences are most closely related to CMEs. First, there is a very large statistical correlation between them

[7–9]. Second, a prominence rising to considerable heights in the corona is often a component of a larger formation—a CME. A typical CME is composed of three basic elements: a bright core (remnants of the eruptive prominence), an extended dark cavity with decreased density surrounding the core, and an outer diffuse envelope, whose projection onto the plane of the sky resembles a loop with its ends fixed on the Sun [10–12].

However, a careful comparison of the positions of filaments on the disk that have disappeared suddenly and CMEs reveals some problems in the interpretation of CMEs as continuations of the filament eruptions in the upper corona. The heliolatitudes of the disrupted filaments and of the subsequent coronal ejections sometimes differ by tens of degrees [13–15]. For example, Cliver and Webb [14] found that, in a period of maximum activity, the number of CMEs with heliolatitudes >60° was four times the number of disrupted filaments at latitudes >45°. If these two phenomena are causally related, it is unclear why their latitudes (position angles) differ so strongly.

Another objection against the concept of a CME as a further development of the eruption of a prominence in the upper corona is based on the kinematics of these phenomena [16]. The velocity of an eruptive prominence (bright core of a CME) is usually less than the velocity of the outer loop (envelope of the CME) by a factor as large as 1.5. For this reason, most researchers believe that the prominence cannot "push" the CME and be the reason for its formation. On the other hand, prominences can be considered as
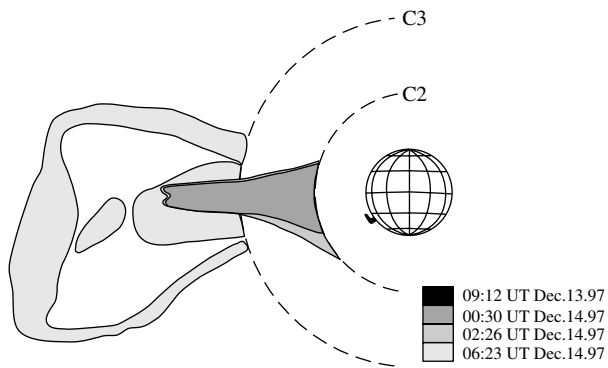
Fig. 1. Schematic of the filament eruption and coronal ejection of December 14, 1997. Objects observed at various times are marked by different shading. The dashed semicircles C2 and C3 correspond to the inner boundaries of the fields of view for the C2 and C3 coronographs, respectively (SOHO/LASCO and Meudon Observatory data).

Fig. 2. Lines of the global solar magnetic field used in the model under consideration. Dashed lines denote polarity reversals at the photospheric surface. The thick solid curve in the left-hand part of the figure shows the locus of equilibrium points of the ring for various values of the current. The point C is the critical position above which the equilibrium is unstable.

indicators of local coronal currents [17, 18]. The magnetic field of the current flowing in the corona over a line of polarity reversal (a magnetic rope) creates the conditions necessary to accumulate dense prominence material, affecting the distribution of matter in the corona [19]. A sudden loss of the current's equilibrium as a result of some parameters attaining critical values could lead to eruption of the prominence, with the action on the ambient corona increasing the density and forming an envelope [20, 21]. The kinematics of this process agree well with the observed velocity pattern.

The aim of the present paper is to show that the considerable heliographic separation of the observed manifestations of eruption in its initial and final stages may result from nonradial (i.e. nonlinear) motions of currents in the corona due to their interaction with the large-scale magnetic field. Compared to our earlier work [22], we consider here a more complex coronal magnetic field, taking into account radial stretching by the solar wind. The observational data for the entire sequence of events forming the specific event used as a basis for choosing the model parameters will be presented in Section 2. We describe a model for equilibrium of a current in the large-scale solar magnetic field in Section 3. Further, we present and discuss the results of our numerical solutions of the equations of motion.

2. THE FILAMENT ERUPTION AND CORONAL EJECTION OF DECEMBER 14, 1997

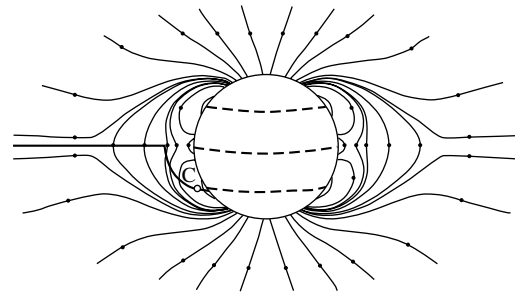A very illustrative and well-observed case of a considerable latitude separation between an eruptive prominence and a possibly associated CME is described by Gopalswamy *et al.* [15]. The eruption of the prominence was observed by the Nobeyama radioheliograph on December 14, 1997. This prominence had the form of a very high arch (to 0.25 $R_\odot$) extending from S20° to S50°. It was also clearly seen in Meudon Observatory spectroheliograms obtained on December 13 in the Ca K_3 line. The eruption began at approximately 00:38 UT. The arch rose radially with an acceleration of 5 m/s^2 and left the field of view of the radioheliograph within 2.5 h after the beginning of its motion, when its velocity was about 44 km/s.

The characteristic features of the eruption in the white-light corona (continuum) became detectable by the LASCO/C2 coronograph starting at 02:03 UT. The eruption began with the expansion of the southern part of the equatorial streamer, distorting its shape, which was initially nearly symmetric about the equator. The southern boundary continued to move southward. At 02:26 UT, the southern part of the streamer at the inner edge of the field of view of the C2 coronograph ($\sim 2R_\odot$) was almost twice as wide as the northern part (Fig. 1). Unfortunately, no C2 coronograph data were received from 02:26 to 06:23 UT. At 06:23 UT, there is no streamer in the coronal image—it has been disrupted. In its place, at a distance of $\sim 10R_\odot$, we can see the loop of a CME with a flat or even bent-over top. The angular size of the loop is $\sim 40°$, and it is symmetric about the equatorial plane. The loop moves radially with a velocity in the plane of the sky of ~ 570 km/s.

The time sequence for these events fits well with the idea that a sudden increase in the current associated with the prominence resulted in a reconstruction of the corona and the formation of a coronal ejection. Despite the fact that an extrapolation of the prominence velocity assuming constant acceleration gives only 110 km/s for the distance where the CME is observed [15], this discrepancy should not be considered

critical for the following reasons. First, the acceleration could have increased with time. The acceleration derived for the initial stage of the prominence's rise may be underestimated, since forces acting on the current are balanced near the equilibrium position. As the prominence moves away from this position, the imbalance grows, increasing the acceleration. Second, as noted above, the velocity of the CME envelope should exceed the velocity of the prominence due to the specific nature of the motions of field lines in the magnetic configuration under consideration. Nevertheless, the spatial pattern seems to contradict this picture. In the initial stage, the prominence moves radially toward the southeast (in heliographic coordinates). In the final stage, the ejection also propagates radially, but toward the east. What is the factor acting on the eruptive prominence to change the initial direction of motion?

3. MODEL OF PROMINENCE EQUILIBRIUM IN THE CORONAL MAGNETIC FIELD

In a classical picture, a quiet prominence is located over a line of polarity reversal of the photospheric magnetic field. It is surrounded by a cavity, above which, as a rule, there is a coronal helmet (streamer). However, a streamer can sometimes encompass more than one line of polarity reversal of the large-scale field [23]. In the case we consider here, there is only one streamer near the equatorial plane (as is typical for activity minimum) and the eruption of the prominence develops from moderate latitudes. An idealized mean pattern for the global solar magnetic field in periods of minimum activity has three lines of polarity reversal at the photosphere and a dipole-type field in the upper corona (Fig. 2). Therefore, the third harmonic (hexapole) of the expansion of the magnetic-field potential in spherical functions dominates near the photospheric surface, while the first harmonic (dipole) dominates at distances of the order of the solar radius. Only the dipole component affects streamer formation. The stretching of the helmet apex is usually attributed to the action of radial plasma flows, i.e., to the solar wind [24]. The corresponding deformation of the magnetic field is described using a source surface [25]: the field is assumed to still be potential in the spherical layer between the photosphere and source surface (whose radius is usually taken to be $\sim 2.5 R_\odot$), with the boundary conditions at the source surface formulated so that there is no tangential field component. At larger distances, the field is assumed to be purely radial, with the current concentrated in the plane of the magnetic equator, forming a heliospheric current sheet [26].

Let us consider an axially-symmetric model for the equilibrium of a filament in the corona. The filament

is represented by a thin current-carrying plasma ring (torus) located above the photosphere along a heliographic parallel. A similar model for a ring located in the equatorial plane was analyzed by Lin *et al.* [27]. The equation of motion in an ideal magnetohydrodynamical approximation takes the form

$$\rho_p \frac{d\mathbf{v}}{dt} = \frac{1}{c}[\mathbf{j} \times \mathbf{B}] - \text{grad}\, p + \mathbf{F}_g, \qquad (1)$$

where ρ_p is the matter density, $\mathbf{v}$ the velocity, $\mathbf{j}$ the current density, $\mathbf{B}$ the magnetic induction, p the pressure, and $\mathbf{F}_g$ the force of gravity. After integrating over the torus volume, we can obtain the equation of motion of the torus as a whole, as well as an equation describing variations of its inner radius. This latter equation is not of interest to us here. If the equilibrium conditions for the inner radius a are approximately satisfied, we can derive certain relations between the quantities appearing in the first equation [28]. In cylindrical coordinates (ρ, φ, z) with their origin at the solar center and the z axis directed along the rotational axis, the equations of motion for a toroidal segment with unit length take the form

$$m\frac{d^2\rho}{dt^2} = \frac{I}{c}(B_z^{(ex)} + B_z^{(m)} + B_z^{(I)}) \qquad (2)$$
$$- mgR_\odot^2 \frac{\rho}{(\rho^2 + z^2)^{3/2}},$$

$$m\frac{d^2 z}{dt^2} = -\frac{I}{c}(B_\rho^{(ex)} + B_\rho^{(m)}) \qquad (3)$$
$$- mgR_\odot^2 \frac{z}{(\rho^2 + z^2)^{3/2}},$$

where $B^{(ex)}$ is the magnetic field produced by sources located beneath the photosphere and by currents in the solar-wind region, $B^{(m)}$ is the field produced by inductive currents in the photosphere, which prevent the penetration of the coronal-current field into the Sun, $B^{(I)}$ is the field produced by the current flowing along the ring axis, and g is the free-fall acceleration at the photospheric level.

The potential of the photospheric magnetic field in a spherical layer assuming axial symmetry can be written as an expansion in spherical functions [29]:

$$u = R_\odot \sum_n P_n(\cos\theta) \qquad (4)$$

$$\times \left[c_n \left(\frac{r}{R_\odot}\right)^n + (1 - c_n)\left(\frac{R_\odot}{r}\right)^{n+1} \right] g_n,$$

where P_n are Legendre polynomials and

$$c_n = -\left[\left(\frac{R_s}{R_\odot}\right)^{2n+1} - 1\right]^{-1} \qquad (5)$$

are coefficients chosen so that the potential u is zero at the source surface $r = R_s$. The components of the magnetic field are determined by the expression $\mathbf{B} = -\mathrm{grad}u$:

$$B_r^{(ex)} = g_1\cos\theta p_1(r) + \frac{1}{2}g_3\cos\theta(5\cos^2\theta - 3)p_3(r), \tag{6}$$

$$B_\theta^{(ex)} = \frac{1}{2}g_1\sin\theta[p_1(r) + 3c_1]$$

$$+\frac{1}{8}g_3\sin\theta(15\cos^2\theta - 3)\left[p_3(r) + 7c_3\left(\frac{r}{R_\odot}\right)^2\right],$$

$$B_\varphi^{(ex)} = 0,$$

where

$$p_1(r) = (1 - c_1)\left(\frac{R_\odot}{r}\right)^3 - c_1,$$

$$p_3(r) = (1 - c_3)\left(\frac{R_\odot}{r}\right)^5 - 3c_3\left(\frac{r}{R_\odot}\right)^2.$$

The signs of g_1 and g_3 should be the same in order for no field singularities to be present in polar regions and for the singular line to be in the equatorial plane. The ratio g_1/g_3 depends on the height ξ of the singular line (point) over the photosphere (in units of $R_\odot$) and is determined by the equation $B_\theta^{(ex)}\left(\xi R_\odot, \frac{\pi}{2}\right) = 0$:

$$\frac{g_3}{g_1} = \frac{2(s^7 - 1)(\xi^5 - s^3\xi^2)}{3(s^3 - 1)(\xi^7 - s^7)}, \tag{7}$$

where $s = R_s/R_\odot$. The position of the singular point where the three loop systems touch each other specifies the basic geometry for the magnetic configuration. The field becomes radial beyond the source surface, so

$$B_r^{(ex)}(r,\theta) = B_r^{(ex)}(R_s,\theta)\left(\frac{R_s}{r}\right)^2, \quad r > R_s. \tag{8}$$

Before substituting them into the equations of motion (2) and (3), the field components in spherical coordinates (6) and (8) must be transformed into cylindrical coordinates using the standard formulas:

$$B_\rho = B_r\sin\theta + B_\theta\cos\theta, \tag{9}$$

$$B_z = B_r\cos\theta - B_\theta\sin\theta,$$

$$\sin\theta = \frac{\rho}{r}, \quad \cos\theta = \frac{z}{r}, \quad r = \sqrt{\rho^2 + z^2}.$$

The induction-current field $B^{(m)}$ can be found using the image method widely used in electrostatics: it is known (see, for example, [30, p. 169]) that there is a close correspondence between problems in magnetostatics and electrostatics. Based on symmetry considerations, it is clear that the field due to induction

currents outside the sphere should be equivalent to the field of a current-carrying ring located inside the sphere on the line joining the outer ring to the sphere center. Based on the condition that the only nonzero component of the vector potential A_φ be constant on the sphere, we obtain the ring radius

$$\rho_m = \rho\frac{R_\odot^2}{r^2} \tag{10}$$

and the amplitude of the ring current

$$I_m = I\frac{r}{R_\odot}. \tag{11}$$

The magnetic field of a current-carrying ring is given by the well-known formulas ([30], p. 173)

$$B_\rho = \frac{2I(z - z_m)}{c}\frac{(z - z_m)}{\rho\sqrt{(\rho_m + \rho)^2 + (z - z_m)^2}} \tag{12}$$

$$\times\left[-K(k) + \frac{\rho_m^2 + \rho^2 + (z - z_m)^2}{(\rho_m - \rho)^2 + (z - z_m)^2}E(k)\right],$$

$$B_z = \frac{2I(z - z_m)}{c}\frac{1}{\sqrt{(\rho_m + \rho)^2 + (z - z_m)^2}} \tag{13}$$

$$\times\left[K(k) + \frac{\rho_m^2 - \rho^2 - (z - z_m)^2}{(\rho_m - \rho)^2 + (z - z_m)^2}E(k)\right],$$

where

$$k^2 = \frac{4\rho_m\rho}{(\rho_m + \rho)^2 + (z - z_m)^2}, \tag{14}$$

$K(k)$ and $E(k)$ are complete elliptical integrals of the first and second kinds, respectively, and z_m is the coordinate of the z plane of the ring.

The field $B^{(I)}$, which is produced by the filament current and tends to stretch it, cannot be calculated using (12) and (13) due to their divergence at $\rho \to \rho_m$ and $z \to z_m$. However, this field is equal to the field required to hold the current-carrying plasma ring in equilibrium and has the opposite sign [28]:

$$B_z^{(I)} = \frac{I}{c\rho}\left(\ln\frac{8\rho}{a} - \frac{3}{2} + \frac{l_i}{2}\right), \tag{15}$$

where l_i is a coefficient of the order of unity that depends on the current distribution in the torus cross section. Since the detailed distribution of the field and pressure inside the prominence is not of interest to us, we shall take the current distribution over the cross section to be that for a force-free field inside a cylindrical tube when $l_i = 1$ [27].

4. THE INITIAL EQUILIBRIUM POSITION

Solving (2) and (3) with zero left-hand terms for various amplitudes of the current I, we can find the equilibrium positions of the filament. If the amplitude of the coronal magnetic field produced by sources
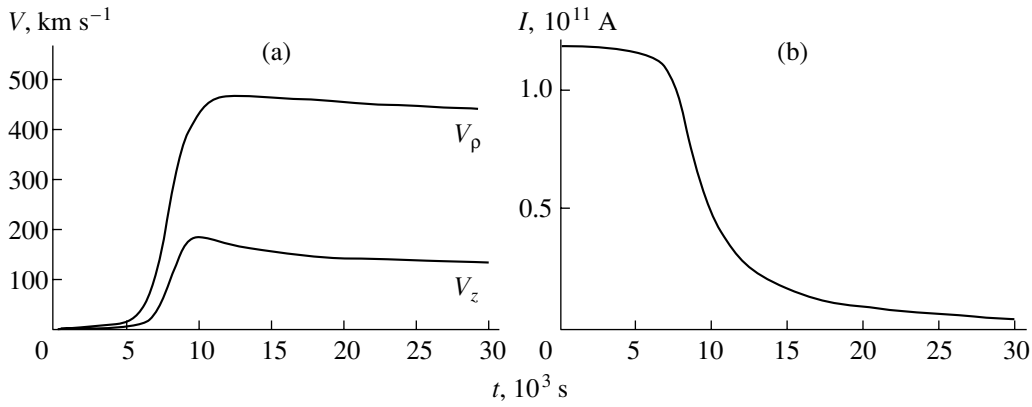
Fig. 3. Time profiles of the (a) velocity and (b) electric current in an eruptive filament.

under the photosphere is 1–10 G, a filament in the corona at a height of about 10–30 Mm can be in equilibrium if the corresponding currents are 10^{10}–10^{11} A. For typical values of $\sim 10^5$ g/cm, the mass of the prominence does not appreciably affect the equilibrium position in the lower corona, since the gravitational force is about two orders of magnitude weaker than the electromagnetic forces acting on the filament. The geometrical positions of the equilibrium points of the filament are shown by the line in Fig. 2. Each value of the current corresponds to two equilibrium points in this curve—one above and one below some critical point whose current I_c corresponds to a single solution of (2) and (3). If the current exceeds the critical value, equilibrium cannot be achieved in the corona. This picture is similar to the two-dimensional model of a filament [31] and the axial model for a purely dipole field [27]: except that the lower equilibrium position is stable, and when the current exceeds a critical value, we obtain a "catastrophic" transition to a considerably higher equilibrium position (which may be unattainable due to the velocity acquired), i.e., eruption of the filament.

In a rigorous study of the filament's stability against displacements, we must take into consideration the induction equation, which expresses the conservation of magnetic flux through the filament contour:

$$\Phi = \Phi_{ex} + LI = \text{const}, \qquad (16)$$

where

$$L = 4\pi\rho \left(\ln\frac{8\rho}{a} - \frac{3}{2} \right) \qquad (17)$$

is the self-induction of a current-carrying ring [30]. The flux of the external field can be found by integrating B_z over the circular region bounded by the ring:

$$\Phi_{ex} = 2\pi \int_0^{\rho} B_z^{(ex)} \rho' \, d\rho'. \qquad (18)$$

Substituting expressions following from (6) and (8) taking into account (9) into (18), we obtain

$$\Phi_{ex}(\rho, z) \qquad (19)$$

$$= \begin{cases} \Phi_1|_0^{\rho}, & r < R_s, \\ \\ \Phi_1|_0^{\rho_0} + \Phi_2|_{\rho_0}^{\rho}, & r > R_s, z < R_s, \\ \\ \Phi_2|_0^{\rho}, & z > R_s, \end{cases}$$

where

$$\Phi_1(\rho, z) = \frac{\pi\rho^2}{4r^2} \left[4g_1 r^2 p_1(r) - g_3 p_2(r)(r^2 - 5z^2) \right],$$

$$\Phi_2(\rho, z) = -\frac{\pi R_\odot^2 z^2}{4r^4} \left[4g_1 \, r^2 p_1(r) \right.$$
$$\left. - g_3 p_3(r)(6r^2 - 5z^2) \right],$$

$$\rho_0 = \sqrt{R_\odot^2 - z^2}.$$

5. MOTION OF THE FILAMENT

Having attained a critical point in the course of its slow evolution due to variations of the external magnetic field or its own current, the filament becomes unstable and the eruption occurs. The corresponding behavior of the filament can be studied via numerical solution of the equations of motion (2) and (3) together with the induction equation (16).

The time profile of the filament's velocity after its current has increased by approximately 1% near the critical point C is shown in Fig. 3a. The initial velocity is small, and the filament slowly rises along the equilibrium curve. Such behavior is due to the fact that the magnetic field near the initial equilibrium position is very weak: the current flows along the zero line of the total field due to photospheric sources and the
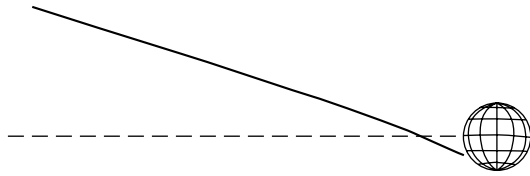
Fig. 4. Trajectory of motion of an eruptive prominence.

reflected current. Further, the filament sharply accelerates. In addition, due to the increase in the ring size, the amplitude of the current decreases (Fig. 3b) in accordance with (16). As a result, the filament reaches a maximum velocity, which then gradually decreases. Within a certain range of parameters, the maximum velocity depends almost linearly on the filament mass. This mass, which can be estimated only crudely from observations, represents a free parameter, which can be varied to obtain agreement between the kinematic characteristics and observations. Note that the mass $m \approx 7.5 \times 10^4$ g/cm required to obtain a velocity $v \approx 500$ km/s is quite typical for prominences. In fact, the mass of the eruptive prominence decreases during its rise, since some fraction of the material flows back to the chromosphere along the legs of the loop, which are still fixed on the Sun. This effect, which we have not taken into account in our model, may compensate the decrease in the velocity at late stages of the eruption.

The trajectory of the filament's motion during the eruption is shown in Fig. 4. As noted above, the initial part of this trajectory is close to the equilibrium curve shown in Fig. 2. Further, the trajectory deviates from this curve, apparently because of the action of inertial forces. Due to its inertia, the filament intersects the equatorial plane and continues to move almost linearly at a small angle ($\approx 20°$) to the equatorial plane.

6. CONCLUSION

We have considered the motion of a magnetic rope in the solar corona from a stable equilibrium position in lower layers to the solar-wind region. We believe that this process models the eruption of a prominence and the formation of a coronal mass ejection. Unfortunately, currently available observational facilities do not enable us (or enable only rarely) to trace the detailed evolution of a plasma bunch from an initial stationary state to a large-scale coronal disturbance—CME. The fields of view of instruments designed for observations of the inner and outer corona do not overlap. Moreover, the time intervals between successive images given by space observations are often large for studies of dynamical phenomena, due to limitations on the load on the satellite communication channels, preventing the formation of a unified picture of dynamic phenomena observed. The evolution of plasma structures during hidden periods could be very complex, making it difficult to fit together extrapolations upward and downward in the corona. This is particularly true of the trajectories and velocities of prominences and coronal mass ejections.

Since the basic mechanism for the acceleration of solar material ejected into interplanetary space (CMEs) is electrodynamic, the complex coronal magnetic field governing the plasma motion can lead to unexpected evolution of plasma bunches. Instead of radial (i.e., purely vertical at a given point) motion along a straight line, the plasma may travel over considerable distances along the surface. If in addition the main phase of the acceleration is not observed, phenomena in the lower and upper corona may appear nearly unrelated. This was precisely the case for the event of December 14, 1997, that formed the basis for our modeling. Our model does not agree with the observations in detail (indeed, this was not our primary aim), but demonstrates that the phenomena observed in the lower and upper corona may be consequences of a single process of the expansion of a magnetic rope. We used a fairly crude representation for the complex coronal field, with only two spherical harmonics. The magnetic rope corresponding to the filament is completely detached from the Sun, while the ends of the loop of the eruptive prominence always remain connected to the solar surface. As a result, some material can flow back to the chromosphere, modifying the kinematics of the phenomenon under study. In addition, we did not take into consideration any dissipative processes or factors resulting in acceleration of the solar wind. For these reasons, this model cannot provide an exact description of the real event (for example, when the trajectory deviates from the equatorial plane by a small angle). However, it does provide a good general picture of the event and a unified interpretation of processes near and far from the solar surface that initially seemed contradictory.

REFERENCES

1. D. F. Webb and R. A. Howard, J. Geophys. Res. **99**, 4201 (1994).

2. O. C. St. Cyr, R. A. Howard, N. R. Sheeley, Jr., *et al.*, J. Geophys. Res. **105**, 18169 (2000).

3. R. M. Illing and A. J. Hundhausen, J. Geophys. Res. **91**, 10951 (1986).

4. A. J. Hundhausen, J. Geophys. Res. **98**, 13177 (1993).

5. M. D. Andrews, A.-H. Wang, and S. T. Wu, Sol. Phys. **187**, 427 (1999).

6. N. S. Shilova, Astron. Astrophys., Suppl. Ser. **144**, 371 (2000).

7. N. R. Sheeley, Jr., R. A. Howard, M. J. Koomen, and D. J. Michels, Astrophys. J. **272**, 349 (1983).

8. D. F. Webb and A. J. Hundhausen, Sol. Phys. **108**, 383 (1987).

9. O. C. St. Cyr and D. F. Webb, Sol. Phys. **136**, 379 (1991).

10. F. Crifo, J. P. Picat, and M. Cailloux, Sol. Phys. **83**, 143 (1983).

11. D. G. Sime, R. M. MacQueen, and A. J. Hundhausen, J. Geophys. Res. **89**, 2113 (1984).

12. E. W. Cliver and D. F. Webb, in *New Perspectives on Solar Prominences (IAU Colloquium 167),* Ed. by D. Webb, D. Rust, and B. Schmieder (Astron. Soc. of the Pacific, San Francisco, 1998), Astron. Soc. Pac. Conf. Ser. **150**, 479 (1998).

13. N. Gopalswamy, Y. Hanaoka, and H. S. Hudson, Adv. Space Res. **25**, 1851 (2000).

14. A. J. Hundhausen, in *The Many Faces of the Sun: A Summary of the Results From NASA's Solar Maximum Mission,* Ed. by K. T. Strong, J. L. R. Saba, B. M. Haisch, and J. T. Schmelz (Springer-Verlag, New York, 1999), p. 143.

15. B. P. Filippov, in *New Perspectives on Solar Prominences (IAU Colloquium 167),* Ed. by D. Webb, D. Rust, and B. Schmieder (Astron. Soc. of the Pacific, San Francisco, 1998), Astron. Soc. Pac. Conf. Ser. **150**, 257 (1998).

16. B. P. Filippov, Izv. Akad. Nauk, Ser. Fiz. **63**, 2174 (1999).

17. B. C. Low, Sol. Phys. **167**, 217 (1996).

18. B. P. Filippov and N. S. Shilova, Astron. Zh. **72**, 222 (1995) [Astron. Rep. **39**, 195 (1995)].

19. B. P. Filippov, Astron. Astrophys. **313**, 277 (1996).

20. R. Schwenn, B. Inhester, S. P. Plunkett, *et al.*, Sol. Phys. **175**, 667 (1997).

21. B. P. Filippov, A. V. Lozheckin, and N. Gopalswamy, Sol. Phys. (2001) (in press).

22. G. W. Pneuman, Sol. Phys. **6**, 225 (1969).

23. K. H. Schatten, J. M. Wilcox, and N. F. Ness, Sol. Phys. **6**, 442 (1969).

24. I. S. Veselovsky and O. A. Panassenko, Adv. Space Res. **26**, 819 (2000).

25. J. Lin, T. G. Forbes, P. A. Isenberg, and P. Demoulin, Astrophys. J. **504**, 1006 (1998).

26. V. D. Shafranov, in *Reviews of Plasma Physics,* Ed. by M. A. Leontovich (Gosatomizdat, Moscow, 1963; Consultants Bureau, New York, 1966), Vol. 2.

27. M. D. Altschuler and G. Newkirk, Jr., Sol. Phys. **9**, 131 (1969).

28. L. D. Landau and E. M. Lifshitz, *Course of Theoretical Physics,* Vol. 8: *Electrodynamics of Continuous Media* (Nauka, Moscow, 1982; Pergamon, New York, 1984).

29. M. M. Molodenskiĭ and B. P. Filippov, Astron. Zh. **64**, 1079 (1987) [Sov. Astron. **31**, 564 (1987)].

Translated by Yu. Dumin

Twist of Magnetic Fields in Solar Active Regions

Hongqi Zhang[1], Shudong Bao[1], and Kirill M. Kuzanyan[1,2]

[1]*National Astronomical Observatories, Chinese Academy of Sciences, Beijing 100012, China*

[2]*Heliophysics Lab, Institute of Terrestrial Magnetism, the Ionosphere, and Radio-Wave Propagation, Troitsk, Moscow region, 142190 Russia*

Received September 18, 2001; in final form October 19, 2001

Abstract—We study the twist properties of photospheric magnetic fields in solar active regions using magnetographic data on 422 active regions obtained at the Huairou Solar Observing Station in 1988–1997. We calculate the mean twist (force-free field α_f) of the active regions and compare it with the mean current-helicity density of these same active regions, $h_c = \mathbf{B}_\parallel \cdot (\bigtriangledown \times \mathbf{B})_\parallel$. The latitude and longitude distributions and time dependence of these quantities is analyzed. These parameters represent two different tracers of the α effect in dynamo theory, so we might expect them to possess similar properties. However, apart from differences in their definitions, they also display differences associated with the technique used to recalculate the magnetographic data and with their different physical meanings. The distributions of the mean α_f and h_c both show hemispherical asymmetry—negative (positive) values in the northern (southern) hemisphere—although this tendency is stronger for h_c. One reason for these differences may be the averaging procedure, when twists of opposite sign in regions with weak fields make a small contribution to the mean current-helicity density. Such transequatorial regularity is in agreement with the expectations of dynamo theory. In some active regions, the average α_f and h_c do not obey this transequatorial rule. As a whole, the mean twist of the magnetic fields α_f of active regions does not vary significantly with the solar cycle. Active regions that do not follow the general behavior for α_f do not show any appreciable tendency to cluster at certain longitudes, in contrast to results for h_c noted in previous studies. We analyze similarities and differences in the distributions of these two quantities. We conclude that using only one of these tracers, such as α_f, to search for signatures of the α effect can have disadvantages, which should be taken into account in future studies. © *2002 MAIK "Nauka/Interperiodica"*.

1. INTRODUCTION

The configuration of magnetic fields at the solar surface and their evolution are important problems in solar physics. It is believed that the magnetic field is generated by a dynamo operating near the base of the convection zone, then emerges to the solar surface. A strong twist of the photospheric magnetic field is often observed in solar active regions, which may carry information about the α effect as a driver of the solar dynamo. Recently, magnetic helicity was employed to describe the twist of the magnetic fields in solar active regions. Several previous studies of the transequatorial change in sign of the magnetic current helicity have been carried out [1–5]. The longitude distribution of the magnetic helicity in solar active regions was analyzed in [6, 7]. Bao and Zhang [4] found a link between the monthly averaged sunspot number and current helicity during the 22nd solar cycle. The temporal and spatial dependences of the mean force-free coefficient are analyzed in [5].

The magnetic twist can also be indirectly inferred from chromospheric Hα structures around sunspots [8, 9], the distribution of quiescent filaments [10], and

soft X-ray images [11]. These observations provide information on the twist of the magnetic field above the solar photosphere. The question is: what it is that twists the magnetic field at the solar surface? We hope that studies of the magnetic-field twist will reveal information about the properties of solar turbulent convection, and thereby the mechanism for the generation of the solar magnetic field. Both the twist and current helicity have been independently analyzed previously.

In the present study, we compute both of these quantities using the same data and compare their spatial and temporal structures. These parameters represent two tracers of the α effect in dynamo theory, so we might expect them to possess similar properties. The aim of this paper is to establish how similar or different these quantities are.

In Section 2, we describe how the α effect in dynamo theory may be related to observed quantities. In Section 3, we describe the observational data and observing technique. In Sections 4–6, we report similarities and differences between the derived properties of the quantities under investigation.

2. THE α EFFECT IN DYNAMO THEORY

The α effect in dynamo theory (see, for example, [12]) is an important quantity used to characterize turbulent convection in the solar convective zone. This effect is believed to enable regeneration of the magnetic field via the dynamo mechanism. The α effect is estimated in [13] to be

$$\alpha_{\text{ef}} = -\frac{\tau}{3}\langle \mathbf{v} \cdot \bigtriangledown \times \mathbf{v}\rangle, \tag{1}$$

where τ is the turbulent correlation time and $\mathbf{v}$ is the velocity of turbulent fluctuations. There are no reliable estimates of this effect based on observations. Therefore, the α effect has been extensively studied theoretically. Some authors have suggested that the dynamo quantity α_{ef} increases with magnetic-field strength (for example, [14, 15]).

An expression for α_{ef} in terms of the current helicity [see formula (9) below] was derived using a first-order smoothing approximation in [16] and without this approximation in [17]. Using this (or a similar) relationship, some properties of the solar dynamo mechanism can be traced using photospheric vector magnetograms. It has been suggested that the α effect in solar dynamo theory is connected with the current helicity of the fluctuating magnetic field [16–17]. Under certain assumptions, we have

$$\alpha_{\text{ef}} = -\frac{\eta}{\langle \mathbf{B}\rangle^2}\langle \mathbf{B}' \cdot \bigtriangledown \times \mathbf{B}'\rangle, \tag{2}$$

where η is the molecular magnetic diffusivity, $\langle \mathbf{B}\rangle$ the mean field, and $\mathbf{B}'$ the fluctuating field. The magnetic fields in active regions are believed to be made up primarily of the fluctuating field, with the magnetic fluctuations being statistically stationary. Other assumptions are discussed in the references presented above. There is no explicit criterion for identifying observed active-region fields as mean or fluctuating in the sense of mean-field dynamo theory [18], but we suggest that the α effect has a definite correlation with the twist and current helicity of the magnetic fields in active regions. Thus, the current-helicity distribution contains some qualitative statistical information on the α effect in dynamo theory. While the relationship between the current helicity and the dynamo α effect is a complex problem, we expect that functions of the helicity density and twist have positive correlations with the α effect. We also note that other opinions have been expressed in some studies, such as [19], which is dedicated to the generation of magnetic helicity under the action of solar turbulent convection [19].

3. HELICITY AT THE SOLAR SURFACE

3.1. Expressions for the Helicity and Twist

With $\mathbf{B}$ denoting the magnetic induction, the density of the current helicity is defined to be

$$h_c = \mathbf{B} \cdot \bigtriangledown \times \mathbf{B}. \tag{3}$$

Separating h_c into two parts determined by the parallel ($\parallel$) and perpendicular ($\perp$) components of the magnetic field to the line of sight, we can write

$$h_c = \mathbf{B}_\parallel \cdot (\bigtriangledown \times \mathbf{B})_\parallel + \mathbf{B}_\perp \cdot (\bigtriangledown \times \mathbf{B})_\perp. \tag{4}$$

We can assume that the field is force-free within a single active region (see, for example, [20]). We then have for the force-free magnetic field

$$\bigtriangledown \times \mathbf{B} = \alpha_f \mathbf{B}, \tag{5}$$

where the constant α_f can be calculated as

$$\alpha_f = \frac{\mathbf{B}_\parallel \cdot (\bigtriangledown \times \mathbf{B})_\parallel}{B_\parallel^2}. \tag{6}$$

Thus,

$$h_c = \alpha_f B^2 = \left(\frac{B^2}{B_\parallel^2}\right) \mathbf{B}_\parallel \cdot (\bigtriangledown \times \mathbf{B})_\parallel, \tag{7}$$

where B is the absolute value of the magnetic field. Note that α_f has only dimensions of inverse length and not explicitly of magnetic-field strength.

3.2. Observational Estimates of the Current Helicity and Twist

Existing solar vector magnetographs can be used to measure the three components of the photospheric magnetic field $\mathbf{B} = \{B_x, B_y, B_z\}$. Let B_z be the component of the magnetic field along the line of sight and B_x and B_y be vertical (transverse) components of the magnetic field relative to the line of sight. Since active regions are usually not located near the center of the solar disk, the effect of projection becomes important for magnetic fields in active regions but is not the main problem in analyses of the magnetic-field configurations of active regions at relatively high latitudes. Most of the active regions were observed at latitudes $\pm 30°$.

The current-helicity parameters h_z (part of the current helicity h_c) and α_f can be calculated from observed photospheric vector magnetograms:

$$h_z = \mathbf{B}_\parallel \cdot (\bigtriangledown \times \mathbf{B})_\parallel = B_z\left(\frac{\partial B_y}{\partial x} - \frac{\partial B_x}{\partial y}\right), \tag{8}$$

and

$$\alpha_f = \frac{\mathbf{B}_\parallel \cdot (\bigtriangledown \times \mathbf{B})_\parallel}{B_\parallel^2} = \left(\frac{\partial B_y}{\partial x} - \frac{\partial B_x}{\partial y}\right)/B_z. \tag{9}$$
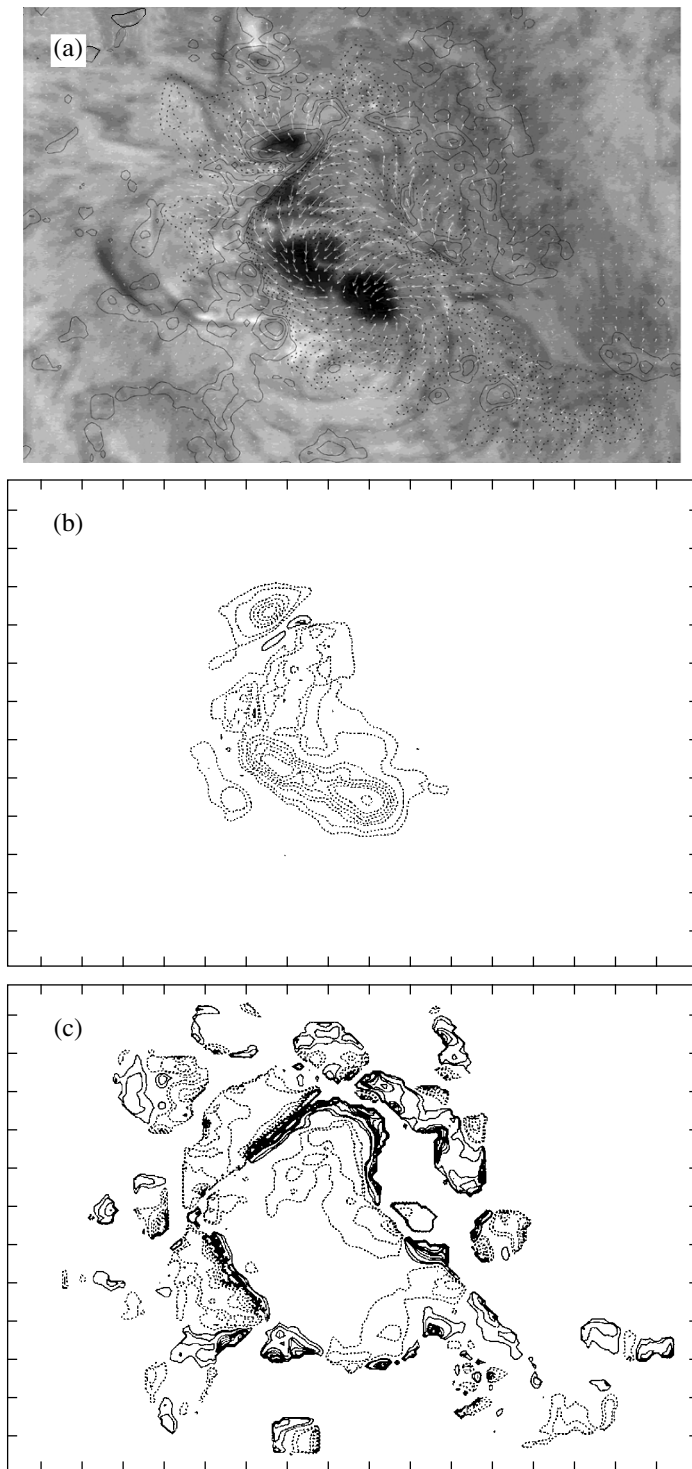
Fig. 1. (a) Vector magnetogram for the active region NOAA 6659 at 05:29 UT on June 9, 1991. The solid (dashed) contours indicate positive (negative) values of the longitudinal magnetic field of ±20, 160, 640, 1280, 1920, 2240, 2560 and 2880 G. (b) Electric-current helicity parameter $\mathbf{B}_{\parallel} \cdot (\nabla \times \mathbf{B})_{\parallel}$. The solid (dashed) contours indicate positive (negative) regions of the current-helicity distribution of ±0.25, 0.5, 1.0, 1.25, 1.5, 1.75, 2.0, 2.5 ($\times10^{-1}$ G^2/m). (c) Force-free field α_f in areas where the longitudinal field is larger than 100 G. The solid (dashed) contours indicate positive (negative) values of the α_f distribution of ±0.5, 1.0, 2, 2.5, 3.0, 3.5, 4.0, 5.0 ($\times 10^{-7}$ m^{-1}). North is up and East is to the left.

Both of these parameters likewise do not provide any real information on the horizontal component of the electric current in current-helicity calculations. The horizontal component of the electric current can sometimes make an important contribution to the total helicity in the photosphere, since the force-free field approximation fails throughout the solar convective zone. However, this approximation is believed to be acceptable for small enough areas in an active region.

The instruments and data-reduction technique have been discussed in previous papers [21, 4]. We resolved the 180° ambiguity in the transverse field and computed it using the techniques described in these papers.

To calculate the helicity parameters, we used only selected domains of the active regions and took into account only pixels far from magnetic neutral lines (e.g., [3]). For this purpose, we applied selection criteria to the magnetic-field components and current [4]. Namely, in order to reduce the influence of noise, which in the original magnetograms does not normally exceed 20 G for the line-of-sight (longitudinal) field $B_\parallel$ and 100 G for the transverse field $B_\perp$, we removed pixels in which the observed fields were lower than these values before calculating h_c and α_f and further neglected these pixels in the averaging. The resulting noise in J_z was calculated to be about 1 mA/m^2, and the accuracy in α_f and h_c was about 20−25%. Thus, we removed pixels in the vicinity of magnetic neutral lines when determining the averages.

It is interesting that, although the intensity distributions of h_z and α_f are different, as a rule these parameters have the same signs in the same areas of the active regions [7]. To best illustrate the basic properties of the current helicity parameters h_z and α_f, we present a vector magnetogram of the active region NOAA 6659 on June 9, 1991, and the corresponding values of h_z and α_f calculated using this magnetogram (Fig. 1). We find that the distributions of the current helicity h_z and twist α_f are similar to those obtained in [7]. This means that the distributions of these parameters over the active region are relatively similar, even if the intensities of the current-helicity parameters in an active region are normally spread over a relatively wide range, as for NOAA 6659 (see Fig. 2).

3.3. Statistical Reduction of the Twist and Current-Helicity Data

To study the statistical properties of the current helicity, we calculated the mean helicity parameters of the active regions. Assuming a force-free field using
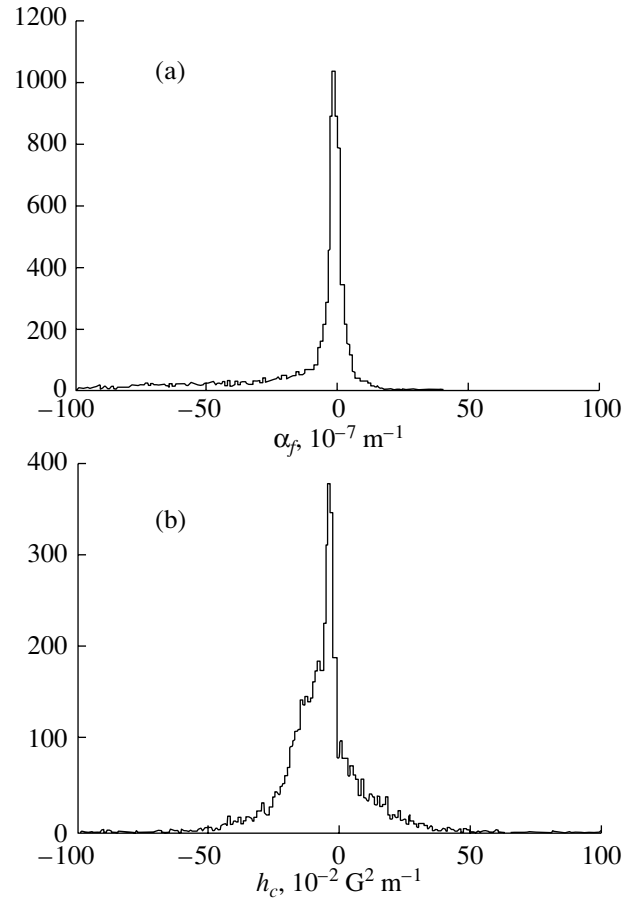

Fig. 2. Distributions of the (a) twist α_f (10^{-7} m^{-1}) and (b) current-helicity density h_c (10^{-2} G^2/m) for pixels in the magnetogram of NOAA 6659 at 05:29 UT on June 9, 1991.

(8), we can obtain the mean value $\langle \alpha_f \rangle$ for the active regions, where the angular brackets denote a spatial average. Neglecting the contribution of the transverse component of the electric current, taking into account relation (7), we calculate the mean density of the current helicity in the photosphere $\langle h_c \rangle$.

Both $\langle \alpha_f \rangle$ and $\langle h_c \rangle$ have been used earlier in studies of the helicity properties of active regions, although they were analyzed separately from each other. In the current study, we computed $\langle \alpha_f \rangle$ and $\langle h_c \rangle$ using the same data and compared their spatial and temporal structures.

We used photospheric vector magnetograms of solar active regions obtained with the vector magnetograph of the Huairou Solar Observing Station. The data cover the period 1988−1997 and include most large active regions present in these ten years. We computed $\langle \alpha_f \rangle$ and $\langle h_c \rangle$ as described above (see, for example, [3, 4]) for 422 active regions (one magnetogram per region). For the sake of simplicity, we omit the angular brackets $\langle \, \rangle$ below.
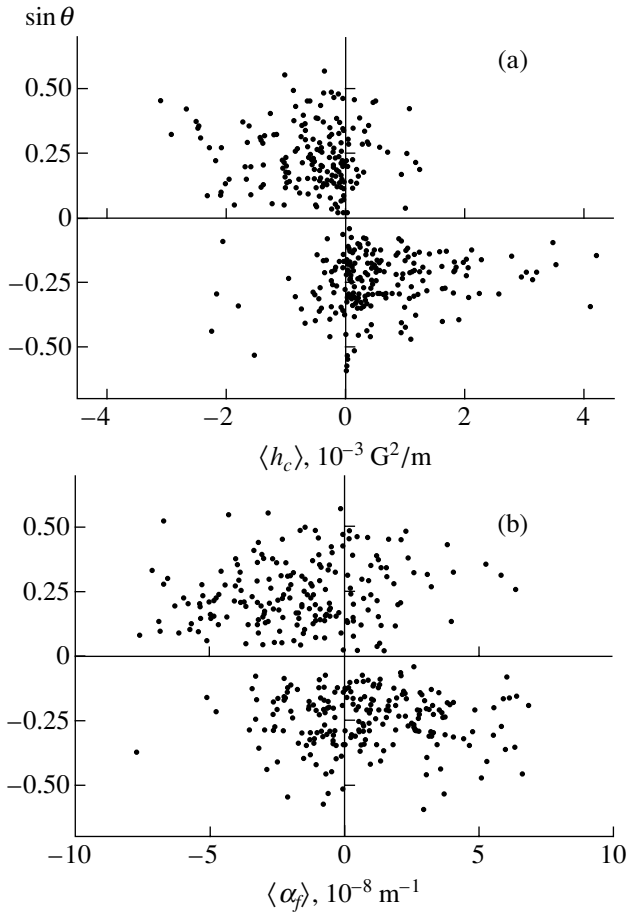
Fig. 3. Latitude distributions of the (a) mean current-helicity density $\langle \mathbf{B}_{\parallel} \cdot (\nabla \times \mathbf{B})_{\parallel} \rangle$ and (b) the mean twist $\langle \alpha_f \rangle$ for 422 active regions. Each point represents a single active region.

4. LATITUDE DISTRIBUTION OF THE TWIST AND CURRENT HELICITY. INFLUENCE OF THE PROJECTION EFFECT ON THE MAGNETIC-FIELD ESTIMATES

Figure 3 shows the latitude distributions of α_f and h_c. Although the definitions of the two helicity parameters differ, they show similar behavior—the magnetic fields in opposite hemispheres are mainly twisted in opposite directions. Figure 4 presents the distributions of α_f and h_c averaged over latitude intervals with representative numbers of observational data points. Figure 5 shows histograms of h_c and α_f for the active regions.

For $h_c = \mathbf{B}_{\parallel} \cdot (\nabla \times \mathbf{B})_{\parallel}$, 84% of the active regions in the northern hemisphere and 81% in the southern hemisphere have negative and positive mean current-helicity densities, respectively. The percentage of active regions following this tendency is lower for α_f. Only 74% (62%) of active regions in the northern (southern) hemisphere show this tendency. This is
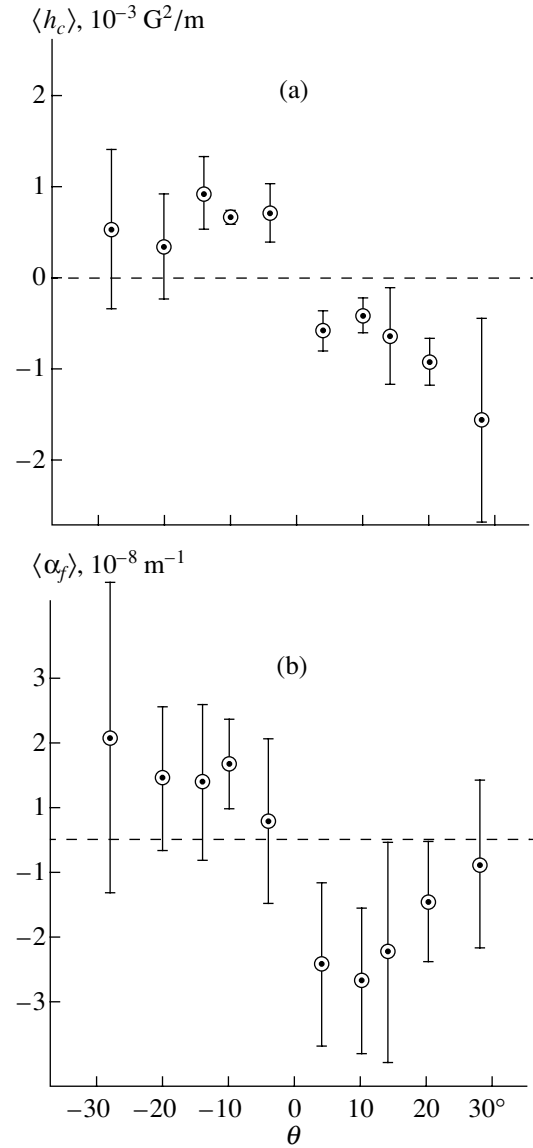
Fig. 4. Values of the (a) mean current-helicity density $\langle \mathbf{B}_{\parallel} \cdot (\nabla \times \mathbf{B})_{\parallel} \rangle$ and (b) twist density $\langle \alpha_f \rangle$ averaged over latitude intervals with representative numbers of observations. We used five intervals between latitudes of $0°$, $8°$, $12°$, $16°$, $24°$, and $32°$ in each hemisphere. The vertical bars show 95% confidence intervals.

consistent with the results of [2], although our definition of α_f is slightly different from that used by Pevtsov *et al.* [2]. With few exceptions, most of the active regions were observed in the range $\pm 30°$. The maxima of the mean current-helicity density occur near $\sin \theta = \pm 0.25$, where θ (the solar latitude) is about $\pm 15°$, in agreement with [22]. However, these patterns could be a consequence of our selection of the active regions for study, as well as of the fact that the current-helicity parameters were probably
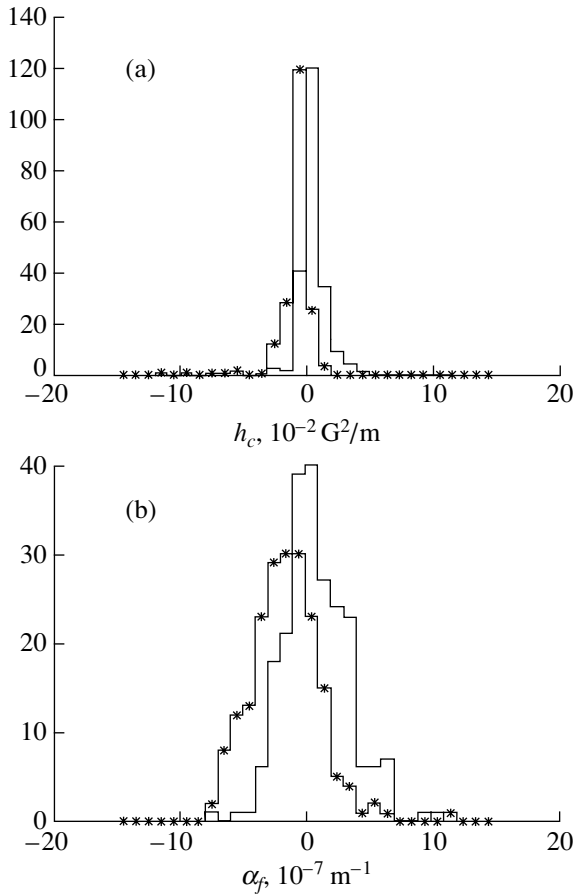
Fig. 5. Histograms of the distributions of the mean (a) current-helicity density h_c (G^2/m) and (b) α_f (m^{-1}) for the 422 active regions. The distributions with (without) asterisks show the current-helicity parameters in the northern (southern) hemispheres.

analyzed over regions of strong magnetic fields, which are usually present at such latitudes.

Figure 6 shows the relation between h_c and α_f. In about 40% of the active regions, the mean h_c and α_f have opposite signs. The magnitude of the magnetic field acts as a weight factor when averaging the current-helicity density h_c over a given active region. This may explain the different properties of h_c and α_f. Figure 6b shows the latitude dependence of the correlation of h_c and α_f upon averaging in latitude. The correlation decreases with increasing heliocentric distance; for example, the correlation is about 70% near the disk center and about 50% near latitude $\pm25°$. This difference can be ascribed to the influence of the effect of projection on estimations of the magnetic field, which is more important at higher latitudes and for larger inclinations of the field to the solar surface. There is also a slight difference between the two hemispheres.
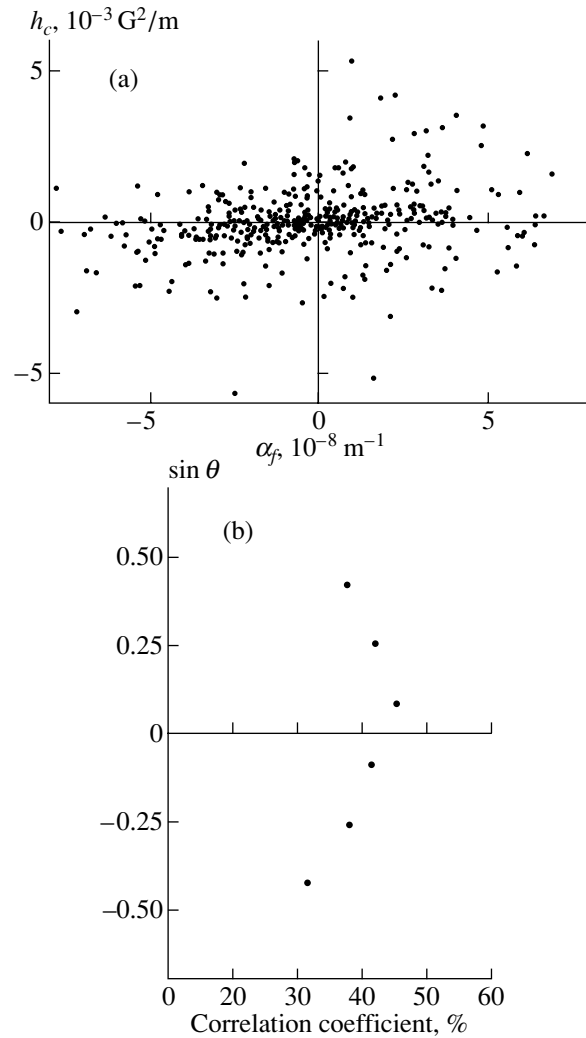
Fig. 6. (a) Relationship between the mean current-helicity parameters α_f and $\mathbf{B}_{\parallel} \cdot (\nabla \times \mathbf{B})_{\parallel}$ for 422 active regions. (b) Relationship between the correlation coefficient for h_c and α and the latitude after averaging over the sine of the latitude in steps of 0.05.

5. EVOLUTION OF THE MEAN HELICITY DENSITY

Figure 7a shows the time variations of h_c. The data show appreciable scatter in 1989−1993 and much lower values in 1994−1997. Accordingly, the solar activity was much higher in 1988−1993 and lower in 1994−1997. The relation between the mean current-helicity density and the number of sunspots was briefly analyzed in [4]. Comparing our Fig. 7a with Fig. 3 of [4], we find that the amplitude of $\mathbf{B}_{\parallel} \cdot (\nabla \times \mathbf{B})_{\parallel}$ changes with time. This implies that the current-helicity density of active regions depends on the phase of the solar magnetic cycle. This may be due to the fact that the magnetic-field strength varies with the solar cycle, with h_c somehow being proportional to the magnetic field.
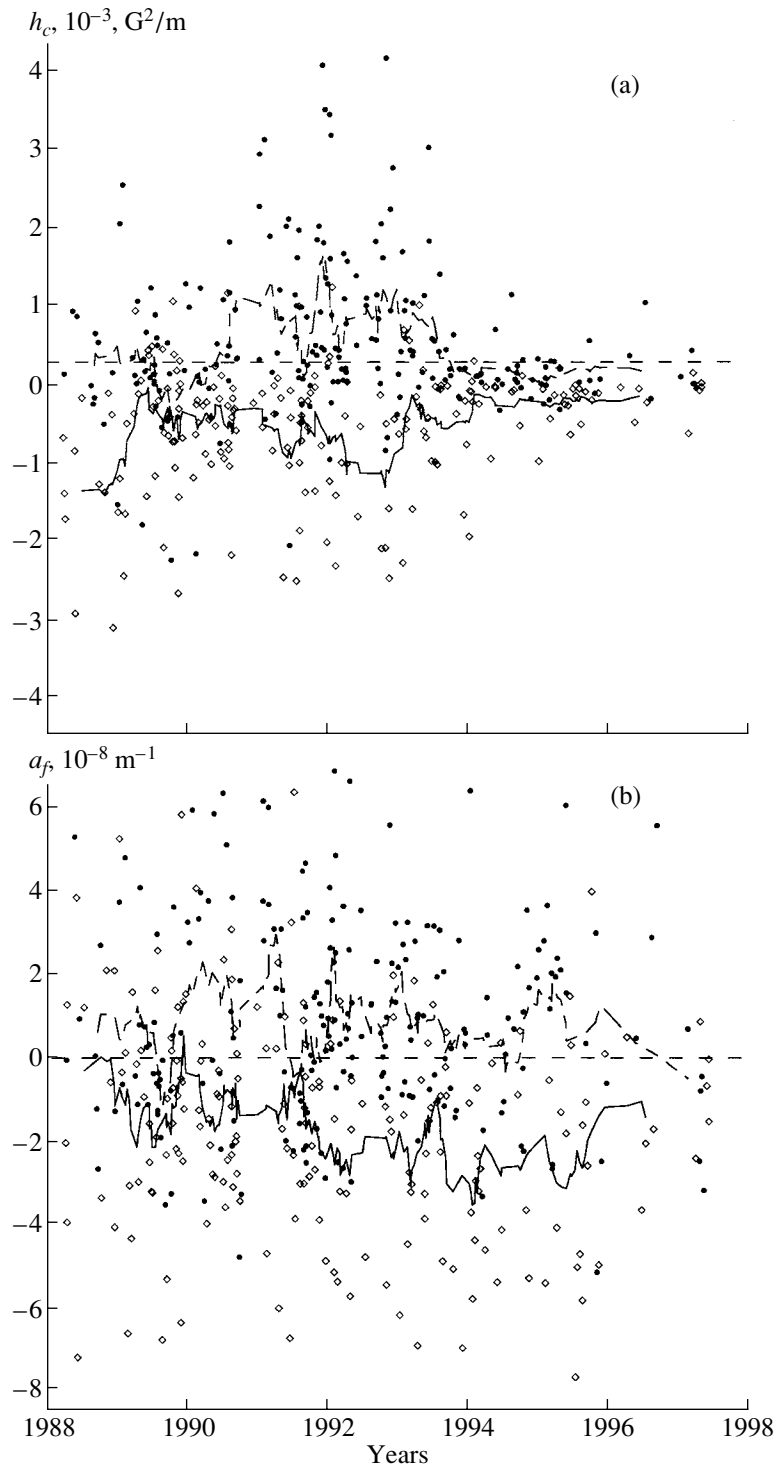
h_c, 10^{-3}, G^2/m

(a)

a_f, 10^{-8} m^{-1}

(b)

Years

Fig. 7. (a) Time evolution of $\mathbf{B}_\parallel \cdot (\bigtriangledown \times \mathbf{B})_\parallel$; the vertical axis is in 10^{-3} G^2/m. (b) Time evolution of α_f; the vertical axis is in 10^{-8} m^{-1}. The active regions in the northern and southern hemispheres are denoted by diamonds and filled circles, respectively. The solid line the 11-point moving average over the northern (southern) hemispheres.

Figure 7b shows the evolution of α_f during the same period. There is no significant difference between years of solar maximum and solar minimum. This implies that the mean twist density of active regions does not significantly depend on the solar activity. Moreover, the parameter α_f in active regions loses information about the magnetic-field strength. From a statistical point of view, it is difficult to find
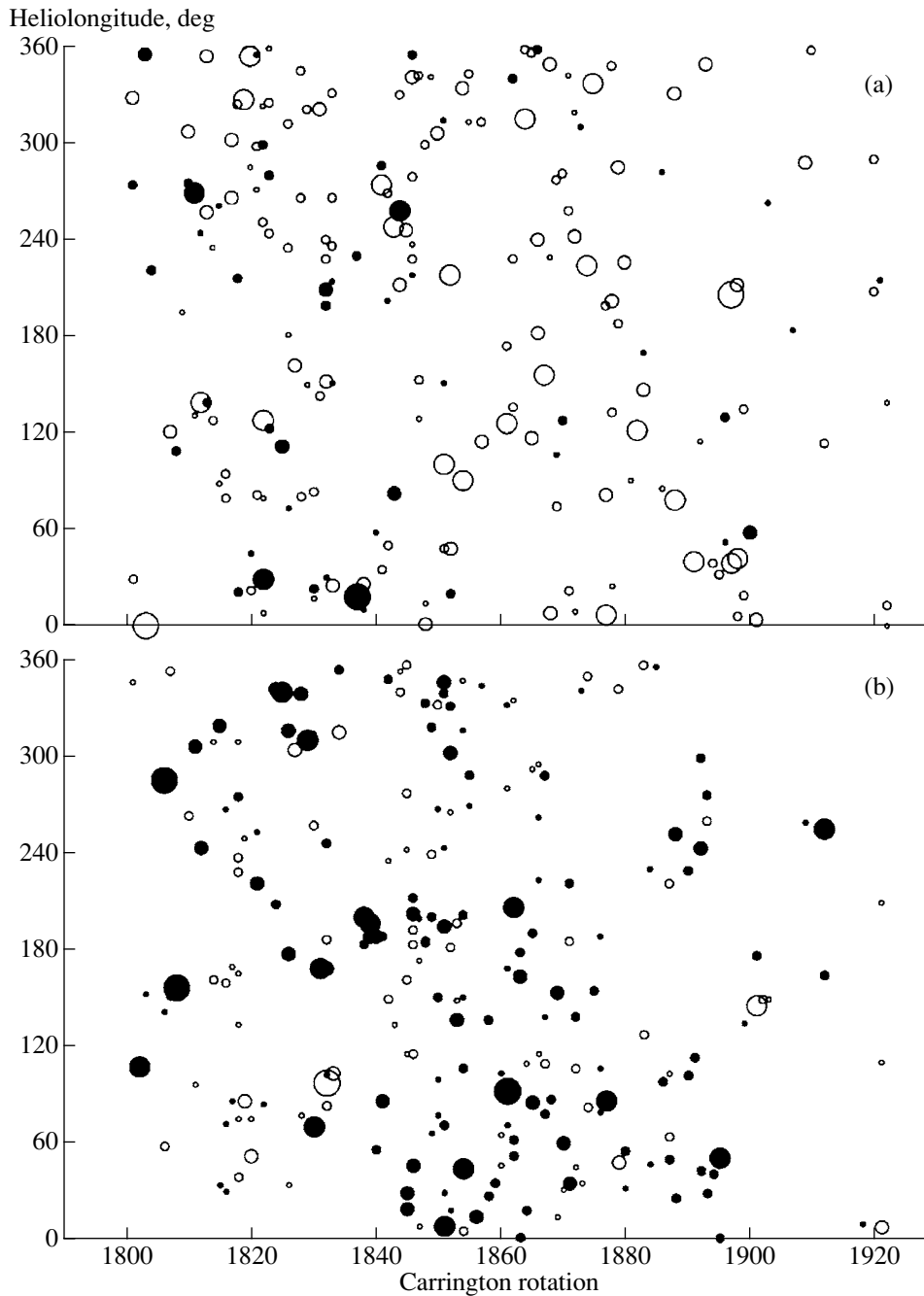
Fig. 8. Longitude distribution of α_f as a function of time (in terms of Carrington rotations) in the (a) northern and (b) southern hemispheres. The density is indicated by the sizes of the circles: $0, 1, 3, 5, 7\,(\times 10^{-8}\ \mathrm{m}^{-1})$. Black (white) circles denote positive (negative) sign values.

a clear dependence of the mean α_f on the phase of the solar cycle based on the studied sample of active regions.

6. LONGITUDE DISTRIBUTIONS OF α_f AND h_c

Figure 8 shows the longitudinal distribution of α_f as a function of time (measured in solar rotation periods) in both hemispheres. The regions where the sign of α_f does not follow the transequatorial rule are distributed quite uniformly in longitude. On the other hand, Zhang and Bao [7] found a tendency for active regions with opposite signs of h_c to cluster at certain longitudes. Note, however, that Canfield and Pevtsov [6] also analyzed the longitudinal distribution of α_f and found some tendency for active regions whose

helicity distribution did not follow the transequatorial rule to cluster at certain longitudes over many rotations.

7. DISCUSSION

Various properties of the twist of the photospheric magnetic field can be derived from magnetograms of active regions. The twist of the magnetic field is linked with the magnetic (current) helicity. Because the total helicity $\mathbf{B} \cdot (\bigtriangledown \times \mathbf{B})$ cannot be obtained using photospheric magnetographs, the study of $\mathbf{B}_{\parallel} \cdot (\bigtriangledown \times \mathbf{B})_{\parallel}$ and $\mathbf{B}_{\parallel} \cdot (\bigtriangledown \times \mathbf{B})_{\parallel}/B_{\parallel}^2$ (i.e., α_f) becomes important and necessary. By analyzing the helicity parameters in detail, we find that they not only obey the transequatorial rule [i.e., the mean current helicity and twist density of active regions usually have negative (positive) sign in the northern (southern) hemisphere] but also contain slightly different information on the twist properties of the magnetic field.

We see in (4) that α_f describes the degree of the twist of the magnetic field. It is normally believed that the twist of magnetic lines of force is due to the action of the Coriolis force, differential rotation, etc., as magnetic lines of force rise from the base of the convection zone and form active regions at the solar surface. If the magnetic field is generated by solar-dynamo action and the magnitude of the photospheric large-scale magnetic field depends on the phase of the solar activity cycle, the mean intensity of the electric current-helicity density should contain some information about both the twist and strength of the magnetic field. However, α_f is related to the twist of the magnetic field of active regions and does not depend on the intensity of the field, so the calculated value of α_f probably contains information primarily on the Coriolis force and differential rotation, which do not significantly change with the phase of the solar cycle.

On the other hand, in about 30% of the total number of active regions in each hemisphere, the sign of α_f is opposite to that of the majority of active regions in that hemisphere. In such active regions, the mean twist of the magnetic field differs from that determined by the Coriolis force. This probably reflects some statistical effects associated with the redistribution of solar magnetic fields, although this difference could also be partially due to the averaging procedure when twists of opposite sign for regions of weak field make a small contribution to the mean current-helicity density. Our results show that the two different helicity quantities α_f and h_c have different properties. The transequatorial rule is stronger for the h_c than for the α_f distribution.

The h_c distribution shows a clear dependence on the level of solar activity (phase of the solar cycle), while α_f does not. The active regions with reversed sign of h_c (disobeying the transequatorial rule) cluster at certain longitudes. We can clearly see indications of such reverse-sign longitudes for h_c, but not for α_f. One possibility is that α_f has lost information about the magnetic-field strength and contains mainly information on the magnetic shear near magnetic neutral lines, as discussed in [23, 7].

Although some properties of the helicity in solar active regions are discussed above, we should also point out that some differences between the distributions for α_f and h_c could be due to uncertainties in the observational data and reduction technique, as well as other factors, such as the effect of projecting the vector magnetic field onto the solar surface and errors in the measurements of the transverse magnetic field. However, it is hardly likely that such factors could cause about 40% of the active regions to have opposite signs for h_c and α_f (cf. Fig. 6a).

The basic agreement between the transverse magnetic fields determined from Huairou magnetograms and the fine structures in Hα and Hβ filtergrams has been confirmed by a number of studies [24, 25]. The influence of errors in the transverse field measurements on the difference in the current helicities calculated using the Huairou and Mees datasets was recently analyzed in [26]. It was found that this is probably not important for determining the signs of the current helicity in most active regions. However, it is not clear if such measurement errors contribute a systematic bias to the statistical properties of the current helicity of active regions. We also note that resolving the 180° ambiguity in the highly sheared transverse magnetic field in areas near magnetic neutral lines in active regions is associated with certain difficulties, which will be analyzed in forthcoming papers.

Thus, in this paper, we have studied the distributions of observational tracers of the α effect. Allowing for the qualifications about the applicability of the Keinings−Seehafer formula noted above, this is the first measurement of the α effect. Knowledge of the latitude and spatial distributions of the α effect is very important from the point of view of dynamo theory. If this theory is to explain Maunder butterfly diagrams, the dynamo waves [27] must propagate toward the equator at low latitudes. For this reason, the sign of the product of the radial gradient of the differential rotation and the α effect should be negative (positive) in the northern (southern) hemispheres. Earlier, insufficient knowledge of the value of the α effect led to uncertainty and created grounds for speculation about the direction of propagation of the dynamo wave.

Here, we suggest the following interpretation of the results of dynamo theory. The values of α_f and h_c are mainly negative (positive) in the northern (southern) hemispheres. These quantities are linked with the magnetic fields near the Solar surface. We expect these quantities to change sign deep in the solar convective zone (see, e.g., [28, 29]) so that they become positive (negative) in the northern (southern) hemispheres. Then, according to the Kainigs–Seehafer formula (2), the sign of the α effect near the convection-zone base is negative/positive in the northern/southern hemispheres. Taking into account the positive radial gradient of differential rotation (e.g., [30]) this leads to dynamo waves [27] propagating toward the equator, as required to explain Maunder butterfly diagrams.

We see that both h_c and α_f are equally important for identifying signatures of the solar α effect. We conclude that approaches based only on one of these tracers, such as α_f, even one having the same dimensions as the α effect, could have some shortcomings. Therefore, both of these tracers of the α effect should be taken into consideration in future studies. The parameter h_c is relevant for investigations of the sign of the α effect, while α_f is more suitable as an indicator of the magnitude of the α effect. Nevertheless, the use of data only for α_f [5] can reveal the main structure of the α effect in the solar convective zone.

8. CONCLUSION

Thus, the main results of the paper are the following.

(1) The average α_f and $h_c = \mathbf{B}_\parallel \cdot (\bigtriangledown \times \mathbf{B})_\parallel$ both provide information on the twist of magnetic-field lines. The difference is that α_f does not contain information on the magnetic-field strength, while h_c does.

(2) α_f and h_c show similar latitude and longitude distributions. However, the distribution of the mean current-helicity density h_c of active regions shows a stronger transequatorial regularity than does that of α_f. The distribution of active regions that do not follow the transequatorial rule for the sign of α_f is more uniform in longitude than the corresponding distribution for h_c and reveals no clustering at particular longitudes. This transequatorial sign rule for α_f and h_c corresponds to the general expectations of dynamo theory.

(3) About 40% of the active regions have α_f and h_c with opposite signs. This may be due to the fact that h_c depends on the magnetic-field strength as a weight factor.

REFERENCES

1. N. Seehafer, Sol. Phys. **125**, 219 (1990).
2. A. A. Pevtsov, R. C. Canfield, and T. R. Metchalf, Astrophys. J. Lett. **440**, L109 (1995).
3. V. I. Abramenko, T. J. Wang, and V. B. Yurchishin, Sol. Phys. **168**, 75 (1996).
4. S. D. Bao and H. Q. Zhang, Astrophys. J. **496**, L43 (1998).
5. K. M. Kuzanyan, H. Zhang, and S. Bao, Sol. Phys. **191**, 231 (2000).
6. R. C. Canfield and A. A. Pevtsov, in *Synoptic Solar Physics*, Ed. by K. S. Balasubramaniamn, J. W. Harvey, and D. M. Rabin, ASP Conf. Ser. **140**, 131 (1998).
7. H. Zhang and S. Bao, Astrophys. J. **519**, 876 (1999).
8. G. E. Hale, Nature **119**, 708 (1927).
9. R. S. Richardson, Astrophys. J. **93**, 24 (1941).
10. S. F. Martin, R. Bilimoria, and P. W. Tracada, in *Solar Surface Magnetism*, Eds. C. J. Rutten and C. J. Schrijver (Kluwer, Dordrecht, 1994), p. 303.
11. D. M. Rust and A. Kumar, Astrophys. J. Lett. **464**, L199 (1996).
12. F. Krause and K. H. Rädler, *Mean-Field Magnetohydrodynamics and Dynamo Theory* (Akademie-Verlag, Berlin, 1980).
13. F. Krause, Habilitationsschrift (Univ. Jena, 1967); *The Turbulent Dynamo,* NCAR Technical Note TN/IA-60 (1971).
14. A. Brandenburg and K. J. Donner, Mon. Not. R. Astron. Soc. **288**, L29 (1997).
15. A. Brandenburg, S. H. Saar, and C. R. Turpin, Astrophys. J. Lett. **498**, L51 (1998).
16. R. K. Keinigs, Phys. Fluids **26**, 2558 (1983).
17. N. Seehafer, Europhys. Lett. **27**, 353 (1994).
18. N. Seehafer, in *New Perspectives on Solar Prominences (IAU Coll. 167)*, Eds. D. Webb, D. Rust, and B. Schmieder, ASP Conf. Ser. **150**, 407 (1998).
19. D. W. Longcope, G. H. Fisher, and A. A. Pevtsov, Astrophys. J. **507**, 417 (1998).

20. L. Woltjer, Proc. Nat. Acad. Sci. **44**, 489 (1958).
21. T. J. Wang, A. A. Xu, and H. Q. Zhang, Sol. Phys. **155**, 99 (1994).
22. J. B. Zirker, S. F. Martin, K. Harvey, and V. Gaizauskas, Sol. Phys. **175**, 27 (1997).
23. H. Zhang and S. Bao, Astron. Astrophys. **339**, 880 (1998).
24. H. Q. Zhang, G. Ai, T. Sakurai, and H. Kurokawa, Sol. Phys. **136**, 269 (1991).
25. H. Q. Zhang, Sol. Phys. **154**, 207 (1994).
26. S. D. Bao, A. A. Pevtsov, T. J. Wang, and H. Q. Zhang, Sol. Phys. **195**, 75 (2000).
27. E. N. Parker, Astrophys. J. **122**, 293 (1955).
28. H. Yoshimura, Astrophys. J. **247**, 1102 (1981).
29. N. H. Brummell, N. E. Hurlburt, and J. Toomre, Astrophys. J. **493**, 955 (1998).
30. J. Schou, H. M. Antia, S. Basu, *et al.*, Astrophys. J. **505**, 390 (1998).

Translated by H. Zhang